2017

A Study On The Plasticity And Fracture Behaviors Of Inconel 718 Under Multiaxial Stress And Extremely Low Cycle Fatigue Loadings

Mohammed Algarni
University of Central Florida

A STUDY ON THE PLASTICITY AND FRACTURE BEHAVIORS OF INCONEL 718 UNDER MULTIAXIAL STRESS AND EXTREMELY LOW CYCLE FATIGUE LOADINGS

by

MOHAMMED SALEH ALGARNI

B.S. King Fahd University of Petroleum and Minerals, 2006
M.S. University of Central Florida, 2013

A dissertation submitted in partial fulfillment of the requirements
for the degree of Doctor of Philosophy
in the Department of Mechanical and Aerospace Engineering
in the College of Engineering and Computer Science
at the University of Central Florida
Orlando, Florida

Spring Term
2017

Major Professor: Yuanli Bai

ABSTRACT

Engineering materials and structures are usually subjected to multiaxial stress states loading due to geometrical effects, residual stresses, or multi-directional loading. Ductile fracture and Extremely Low Cycle Fatigue (ELCF), less than 100 cycles to fail, are two common and co-exist failure modes in many engineering structures. However, the linkage between these two failure modes under multi-axial loading conditions has never been systematically studied. This research summarizes an extensive work of experimental and numerical studies of ductile fracture and ELCF under different stress states for nickel-base superalloy material "IN718" under room temperature. Specially designed specimens and tests were used to achieve desired multi-axial loading conditions. Four types of specimens with four different shapes, total of 16 specimens, were tested until complete fracture. Two groups of tests were conducted: (a) round bar specimens with different notches; (b) plane strain specimens. Experimental data of force-displacement curves and strain-life graph were plotted for analysis.

The first part of this research focuses on a numerical study of monotonic tensile loading with different stress states. This part of the investigation deeply studies the dependency of the hydrostatic stress (related to stress triaxiality) and the normalized third invariant of the deviatoric stress (related to Lode angle parameter) in plastic behavior and ductile fracture. Constitutive plasticity model proposed by Bai & Wierzbicki and the modified Mohr-Coulomb (MMC) ductile fracture model were adapted with several extensions. The plasticity model and ductile fracture criterion were implemented into ABAQUS through a user-defined material subroutine (VUMAT). Extensive experimental

results are used to calibrate the models. After setting up the parameter optimization during model calibration, the experimental results and numerical simulations were well correlated in both plasticity deformation and fracture initiation. A 3D fracture locus of Inconel 718 was constructed by knowing the strain at fracture, stress triaxiality, and normalized Lode angle of the tested samples. By introducing a suitable element post-failure behavior, not only the fracture initiation but also the fracture propagation modes are successfully predicted in finite element simulations for monotonic loading.

The second part extensively investigates ELCF on IN718. The IN718 cyclic plasticity behavior and the Bauschinger effect are studied and simulated using the well-known nonlinear kinematic hardening law by J. L. Chaboche and his co-workers under different strain amplitudes and different stress states. Moreover, the Vocé isotropic hardening law was applied in combination with the Bai-Wierzbicki plasticity model. The Bai-Wierzbicki plasticity model was used to capture the effect of different stress states on ELCF based on the stress triaxiality and Lode angle parameters. On the other hand, the modified Mohr–Coulomb (MMC) ductile fracture model for monotonic loading was extended by a new damage evolution rule to cover the ELCF regime. A new parameter was introduced to represent the effect of the cyclic loading at ELCF. The new parameter is responsible for capturing the change of non-proportional loading direction between the current stress and the backstress tensors. The model explores the underlying damage and fracture mechanisms through the equivalent plastic strain evolution under cycling loading.

Finally, the mechanism linkage between these two failure modes was studied. A comparison between the experimental data and the finite element simulation results (by Abaqus/Explicit) shows very good correlations. In addition, fractographic examinations, analysis, and finite element simulations are presented.

ACKNOWLEDGMENTS

First and foremost, I would like to express my sincere gratitude to my academic advisor, Professor **Yuanli Bai**, for his guidance, encouragement, and patience rendered throughout my years of study at University of Central Florida (UCF). I'm extremely indebted for his suggestions and daily discussions throughout my doctoral research. This dissertation would not have been possible without his persistent help. He has inspired me to become an independent researcher. Also, I want to thank my committee members, Professor **Alain Kassab**, Professor **Quanfang Chen**, Professor **Hansen Mansy**, and Professor **BooHyun Nam** for their continuous instruction. Furthermore, I want to thank my friends in the Lab of Solid and Structure Mechanics (LSSM) for their limitless help and support and in particular my very close friend Professor **Yueqian Jia** for all the daily consultations and all his never-ending generous advice. Also, I want to thank **Timothy Lindner,** machine laboratory manager, for his thoughtful advices and sharing experience.

Also, I would like to extend my deepest thanks and sincere appreciation to my **mother** and **father** for not only giving me the inspiration and the motivation to complete my studies, but also for their prayers and faith in me. My appreciation extends to my dear sisters and brothers for all their supportive conversations.

I gratefully acknowledge the financial support from the Ministry of Education in Kingdom of Saudi Arabia and from Royal Embassy of Saudi Arabia Cultural Bureau in Washington, D.C. Also, many thanks to my friends and colleagues at King AbdulAziz University (KAU) and the faculty of the Mechanical Engineering department in Rabigh for their kind support and assistance throughout my graduate studies years.

Finally, and most importantly, I would like to thank my beloved wife **May**. Her unwavering love, enormous patience and encouragement were undeniably the bedrock upon which completion of my studies has been achieved. Her tolerance of my many hours researching in the lab is proof in itself of her unyielding devotion and love. Without her behind me, I doubt that I would be in this place today. To my two little adorable princesses, **Mariya** and **Hanan**, thank you for all the fun time you shared with me.

I am dedicating this research to our great leader **King Abdullah bin AbdualAziz** may his sole rest in peace. During his 10 years of ruling the kingdom, our country witnessed many developmental achievements across the country. Specifically, the education process witnessed huge improvements; a great amount of the Kingdom's revenues was directed to the improvement and development of education and many overseas scholarships were granted to the people.

TABLE OF CONTENTS

LIST OF FIGURES

LIST OF TABLES

LIST OF NOMENCLATURE

a_o, a	initial and final necking radius
A, σ_y, K	material coefficients in power strain hardening law
$B_1, B_2, B_3, \ and \ B_4$	material parameters in the extended plasticity model
c_η	coefficient of stress triaxiality dependency on plasticity
c_θ^s, c_θ^t, c_θ^c, c_θ^{AX} and m	material parameters in plasticity model by Bai and Wierzbicki
$\tilde{c}_\theta^s$, $\tilde{c}_\theta^c$, c_1, and c_2	material parameters in the MMC fracture criterion
D	damage indicator
D_c	critical damage indicator for element deletion
I	identity tensor
J_2	the second stress invariant
L_o	reference gauge length
n, N	material power strain hardening exponent
p, q, r	three stress invariants
r	radial coordinate from the center of specimen notch
R	notch radius
S	deviatoric stress tensor
S_1, S_2, S_3	three principal stresses of deviatoric stress tensor
w	material post-failure softening power coefficient
β	material post-failure softening factor
γ	Lode parameter

$\varepsilon_t, \varepsilon_E$	true strain and engineering strain
$\bar{\varepsilon}_{\mathrm{pl}}$	equivalent plastic strain
$\bar{\varepsilon}_{\mathrm{f}}$	equivalent plastic strain to fracture
η	stress triaxiality
η_{o}	reference value of stress triaxiality from a reference test
η_{avg}	average stress triaxiality
θ	Lode angle
$\bar{\theta}$	Lode angle parameter or normalized Lode angle
$\bar{\theta}_{\mathrm{avg}}$	average Lode angle parameter
ξ	normalized third deviatoric stress invariant
$\bar{\sigma}$	equivalent stress
$\sigma_1, \sigma_2, \sigma_3$	three principal stresses
σ_m	mean stress
σ_t, σ_E	true stress and engineering stress
$\sigma_{xx}, \sigma_{yy}, \sigma_{zz}$	axial, radial, and hoop stresses
$\bar{\sigma}_{yield}$	equivalent stress to yield in Ludwik's model
$\tilde{\sigma}_{yield}$	softened flow stress

CHAPTER ONE:
INTRODUCTION

Mechanical failure can cause fatal incidents or major injuries along with huge monetary loss. An example of a tragic major incident pertaining to a mechanical fracture and fatigue failure happened in 1968 for the famous RMS “Queen Elizabeth 2” liner. The failure occurred during the ship’s maidan voyage from Tail O’ the bank, resulting in a severe damage to the 9^{th} stage starboard High Pressure (HP) and the 9^{th} stage port HP turbine rotor. The investigation concluded that the failure occurred due to the resonances of the blade packet.

Another major incident occurred in 1983 when a 600 MW turbo-set was restarted after a periodic inspection. An explosion happened during the testing stage prior to processing the machine to the live service. The blast investigation shows two complete ruptures on the exciter end of the generator shaft in the high-pressure section. It also shows beach marks on a broken blade surface in the low-pressure stage. The damage cost was estimated to be more than $40 million. These major incidents were attributed to fracture in the high-pressure stages and to fatigue in the low-pressure stages [1-3].

Nevertheless, the number of mechanical failures significantly decreased in the past years due to the enormous amount of research in different failure modes and the well-designed components and structures. Many factors can be involved in mechanical failures such as time, temperature, corrosion, erosion, impact, and other load types. Each factor can be solely a cause of a mechanical failure, or it can be a complex interaction of two or more factors. The time factor can be years (i.e. steel bridges) or milliseconds (i.e.

fire gun cartage malfunctions). The temperature factor may range from cryogenic in spaceships to high temperature (over 1000^{o}C) in gas turbine engines. Temperature may also vary or remain steady. Corrosion factor may be severe such as exposing a structure to a salt water environment or may have negligible effects like in a vacuum. The load factor itself can be separated into many conditions such as static, quasi-static, monotonic, cyclic, uniaxial, multiaxial, etc.

In summary, mechanical failure modes of metals occur in many possible scenarios. However, a large number of studies proposed many plasticity models for monotonic and cyclic loading, independently, to understand the material's behavior under different loading conditions [4-22]. In addition, many ductile fracture criteria were also developed for both monotonic and cyclic loading [23-30]. Mechanical engineering designers often use these models independently to study the metal structure behavior and life prediction for each failure scenario separately. Thus, it is more efficient to generate a procedural approach with a minimum amount of material parameters to study both mechanical failures (fracture and fatigue) which can be carried out by finite element analysis packages. For designers, this will save them an enormous amount of money and time. Also, more parametric studies will probably lead to improve components or structures design.

1.1 Quasi-Static and Cyclic Loading

Mechanical failure modes of metals occur in many possible scenarios. However, the current dissertation will solely focus the investigation on two types of mechanical

failures. The two types of mechanical failures are ductile fracture and metal fatigue. The ductile fracture is caused by quasi-static loading. Quasi-static loading is considerably slow such that the inertial effects are neglected. A thorough evaluation of Inconel 718 plastic flow behavior under quasi-static and cyclic loading with ductile fracture modeling under different loading conditions is studied.

The other type of the mechanical failures is fatigue under cyclic loading conditions. Fatigue is *the process of progressive localized permanent structural change occurring in a material subjected to conditions that produce fluctuating stresses and strains at some point or points, and that may culminate in cracks or complete fracture after a sufficient number of fluctuations* [31]. Based on the number of loading cycles to failure, fatigue can be divided into three major types: High Cycle Fatigue (HCF), Low Cycle Fatigue (LCF), and Extremely Low Cycle Fatigue (ELCF). The definition of the transition cycle from one fatigue regime to another is generally vague and varies by the material in different sources. For Inconel 718 behavior, many sources consensus the transient number of cycles are as in Figure 1 [32-39]. Apparently, the ELCF regime starts at 1 cycle to 10^2 cycles. The HCF regime starts just above 10^4 cycles whereas LCF regime falls in between. The ELCF and LCF regimes are usually characterized by strain-controlled testing. The stresses in these two regimes are between the yielding stress and the ultimate tensile strength. On the other hand, HCF is characterized by stress-controlled testing and the loading amplitudes are below the yield stress limit [40]. Studies on cyclic loading in this dissertation will only focus on the Extreme Low Cycle Fatigue pertaining to high strain amplitudes.

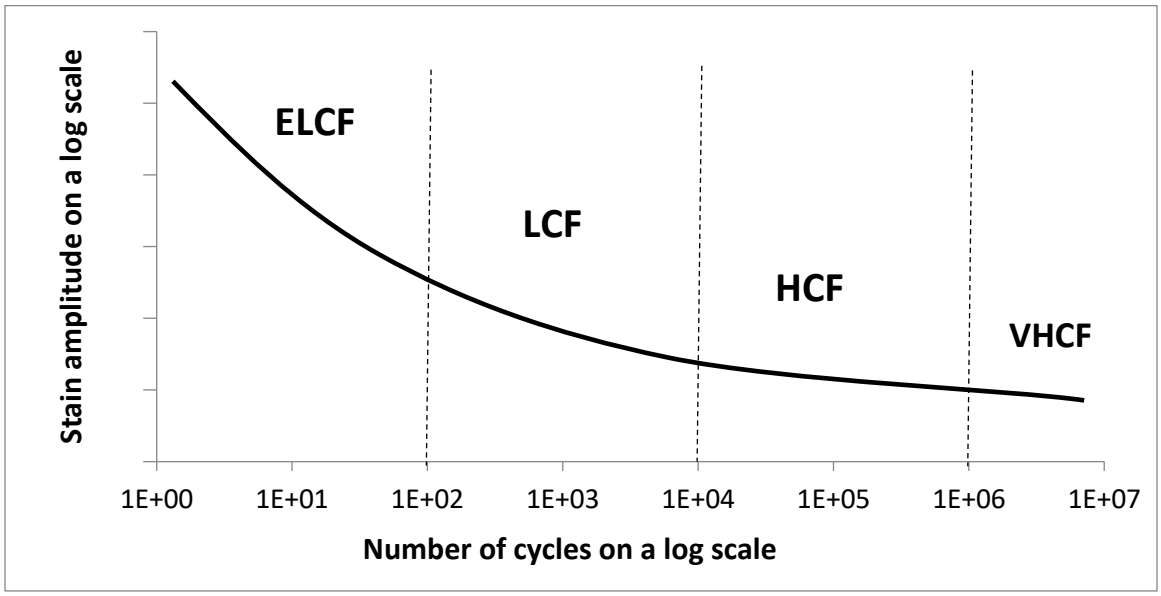

Figure 1: A log scale plot illustrating the number of cycles for the fatigue regimes.

In history, the study of ductile fracture and fatigue were independently studied. The need for combining both failure modes arises in the process of designing a structure to withstand high stresses or large deformations. One example of this is the seismic loading. In a seismic event, metal structures are assumed to undergo a large plastic deformation due to the earthquake's extreme forces without a significant loss of strength. Another example that can combine both scenarios of mechanical failures is blade-out failure in a jet engine. Due to the high pressure in a jet engine and the massive centrifugal forces, blades are more apt to failures pertaining to abrupt ductile fracture or ELCF failures.

1.2 Motivations and Objectives

In real applications, most components and structures are subjected to multiaxial loading. These loads may vary in amplitudes and applied under different loading conditions. Therefore, in the aircraft-engine design standard, all manufacturers are subjected to run severe tests on their engines to examine its integrity. Monotonic and cyclic loading tests on the rotor blades are part of these severe tests. The statistics show that more than 90% of all mechanical failures are caused by metal fatigue [41]. Therefore, more research in studying these two types of mechanical failures is increasingly progressing.

The objective of this research is to build a framework for a metal's plasticity model that can describe the materials' behavior under multiaxial stresses. Also, predicting the materials' life by using a damage-based model is another part of the thesis objective. The established study will help designers to improve and understand the life performance of a simple metal component to complicated metal structure systems.

1.3 Structure of the Thesis

The thesis will consists of seven chapters. Chapter 1 expresses the introduction, motivations, and objectives of the research. Chapter 2 involves a literature review of the metal plasticity material models and fundamentals for both monotonic and cyclic loadings. Four research papers were published in accordance with this research. These papers will be included in chapters 3 to 6. Each chapter will present a single research

paper. Finally, chapter 7 shows the comprehensive Ph.D. research conclusion and the suggested future work. The contents of each chapter are summarized as follows.

CHAPTER 1: A brief introduction about quasi-static and reversal loading followed by the motivation and objectives.

CHAPTER 2: An extended literature review of the theory of metal plasticity and a thorough overview of the phenomenological and current metal plasticity models. In the end, two summary tables of the metal plasticity models and ductile fracture models assist in a fast tracking.

CHAPTER 3: Paper I: **M. Algarni**, Y. Jia, J. Karl, A. P. Gordon, Y. Bai, M. The Minerals*, et al.*, "Linkage between Ductile Fracture and Extremely Low Cycle Fatigue of Inconel 718 Under Multiaxial Loading Conditions," in *TMS2015 Supplemental Proceedings*, ed: John Wiley & Sons, Inc., 2015, pp. 1023-1030.

CHAPTER 4: Paper II: **Algarni, Mohammed**, Yuanli Bai, and Youngsik Choi. "A study of Inconel 718 dependency on stress triaxiality and Lode angle in plastic deformation and ductile fracture." Engineering Fracture Mechanics 147 (2015): 140-157.

CHAPTER 5: Paper III: **Algarni, M.**, and Yuanli Bai. "A unified material model for multiaxial ductile fracture and extremely low cycle fatigue of Inconel", *ready to be submitted to IJ Fatigue in fall 2016*.

CHAPTER 6: Paper IV: **M. Algarni**, Y. Bai., “Extremely Low Cycle Fatigue Damage Mechanism, Fractographic Examination, And Life Prediction," in

Materials Science & Technology Conference and Exhibition 2016; Supplemental Proceedings, Salt Lake City, Utah, USA, *publication due in October 2016.*

CHAPTER 7: Conclusion and future work.

CHAPTER TWO:
LITERATURE REVIEW

This chapter will cover a brief overview of the early and current ongoing research related to fracture and ELCF. It will then address the most phenomenological metal plasticity and ductile failure models. Accordingly, a list of coupled and non-coupled plasticity models and ductile failure criteria will be thoroughly explained to set a strong background to help understand the succeeding chapters. The first section (2.1) covers a comprehensive literature review to show the current state of the art of fracture and ELCF. The second section (2.1) starts with an explanation of the principle stresses to show how they represent a yield surface. Since most yield functions are functions of the stress invariant, an extended explanation of stress invariants space is described. After that, the most phenomenal plasticity and fracture models for continuum mechanics are listed. All these models assume the material isotropy, homogeneous and behave in an elastic-plastic behavior. A list of isotropic hardening and kinematic hardening models for reversal loading are described in section (2.2.5.3). Isotropic hardening controls the yield surface expansion or shrinkage whereas the kinematic hardening only translates the yield surface in the stress space. Section (2.4) shows the fundamentals of fatigue strain-life and the underlying models used.

2.1 Ductile Fracture and Extremely Low Cycle Fatigue

Ductility is defined as the ability of a material to accept large amounts of plastic deformation without crack [42]. Bai and Wierzbicki [4] have proposed a new model for

metal plasticity and ductile fracture that includes the effect of the hydrostatic pressure (related to the stress triaxiality) and the effect of the third invariant of the deviatoric stress tensor. The effect of the hydrostatic pressure is responsible for controlling the size of the yield surface whereas the effect of the third invariant of the stress deviator is responsible for the shape of the yield surface [43]. An efficient numerical integration algorithm for this model was presented in Ref. [44], where the simulation results in finite element (FE) analysis are satisfactory.

Decades ago, McClintock [45], Rice and Tracey [46], Hancock and Mackenzie [47], Hancock and Brown [48] have showed that ductile fracture is a function of the hydrostatic pressure (stress triaxiality). As a result, the Johnson-Cook ductile fracture model [26] was provided and widely used. On the other hand, many ongoing numerical and experimental studies on ductile materials have verified that a new parameter (along with the stress triaxiality) needs to be considered in predicting the ductile fracture. This parameter is the third invariant of deviatoric stress tensor (which is related to the Lode angle). It plays a crucial role in providing a better fracture prediction along with the stress triaxiality [4, 5, 7, 8, 25, 49-55]. These intense research works showed a decisive relation of the Lode angle to predict correctly ductile material failure. An extension of the classical Mohr-Coulomb fracture criterion was postulated in Ref. [25] under assumption of proportional loading and asymmetric metal plasticity (considering both the pressure sensitivity and the Lode angle dependence). This model predicts shear fractures as well as tensile cracks under multiaxial loading conditions. Over the past few years, this model

has been successfully applied to various applications, especially the metal sheet ductile fracture [6, 38, 56-60].

Inconel 718 was tested to calibrate a multiaxial constitutive model that accounts for the strength-differential [61]. The term "strength-differential" means different plastic flow behavior under uniaxial tension and uniaxial compression. This multiaxial constitutive model differs from the classical metal plasticity by adding all three stress-invariants in its yield function. This promising model is a general form of Durcker [62] and Drucker-Prager [63] models. The plastic deformation behavior of Inconel 718 at different strain rates was studied in Refs. [64, 65] and [66] using the Johnson-Cook (J-C) constitutive relation [10]. Nevertheless, the J-C plasticity model does not take the stress triaxiality ratio nor the Lode angle into account. A study was reported in Ref. [67] to investigate the effect of superimposed hydrostatic pressure using a pressure vessel. The pressure used ranges from 210 to 630 MPa using Ar gas. It was concluded that the plasticity of Inconel 718 is independent of superimposed ambient hydrostatic pressure.

Recently, Inconel 718 is tested to validate a coupled elastoplastic-damage constitutive model with Lode angle dependent failure criterion by Eric and Galvez [9]. This model introduced a new factor, called the weakening function, to the classical Johnson-Cook relationship [10]. It was shown that the combination of a Lode angle dependent failure criterion with weakened constitutive equations is necessary to predict fracture patterns of the mechanical tests performed and provided reliable results. The same research group [68] investigated the ductile failure of Inconel 718 superalloy under

quasi-static and impact loading using the proposed hardening model and the coupled elastoplastic-damage constitutive model with failure criterion [9].

In comparison, this dissertation will study the plasticity and ductile fracture of Inconel 718 using the recent uncoupled continuum plasticity model proposed by Bai and Wierzbicki [4] and the modified Mohr-Coulomb (MMC) ductile fracture criterion [25]. Mechanical tests under different stress states are designed and conducted. Numerical simulations are set up using ABAQUS/explicit to provide information when direct measures are not possible.

2.2 Metal Plasticity and Ductile Fracture

A comprehensive explanation of some phenomenological and current metal plasticity and ductile fracture models is explained here. Fundamental concepts of solid mechanics (i.e. deviatoric stresses and stress invariants), yielding criteria, and uncoupled and coupled damage-plasticity models are described in the coming sections to establish a solid ground that will assist in comprehending the methodology and terminologies in this dissertation.

2.2.1 Principal Stress Space

Any state of stress $[\sigma_{ij}]$ can be described in terms of three principal stresses denoted by $\sigma_1, \sigma_2, and\ \sigma_3$. These principal stresses form the cartesian coordinate system in a principal stress space where $\sigma_1 \geq \sigma_2 \geq \sigma_3$. The equation of the π-plane in the principal stress state is $\sigma_1 + \sigma_2 + \sigma_3 = 0$ (see Figure 2). Accordingly, a stress tensor

σ_{ij} can be represented in a vector $\left|\overrightarrow{OP}\right|$ in the principal stress space that starts from the origin O $(0, 0, 0)$ and ends at an arbitrary point P ($\sigma_1, \sigma_2, \sigma_3$). The image of the vector $\left|\overrightarrow{OP}\right|$ on the π-plane is called $\left|\overrightarrow{OM}\right|$ and represent the deviatoric stress of the stress tensor by the definition $[S_{ij}] = [\sigma_{ij}] + \sigma_m[I]$ where S_{ij}, σ_m , and I are the deviatoric stress tensor, mean stress and the identity tensor, respectively. In addition, the image of the stress tensor $\left|\overrightarrow{OP}\right|$ on the cylindrical shape is $\left|\overrightarrow{OO'}\right|$ and lies on a hydrostatic axis that has a direction of $\left(\frac{1}{\sqrt{3}}, \frac{1}{\sqrt{3}}, \frac{1}{\sqrt{3}}\right)$, where all $\sigma_1, \sigma_2, \sigma_3$ are equal. The π-plane of an isotropic material represents its yield surface and its failure criterion shape is written as $f(\sigma_1, \sigma_2, \sigma_3) = 0$. Thus, when yielding happens at any stress state $\{\sigma_1, \sigma_2, \sigma_3\}$, it must also yield for $\{\sigma_2, \sigma_1, \sigma_3\}$ or $\{\sigma_3, \sigma_2, \sigma_1\}$ as in Figure 3. Hence, the yield surface should be symmetric about σ_1 axis. By applying the same logic, the yield surface (π-plane) must be symmetric about σ_2 and σ_3 axes. This leads us to image a yield surface of six-fold symmetric segments of 60^o which represents the six possible ordering of the principal stresses state. In view of that, any point (or stress state) on the yield surface has six symmetry points on each segment. The yielding of any isotropic material occurs once the stress tensor lies on the yield surface. [69]

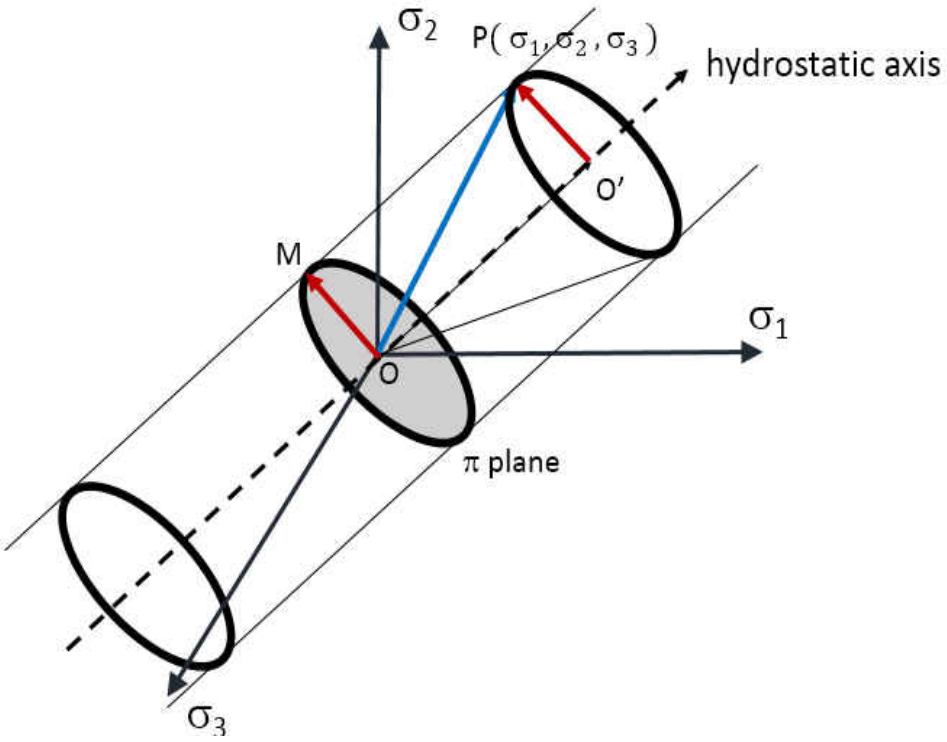

Figure 2: Imaginary yield surface in the space of principal stresses.

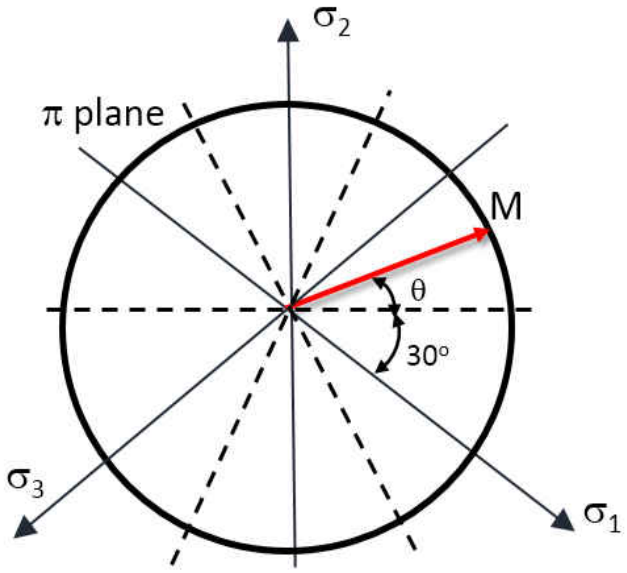

Figure 3: Arbitrary π plane of an isotropic material symmetry yield surface

2.2.2 Stress Invariant Representation

The three stress invariants (I_1, I_2, I_3) can also represent a yield function $f(I_1, I_2, I_3) = 0$ based on the principal stresses. As mentioned before, the most common yield criteria are functions of the stress invariants. Nonetheless, a relative recent combination of invariants are extensively used in yield functions in recent ongoing researches. The combinations of invariants are $f(\sigma_H, \bar{\sigma}, \theta) = 0$ where σ_H is the hydrostatic stress, $\bar{\sigma}$ is the von-Mises equivalent stress, and θ is the Lode angle. The hydrostatic stress σ_H is based on the stress tensor whereas $\bar{\sigma}$ and θ are based on the deviatoric stress tensor. These combinations of invariants can be expressed by the following equations:

$$\sigma_H = \frac{1}{3} I_1 = \frac{1}{3} tr([\sigma]) = \frac{1}{3} (\sigma_1 + \sigma_2 + \sigma_3) \quad (1)$$

$$\bar{\sigma} = \sqrt{3J_2} = \sqrt{\frac{3}{2} [S] : [S]} = \sqrt{\frac{1}{2}[(\sigma_1 - \sigma_2)^2 + (\sigma_2 - \sigma_3)^2 + (\sigma_3 - \sigma_1)^2]} \quad (2)$$

$$cos(3\theta) = \left(\frac{3\sqrt{3} J_3}{2 {J_2}^{3/2}}\right) = \left(\frac{27 J_3}{2\bar{\sigma}^3}\right) \quad (3)$$

$$J_2 = \frac{1}{2} [S] : [S] = \frac{1}{2}({S_1}^2 + {S_2}^2 + {S_3}^2) \quad (4)$$

$$J_3 = \frac{1}{3} \mathrm{tr}([S])^3 = S_1 S_2 S_3 \quad (5)$$

The hydrostatic stress controls the elevation of the π-plane along the hydrostatic axis. Since J_2 and J_3 cannot be easily interpreted on the π-plane, we use the Lode angle θ parameter instead to describe the stress state. The Lode angle θ is a function of J_2 and J_3. The Lode angle is the angle between $\left|\overrightarrow{OM}\right|$ and the closest principal axis. Therefore, the range of the Lode angle is $-\pi/6 \leq \theta \leq \pi/6$. The Lode angle can be normalized and

known as the normalized Lode angle ($\overline{\theta}$) that range from -1 ≤ $\overline{\theta}$ ≤ 1. Finally, Stress triaxiality (η) is a dimensionless hydrostatic pressure used to relate the elevation angle of $\left|\overrightarrow{OP}\right|$ to the π-plane [43, 70]. Stress triaxiality is defined by

$$\eta = \frac{\sigma_m}{\bar{\sigma}} = \frac{\sqrt{2}}{3}\frac{\left|\overrightarrow{OO'}\right|}{\left|\overrightarrow{O'P}\right|} \quad (6)$$

$$\overline{\theta} = 1 - \frac{6\theta}{\pi} \quad (7)$$

By using these parameters ($\eta, \overline{\theta}$), one can uniquely characterize several stress state specimens that are used for plasticity and fracture tests. The characterization using analytical values are shown in Table 1 and represented on η and $\overline{\theta}$ map in Figure 4.

Table 1: The characterization of classical specimens for plasticity and fracture tests [4].

No.	Specimen Type	η	$\overline{\theta}$
1.	Smooth round bars, tension	$1/3$	1
2.	Plastic plane strain, tension	$\sqrt{3}/3$	0
3.	Torsion or shear	0	0
4.	Cylinders, compression	$-1/3$	-1
5.	Equi-biaxial plane stress tension	$2/3$	-1
6.	Equi-biaxial plane stress compression	$-2/3$	1
7.	Plastic plane strain, compression	$-\sqrt{3}/3$	0

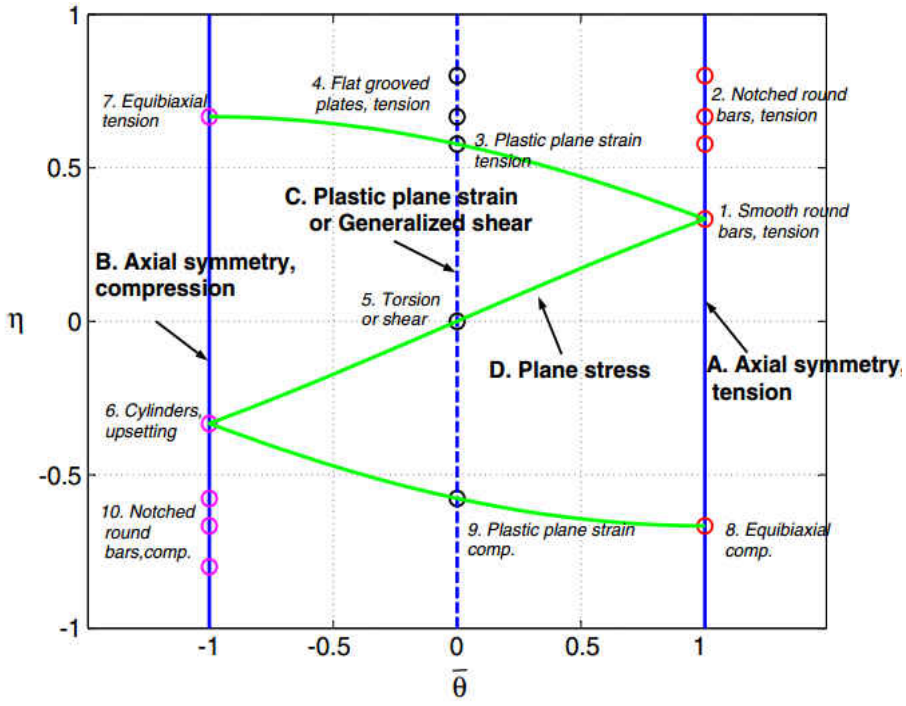

Figure 4. Different stress states on η and $\overline{\theta}$ map [4].

2.2.3 Isotropic Yield & Damage Criteria

Most metals are significantly homogenous in properties due to it polycrystalline microstructure. This makes most metals classified as isotropic. The most common yielding criteria applied to metals are independent of the hydrostatic stress/pressure ($\sigma_H = -p = \frac{1}{3} I_1$) [71, 72]. The hydrostatic stress becomes necessary when yielding criteria is applied to rocks, soils, and concrete [73]. For the sake of simplicity, yielding criteria based on the hydrostatic stress (i.e. Drucker-Prager criterion [74]) will not be considered here in the literature review chapter nor in this dissertation.

2.2.3.1 Tresca Yield Criteria

The Tresca yield criteria is historically the oldest. It was found in 1864 and it embrace the assumption that material yield onset when the maximum shear stress attains a particular value of $K(\gamma)$ where $K(\gamma)$ is the shear yield stress function of an internal variable [75].

$$\tau_{max} = \frac{1}{2}(\sigma_1 - \sigma_3) \quad (8)$$

$$\frac{1}{2}(\sigma_1 - \sigma_3) = K(\gamma) \quad (9)$$

where σ_1 and σ_3 are the maximum and minimum principal stress, respectively. Since the uniaxial yield stress $Y(\gamma)$ is equal to $2K(\gamma)$, the Tresca yield criterion can be described as:

$$f(\sigma,\gamma) = (\sigma_1 - \sigma_3) - K(\gamma) \quad (10)$$

and may also be described in terms of J_2 and Lode angle (θ) as follows:

$$f(J_2,\theta) = 2\sqrt{J_2}\cos\theta - K(\gamma) \quad (11)$$

The projection of the Tresca yield surface in the π-plane (see Figure 5 and Figure 6) is a hexagonal shape and a hexagonal prism in the principal stress space with a longitudinal axis laying on the hydrostatic axis [73].

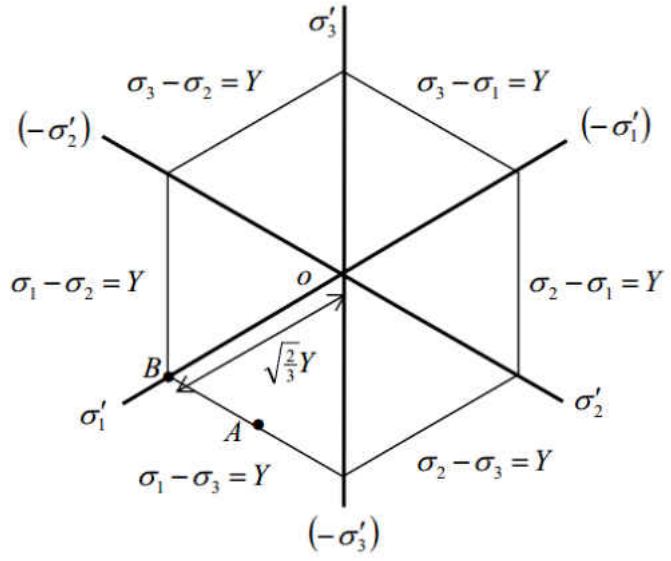

Figure 5: The Tresca criterion in the π-plane [73]

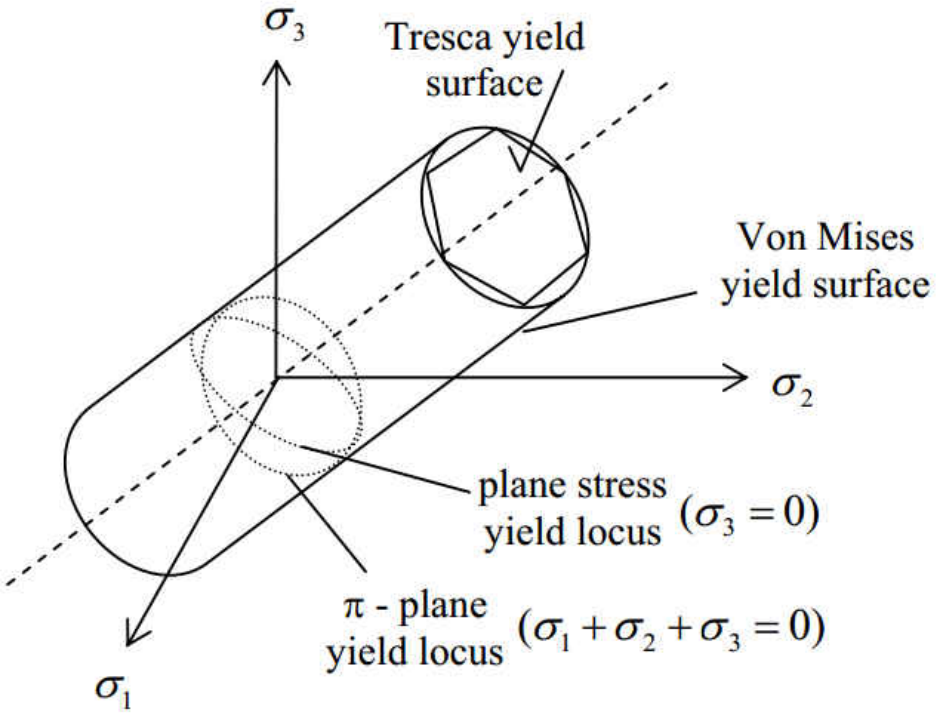

Figure 6: The Von Mises and Tresca yield surfaces in 3D stress space. [73]

2.2.3.2 Von Mises Yield Criteria

At the beginning of the 20th century (1913), von-Mises proposed his phenomenological yield criterion [76]. He proposed a new model that only depends on the second deviatoric invariant J_2 and he postulates that yielding onsets when J_2 equals a yield stress function $K(\gamma)$ of an internal variable. Hence, von-Mises is globally known as J_2 plasticity, referring to second deviatoric invariant. A simple example of a uniaxial stress state will be used to explain the yielding function. The uniaxial stress state tensor and its deviatoric stress tensor are shown in matrices in the following respectively.

$$\sigma = \begin{bmatrix} \sigma & 0 & 0 \\ 0 & 0 & 0 \\ 0 & 0 & 0 \end{bmatrix} \quad (12)$$

$$\sigma' = \begin{bmatrix} \frac{2}{3}\sigma & 0 & 0 \\ 0 & \frac{-1}{3}\sigma & 0 \\ 0 & 0 & \frac{-1}{3}\sigma \end{bmatrix} \quad (13)$$

By the definition, $J_2 = {}^{1}/_{3}\ \sigma^2$ the yield function for the uniaxial stress state is:

$$f(\sigma, \gamma) = \bar{\sigma}(\sigma) - Y(\gamma) \quad (14)$$

where $Y(\gamma) = \sqrt{3K(\gamma)}$ in a uniaxial yield stress and $\bar{\sigma}(\sigma)$ in the von Mises (equivalent) stress defined as:

$$\bar{\sigma} = \sqrt{\frac{1}{2}[(\sigma_{11} - \sigma_{22})^2 + (\sigma_{22} - \sigma_{33})^2 + (\sigma_{33} - \sigma_{11})^2] + 6[\,\tau_{12}^2 + \tau_{23}^2 + \tau_{31}^2\,]} \quad (15)$$

The form of the von-Mises yield surface in the π-plane is a circle with a $\sqrt{3\,J_2}$ radius and shape in a cylindrical form in the principal stress space with a longitudinal axis laying on the hydrostatic axis as in Figure 6 and Figure 7 [73].

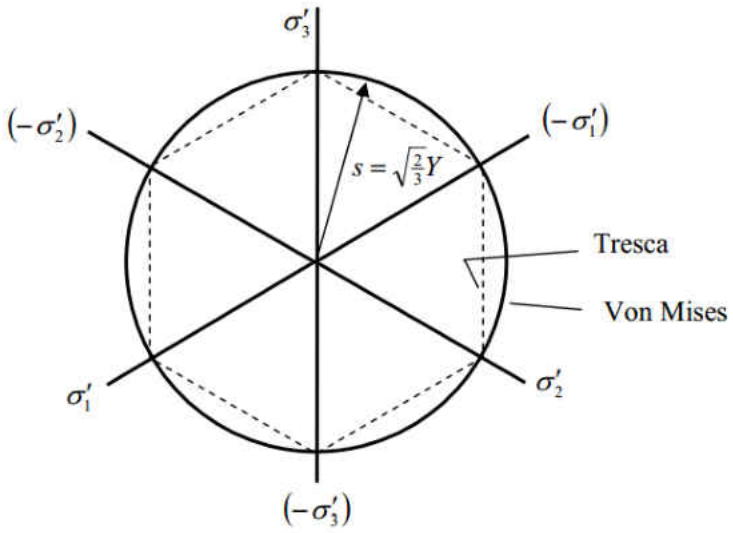

Figure 7: The Von Mises criterion in the π-plane. [73]

2.2.3.3 Isotropic Damage

Any internal degradation of a continuum solid is referred as damage. This definition applies in continuum mechanics. The forms of damage can be micro-voids, cavities, or micro-discontinuities, in general. Since 1950 and on, scientists are trying to represent the damage physically and to attempt to quantify the damage in the laws of continuum mechanics. The first effort to study and quantify internal damage by presenting a scalar that represent damage was by Kachanov [77]. He introduced the idea of measuring internal damage by internal variable factors such as the equivalent plastic strain $\bar{\varepsilon}_{pl}$ without explaining the damage physical meaning. Years later, Rabotnov [78] measured the damage in creep failure due to an internal voids or cracks in the micro-level in a simple way. His proposal was to calculate the damage D by determining the reduction of the cross section area due to the micro-voids as:

$$D = \frac{A - A_o}{A} \qquad (16)$$

where A_o and A are the initial cross section area and the effective load bearing areas of the virgin and damaged materials, respectively [79]. The damage parameter D ranges from $0 \leq D \leq 1$, where $D = 0$ is for a virgin material and $D = 1$ is when the material shows no resistance to load (see Figure 8). In addition, damage evolution is an irreversible process.

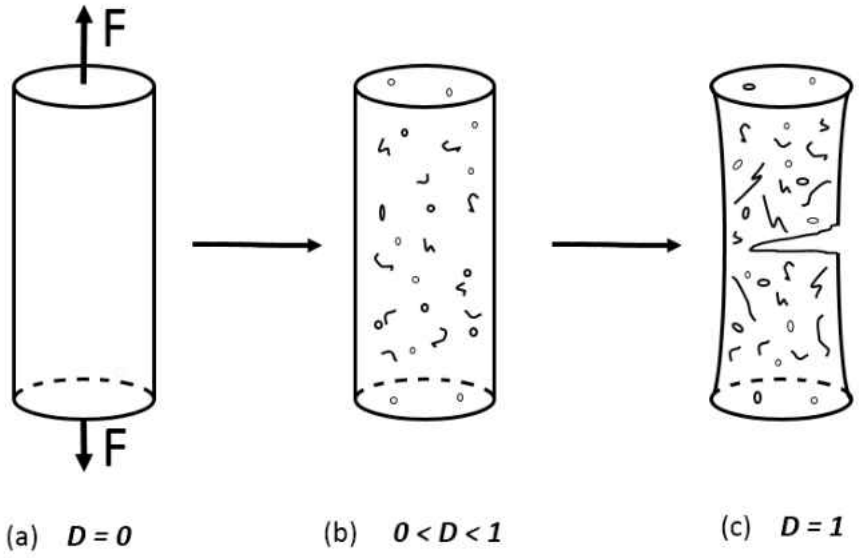

Figure 8. A schematic illustration showing the ductile damage in metals. (a) Virgin material, (b) Nucleation growth of microscopic cracks and voids, (c) voids coalescence and macroscopic fracture.

Since it was plausible to define the damage parameter, the applied original undamaged uniaxial stress σ can be replaced by the effective softened flow stress $\tilde{\sigma}$ where

$$\tilde{\sigma} = \frac{\sigma}{1 - D} \qquad (17)$$

The idea of applying the damage parameter to continuum mechanics was strongly valid throughout the years. Therefore, any continuum constitutive model that includes internal parameters of density or defects will be known as Continuum Damage Mechanics (CDM). In elasto-plastic theory, the damage parameter takes into account the principle of the strain equivalence that makes it a ductile isotropic variable in metals [79-81]. The approach explained above is essentially for isotropic materials. Anisotropic materials damage variable is formed in a fourth-order non-symmetric tensor instead of a scalar. This dissertation will solely focus on damage variable for isotropic materials for the sake of simplicity.

2.2.4 Uncoupled Continuum Material Models

The uncoupled ductile material models do not incorporate damage accumulation the elastoplastic plastic constitutive equation. Therefore, damage accumulation affects the failure only in the uncoupled ductile continuum material models. In other words, plasticity behavior and failure criteria are independent. On the other hand, damage accumulation is incorporated in the elastoplastic model. Thus, damage accumulation affects the elastoplastic and failure in the coupled continuum material models. Example of this is shown below for coupled models

$$f = \sqrt{3\,J_2} - \sigma\left(\bar{\varepsilon}_{pl}\right) \quad (18)$$

and the below equation for uncoupled models.

$$f = \sqrt{3\,J_2} - w(D)\,\sigma\left(\bar{\varepsilon}_{pl}\right) \quad (19)$$

Note that weakening function $w(D)$ is based on the internal damage of the material. It is noteworthy to mention that damage accumulation for ductile materials is based on the plastic strain accumulation $D\left(\bar{\varepsilon}_{pl}\right)$.

In the research domain, the most used models are the uncoupled material models. The foremost advantage of the uncoupled material models is that they are relatively easy to calibrate because of its independence of the weakening function (damage accumulation). In other words, the loading stress update is independent of the weakening due to the internal damage process.

In this dissertation, von-Mises yield function will be used to exhibit the material models. In addition, the development yield surface will be controlled by the isotropic hardening functions. From now on, the internal variable parameter (γ) that was used before will be assigned as the equivalent plastic strain $\left(\bar{\varepsilon}_{pl}\right)$ as the following:

$$\bar{\varepsilon}_{pl} = \sqrt{\frac{2}{3}\,\varepsilon_{pl} : \varepsilon_{pl}} \qquad (20)$$

.The general scenario (flow potential) to explain the elasto-plastic behavior of a material is as:

$$f(J_2, \bar{\varepsilon}_{pl}) = \sqrt{3J_2} - \sigma\left(\bar{\varepsilon}_{pl}\right) \qquad (21)$$

Since we mentioned before that it was more convenient to use the stress triaxiality η and Lode angle parameter $\bar{\theta}$, the general flow potential becomes is as:

$$f(J_2, \bar{\varepsilon}_{pl}, \eta, \bar{\theta}) = \sqrt{3J_2} - \sigma\left(\bar{\varepsilon}_{pl}, \eta, \bar{\theta}\right) \qquad (22)$$

2.2.4.1 Johnson-Cook Model

Johnson-Cook (or J-C) plasticity model is the most phenomenological model in most applications [10]. This is because it considers the strain rate phenomena and the effect of the thermal softening. The potential flow is as:

$$f = \sqrt{3J_2} - \sigma\left(\bar{\varepsilon}_{pl}, \dot{\bar{\varepsilon}}^{*}_{pl}, T^{*}\right) \quad (23)$$

The J-C model consist of three terms: the isotropic plastic strain hardening, the effect of strain rate ($\dot{\bar{\varepsilon}}_{pl}$), and the effect of temperature. Each term is independent of the others. The J-C model is shown below:

$$\sigma\left(\bar{\varepsilon}_{pl}, \dot{\bar{\varepsilon}}^{*}_{pl}, T^{*}\right) = \left[A + B\,\bar{\varepsilon}^{n}_{pl}\right]\left[1 + C \ln \dot{\bar{\varepsilon}}^{*}_{pl}\right]\left[1 - T^{*m}\right] \quad (24)$$

where the constants $A, B, n, C, and\ m$ are material constants, and $\dot{\bar{\varepsilon}}^{*}_{pl}, and\ T^{*}$ are dimensionless plastic strain rate and homologous temperature, respectively.

$$\dot{\bar{\varepsilon}}^{*}_{pl} = \frac{\dot{\bar{\varepsilon}}_{pl}}{\dot{\varepsilon}_{o}} \quad (25)$$

$$T^{*} = \frac{(T - T_r)}{(T_r - T_m)} \quad (26)$$

The reference strain rate, current temperature, room (reference) temperature, and melting temperature are the following parameters $\dot{\varepsilon}_o, T, T_r, and\ T_m$ respectively. This model can be seen extensively built-in in many finite elements code. The internal variable parameter (γ) for J-C model is $\bar{\varepsilon}_{pl}, \dot{\bar{\varepsilon}}^{*}_{pl}, T^{*}$.

J-C damage model [26] was developed two years after J-C plasticity model. It is an accumulation law of three independent parameters: equivalent plastic strain rate ($\dot{\bar{\varepsilon}}_{pl}$), stress triaxiality η, and temperature T as follows:

$$\bar{\varepsilon}_{pl}^{f}\left(\eta,\ \dot{\bar{\varepsilon}}_{pl},\ T\right) = [\,D_1 + D_2\exp(D_3\,\eta)]\,[1 + D_4\ln\dot{\bar{\varepsilon}}_{pl}^{*}\,]\,[1 + D_5\,T^{*}] \qquad (27)$$

where $D_1,\ D_2\ , D_3\ , D_4\ ,\ D_5,\ and\ D_6$ are material constants that needs to be calibrated. The first term in $\bar{\varepsilon}_{pl}^{f}$ is similar to the Hancock and Mackenzie model [47] which is based on Rice and Tracey model [46]. The second and third term presents the fracture strain $\bar{\varepsilon}_{pl}^{f}$ dependency on strain rate and temperature.

J-C damage evolution law is expressed in a numerical simulation code by:

$$dD = \frac{1}{\bar{\varepsilon}_{pl}^{f}(\eta,\ \dot{\bar{\varepsilon}}_{pl},\ T)}\ \dot{\bar{\varepsilon}}_{pl} \qquad (28)$$

The accumulation damage (D) is in an integration form as shown below:

$$D = \sum_{0}^{\bar{\varepsilon}_{pl}^{f}} \frac{1}{\bar{\varepsilon}_{pl}^{f}(\eta,\ \dot{\bar{\varepsilon}}_{pl},\ T)}\ \Delta\bar{\varepsilon}_{pl} \qquad (29)$$

The damage parameter D starts at zero for a virgin material and accumulates damage by means of $\bar{\varepsilon}_{pl}^{f}$ until D reaches unity where the material shows no resistance to load and accordingly fracture occurs.

2.2.4.2 Wilkins' et al. Material Model

Wilkins et al. [82] proposed a strain hardening function that incorporates a scalar parameter A that acts in a same way as the Lode angle parameter. Their A parameter assist in modeling the function of different flow stresses in pure shear and in tension. In addition, it assist in modeling all the stresses in-between. Their A parameter ranges from $0 \le A \le 1$ is expressed in terms of the deviatoric principle stresses:

$$A = \max\left(\frac{\sigma_2'}{\sigma_3'},\ \frac{\sigma_2'}{\sigma_1'}\right) \qquad (30)$$

This model distinguish between two kinds of stress loading: the asymmetric loading or pure shear represented by $A = 0$ and the symmetric loading or uniaxial tension/compression represented by $A = 1$ as in Figure 9. This model uses the equivalent strain hardening to describe the stress flow as:

$$\sigma\left(\bar{\varepsilon}_{pl}, \theta\right) = \sigma\left(\bar{\varepsilon}_{pl}, A\right) = \sigma_t\left(\bar{\varepsilon}_{pl}\right) A^{\lambda} + \sigma_s\left(\bar{\varepsilon}_{pl}\right)\left(1 - A^{\lambda}\right) \quad (31)$$

where σ_t is the equivalent strain hardening functions for uniaxial tension/compression and σ_s is the equivalent strain hardening functions for pure shear/torsion. The power λ is a material parameter for adjusting the yield surface. Note that when λ is 1, it acts as the known J_2 palasticity.

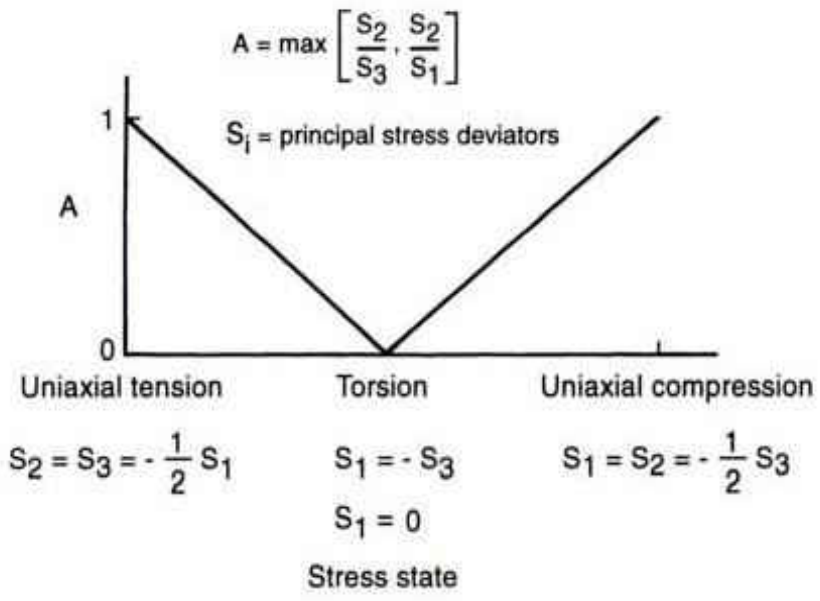

Figure 9: Defenition of the parameter A that depends on the stress state [83].

As for their damage model, plastic strain history controls the model's evolution law along with two separable weighting functions. Their damage model evolution law acts as:

$$dD = w_1(p)\, w_2(p)\, \mathrm{d}\bar{\varepsilon}_{pl} \quad (32)$$

where $w_1(p)$ is the hydrostatic pressure weighting function and $w_2(p)$ is the asymmetric-strain weighting function.

$$w_1(p) = \left(\frac{1}{1+ap}\right)^{\alpha} \quad (33)$$

$$w_2(p) = (2 - A)^{\beta} \quad (34)$$

where $a,\ \alpha\ and\ \beta$ are positive material constants. The hydrostatic pressure ($\sigma_H = -p$) is represented by p.

2.2.4.3 Bai-Wierzbicki Model

A plasticity model that incorporates effects of strain hardening, hydrostatic pressure η, and the Lode angle dependence $\bar{\theta}$ was proposed by Bai and Wierzbicki [4]. The concept of introducing the hydrostatic pressure η in a hardening function was introduced earlier in [63, 84-87]. The potential flow is as:

$$f = \sqrt{3J_2} - \sigma\left(\bar{\varepsilon}_{\mathrm{pl}}, \eta, \theta\right) = 0 \quad (35)$$

The Bai and Wierzbicki model is expressed as:

$$\sigma\left(\varepsilon_{\mathrm{pl}}, \eta, \theta\right) = \sigma\left(\bar{\varepsilon}_{\mathrm{pl}}\right)\left[1 - c_\eta\left(\eta - \eta_o\right)\right]\left[c_\theta^s + (c_\theta^{ax} - c_\theta^s)\left(\gamma - \frac{\gamma^{m+1}}{m+1}\right)\right] \quad (36)$$

$$c_\theta^{ax} = \begin{cases} c_\theta^t & \text{for } \bar{\theta} \geq 0 \\ c_\theta^c & \text{for } \bar{\theta} < 0 \end{cases} \quad (37)$$

The first term is isotropic strain hardening function (see section 2.3.1 for more about isotropic hardening function). The second term is the effect of the hydrostatic pressure on yield where c_η is a material parameter, which needs to be calibrated. The

other parameter η_o is the reference value of stress triaxiality from the reference test. So if the tensile test was calibrated base on smooth round bar, η_o = 1/3, and η_o= -1/3 for cylindrical specimen compressive test, η_o = 0 for torsion test and so on. The third term in this model is the Lode dependence. The Lode angle term consists of four material constants c_θ^s, c_θ^t, c_θ^c, and m that needs to be calibrated. The terms c_θ^s, c_θ^t, c_θ^c are relative and at least one of them equals one. This depends on the type of the calibration test when calibrating the strain hardening function. The parameter γ is the strength difference between von Mises and Tresca in the deviatoric stress plane. The parameter γ is expressed as:

$$\gamma = 6.4641\,[\sec(\theta - \pi/6) - 1] \qquad (38)$$

After modification and normalization, the range of γ is $0 \leq \gamma \leq 1$. In axial symmetry and plane strain conditions, the parameter γ is 1.0 and 0.0, respectively. This model yield surface can breakdown into other famous yield criteria by setting the constants, see Table 2.

Table 2. Contansts setting to attain different well-known yield surfaces.

Yield Criterion	c_η	c_θ^t	c_θ^c	c_θ^s	m
Von-Mises [76]	0	0	0	0	0
Tresca [75]	0	0.866	1	1	$+\infty$
Dracker-Prager [63]	$\neq 0$	0	0	0	0
Pressure-modified Tresca [88]	$\neq 0$	0.866	1	1	$+\infty$

The damage accumulation rule is similar to what was seen in J-C model. However, the damage accumulation here is based on the stress triaxiality η and the normalized Lode angle $\overline{\theta}$. Their fracture locus function has six material constants D_1, D_2, D_3, D_4, D_5, D_6 that need to be calibrated.

$$D = D\left(\bar{\varepsilon}_{pl}\right) = \int_0^{\bar{\bar{\varepsilon}}_{pl}} \frac{d\bar{\varepsilon}_{pl}}{\bar{\varepsilon}_f(\eta, \bar{\theta})} \quad (39)$$

$$\bar{\varepsilon}_{pl}^{f}\left(\eta, \overline{\theta}\right) = \frac{1}{2}\left[\left(\bar{\varepsilon}_{pl}^{f(+)} + \bar{\varepsilon}_{pl}^{f(-)}\right) - \bar{\varepsilon}_{pl}^{f(0)}\right]\overline{\theta}^{2} + \frac{1}{2}\left(\bar{\varepsilon}_{pl}^{f(+)} - \bar{\varepsilon}_{pl}^{f(-)}\right)\overline{\theta} + \bar{\varepsilon}_{pl}^{f(0)}$$

$$= \frac{1}{2}\left[\left(D_1 e^{-\eta D_2} + D_5 e^{-\eta D_6}\right) - D_3 e^{-\eta D_4}\right]\overline{\theta}^{2} + \frac{1}{2}\left(D_1 e^{-\eta D_2} - D_5 e^{-\eta D_6}\right)\overline{\theta} + D_3 e^{-\eta D_4} \quad (40)$$

The term $\bar{\varepsilon}_{pl}^{f(+)}$ shows the fracture locus of the axial symmetric in deviatoric tension ($\overline{\theta} = 1$). The term $\bar{\varepsilon}_{pl}^{f(-)}$ shows the fracture locus of the axial symmetric in deviatoric compression ($\overline{\theta} = -1$). The term $\bar{\varepsilon}_{pl}^{f(0)}$ shows the fracture locus of the shear or plane strain in deviatoric tension ($\overline{\theta} = 0$). A geometrical representation of this fracture locus in the 3D space is shown in Figure 10.

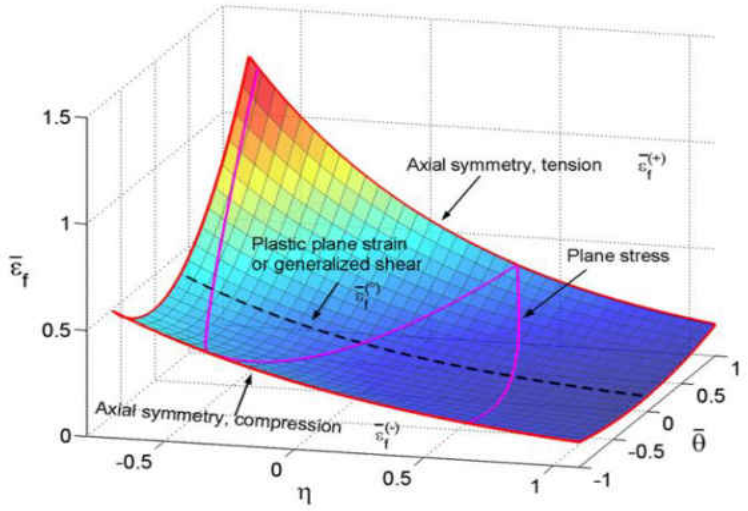

Figure 10. A 3D asymmetric fracture locus of Bai & Wierzbicki model [4]

2.2.5 Coupled Continuum Material Models

The damage-coupled models incorporate a parameter that represents damage accumulation (material degradation) in the elastoplastic model. Each model has its distinctive approach to representing the internal variables of degradation. These internal variables may be load-carrying area, void volume fraction, or distribution of microvoids. As mentioned earlier, the internal damage accumulation is due to voids nucleation, voids growth, and voids coalescence (crack propagation) in the micro level as seen in Figure 8.

In comparison to uncoupled models, damage-coupled models are not easy to calibrate and, therefore, time-consuming. Setting their material constants requires number of experiment tests and data for a better calibration results. The advantages of the damage-coupled models over uncoupled models are that it well predicts the material failure occurrence. Many phenomenological coupled models showed significant success in martial behavior plasticity and failure simulations. For simplicity, the coming

subsections will demonstrate simple coupled models to set a solid background for the reader to visualize the effect of the internal damage on the yielding onset, plasticity behavior, and failure mode. The reader is advised to review the following historical references to know more about coupled models [45, 46, 80-82, 89-100].

2.2.5.1 Modified Johnson-Cook Model

The Johnson-Cook model was modified in 2001 by Børvik et al. [101]. They coupled the J-C plasticity model with an internal variables damage function and adopted the same well-known J_2 yield function:

$$f(\sigma, J_2, D) = \sqrt{3 J_2(\tilde{\bar{\sigma}}, D)} - \sigma\left(\bar{\varepsilon}_{pl}, \dot{\bar{\varepsilon}}_{pl}, T\right) \quad (41)$$

They presented the internal variables of the damage function as the equivalent plastic strain ($\bar{\varepsilon}_{pl}$) and damage (D). The damage evolution rule is expressed in:

$$dD = \begin{cases} 0 & for\ \bar{\varepsilon}_{pl} \leq \bar{\varepsilon}^{d}_{pl} \\ D_c \frac{d\bar{\varepsilon}_{pl}}{\bar{\varepsilon}^{f}_{pl} - \bar{\varepsilon}^{d}_{pl}} & for\ \bar{\varepsilon}_{pl} > \bar{\varepsilon}^{d}_{pl} \end{cases} \quad (42)$$

where $\bar{\varepsilon}^{d}_{pl}$ is the threshold equivalent plastic strain and D_c is the critical limit when material failure occurs. They also have applied the concept of the effective stress tensor $\tilde{\sigma}$ instead of the Cauchy stress tensor σ. Therefore, the equivalent stress ($\bar{\sigma}$) has been changed to the effective equivalent stress $\tilde{\bar{\sigma}}$:

$$\tilde{\bar{\sigma}} = \frac{\bar{\sigma}}{(1-\beta D)} \quad (43)$$

where the parameter β is 0 or 1 to switch from J-C model to the modified J-C model, respectively.

In addition, they introduced a new thermal rate-of-deformation $\dot{\varepsilon}_t$ to the total strain rate tensor as in:

$$\dot{\varepsilon}_t = \alpha \dot{T} \boldsymbol{I} \quad (44)$$

where α is the material thermal expansion coefficient, $\dot{T}$ is the temperature rate, and $\boldsymbol{I}$ is the 2nd order unit tensor.

$$\dot{\varepsilon}_{tot} = \dot{\varepsilon}_e + \dot{\varepsilon}_{pl} + \dot{\varepsilon}_t \quad (45)$$

Finally, the modified J-C model and the modified strain to fracture reads as follows, respectively:

$$\sigma\left(\bar{\varepsilon}_{pl}, \dot{\bar{\varepsilon}}^*_{pl}, T^*\right) = \left[A + B\,\bar{\varepsilon}^n_{pl}\right]\left[1 + \ln \dot{\bar{\varepsilon}}^*_{pl}\right]^C \left[1 - T^{*m}\right] \quad (46)$$

$$\bar{\varepsilon}^f_{pl}\left(\eta, \dot{\bar{\varepsilon}}_{pl}, T\right) = \left[D_1 + D_2 \exp(D_3\,\eta)\right]\left[1 + \ln \dot{\bar{\varepsilon}}^*_{pl}\right]^{D_4}\left[1 + D_5\,T^*\right] \quad (47)$$

where $A, B, n, C, m, D_1, D_2, D_3, D_4, D_5, and\ D_6$ are material constants.

2.2.5.2 Xue-Wierzbicki Model

Another coupled model was proposed by Xue and Wierzbicki [23, 27] in 2008. The advantages of this model are that it is simple and easy to use. It represents the internal variables of the damage function as the equivalent plastic strain ($\bar{\varepsilon}_{pl}$) and damage (D). The weakening function $w(D)$ is introduced in the elastic law: $\sigma = w(D)\boldsymbol{C} : \varepsilon_{el}$ and in the flow potential equation using the von-Mises yield criterion.

$$f = \sqrt{3\,J_2} - w(D)\,\sigma\left(\bar{\varepsilon}_{pl}\right) \quad (48)$$

The damage evolution law is no longer linear with ($\bar{\varepsilon}_{pl}$) as in:

$$dD = m\left(\frac{\bar{\varepsilon}_{pl}}{\bar{\varepsilon}_{pl}^{f}}\right)^{(m-1)} \frac{1}{\bar{\varepsilon}_{pl}^{f}}\, d\bar{\varepsilon}_{pl} \tag{49}$$

The equivalent plastic strain to failure $\bar{\varepsilon}_{pl}^{f}(p,\ \theta)$ is expressed as follows where p is the hydrostatic pressure ($p = \frac{1}{3} I_1$) and θ is the Lode angle.

$$\bar{\varepsilon}_{pl}^{f} = \bar{\varepsilon}_{o}^{f}\left[1 - X_1 \frac{p}{p_{\lim}}\right] \mu_{\theta}(\theta) \tag{50}$$

where $\bar{\varepsilon}_{o}^{f}$, X_1, $p_{\lim}$ are material failure constants. The lode angle dependent function $\mu_{\theta}(\theta)$ have two kinds known as first kind and second kind Lode dependent functions.

$$\mu_{1\theta}(\theta) = \begin{cases} \dfrac{\sqrt{\chi^2 - \chi + 1}}{1 + \left(\frac{\sqrt{3}}{\gamma} - 2\right)\chi} & for \quad 0 \le \chi \le 0.5 \\ \dfrac{\sqrt{\chi^2 - \chi + 1}}{1 + \left(\frac{\sqrt{3}}{\gamma} - 2\right)(1-\chi)} & for \ 0.5 < \chi \le 1 \end{cases} \tag{51}$$

$$\mu_{2\theta}(\theta) = \gamma + (1-\gamma)\left(\frac{6|\theta|}{\pi}\right)^{k} \tag{52}$$

$$\chi = \frac{S_2 - S_3}{S_1 - S_3} \tag{53}$$

where χ is the relative ratio of the principal deviatoric stresses, γ is a material constant of the fracture strain, k the shape parameter.

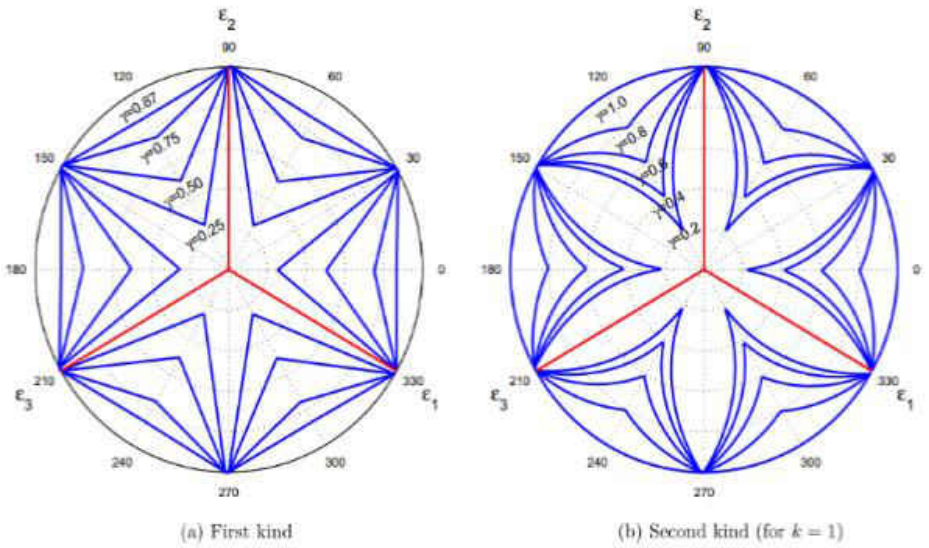

Figure 11. The two kinds of Lode angle dependence functions used in Xue and Wierzbicki.[27].

2.2.5.3 JCXd Model

Recently in 2014, Erice & Galvez [9, 68] postulated a new coupled damage-elastoplastic constitutive model known as JCXd model. Their efforts were primarily gathering two model (J-C model in sec 2.2.5.1 and 2.2.4.1 and Xue-Wierzbicki model sec 2.2.5.2) into one model. The name JCXd is actually decomposed as Johnson-Cook, Xue, and damage. The concept of this model is to have the advantages of each model into one general model. This can be clearly seen in the equation below by adding the weakening function $w(D)$ to the J-C plasticity model and by introducing the two kinds Lode angle dependent function $\mu_\theta(\theta)$ invented by Xue-Wierzbicki to the J-C fracture strain model. Accordingly, the general JCXd coupled model becomes dependent on strain-rate, temperature, Lode angle, and stress triaxiality.

$$\sigma\left(\bar{\varepsilon}_{pl}, \dot{\bar{\varepsilon}}^{*}_{pl}, T^{*}, D\right) = w(D)\left[A + B\,\bar{\varepsilon}^{n}_{pl}\right]\left[1 + C\ln\dot{\bar{\varepsilon}}^{*}_{pl}\right]\left[1 - T^{*m}\right] \quad (54)$$

$$\bar{\varepsilon}^{f}_{pl}\left(\eta, \dot{\bar{\varepsilon}}_{pl}, T, \theta\right) = \mu_{\theta}(\theta)\left[D_1 + D_2\exp(D_3\,\eta)\right]\left[1 + D_4\ln\dot{\bar{\varepsilon}}^{*}_{pl}\right]\left[1 + D_5\,T^{*}\right] \quad (55)$$

$$dD = m\left(\bar{\varepsilon}_{pl}\right)^{(m-1)}\frac{1}{\bar{\varepsilon}^{f}_{pl}}\,d\bar{\varepsilon}_{pl} \quad (56)$$

where m is a material constant.

In summary, Table 3 and Table 4 are set to summarize the coupled and uncoupled models to compare easily among the models and illustrate its dependent parameters.

Table 3. The summary among plasticity models.

Plasticity models	Hydrostatic stress or pressure	J_2	Lode angle θ	Strain rate and temperature	Coupling
Johnson-Cook (J-C) [10]	No	Yes	No	Yes	No
Wilkins et al. [82]	No	Yes	Yes	No	No
Bai-Wierzbicki [43]	Yes	Yes	Yes	No	No
Lemaitre [93, 94]	No	Yes	No	No	Yes
GTN [95-98]	Yes	Yes	No	No	Yes
Modified J-C [101]	No	Yes	No	Yes	Yes
Xue-Wierzbicki [23, 27]	No	Yes	No	No	Yes
JCXd [9, 68]	Yes	Yes	Yes	Yes	Yes

Table 4. The summary among damage models.

Damage models	Hydrostatic stress or pressure	Lode angle θ	Damage evolution law, dD	Strain rate and temperature	Weakening
Johnson-Cook (J-C) [26]	Yes	No	Linear	Yes	No
Wilkins et al. [82]	Yes	Yes	Linear	No	No
Bai-Wierzbicki [43]	Yes	Yes	Nonlinear	No	No
Lemaitre [93, 94]	Yes	No	Nonlinear	No	Yes
GTN [95-98]	Yes	No	Nonlinear	No	No
Modified J-C [101]	Yes	No	Linear	Yes	Yes
Xue-Wierzbicki [23, 27]	Yes	Yes	Nonlinear	No	Yes
JCXd [9, 68]	Yes	Yes	Nonlinear	Yes	Yes

2.3 Hardening Models

There have been extensive studies to understand metals behavior experiencing reversal loading. Studies on models and simulations of the behavior of metals have been increasingly ongoing in research. Accordingly, fatigue failure and crack propagation due to the loading cycles were also investigated. Yielding onset and plastic behavior of metals in each load cycle where found to be controlled and described by two main types of hardening: Isotropic hardening and Kinematic hardening (known as the Bauschinger effects). Isotropic hardening controls the yield surface form and size in the principal stress space during the plastic deformation (see Figure 12).

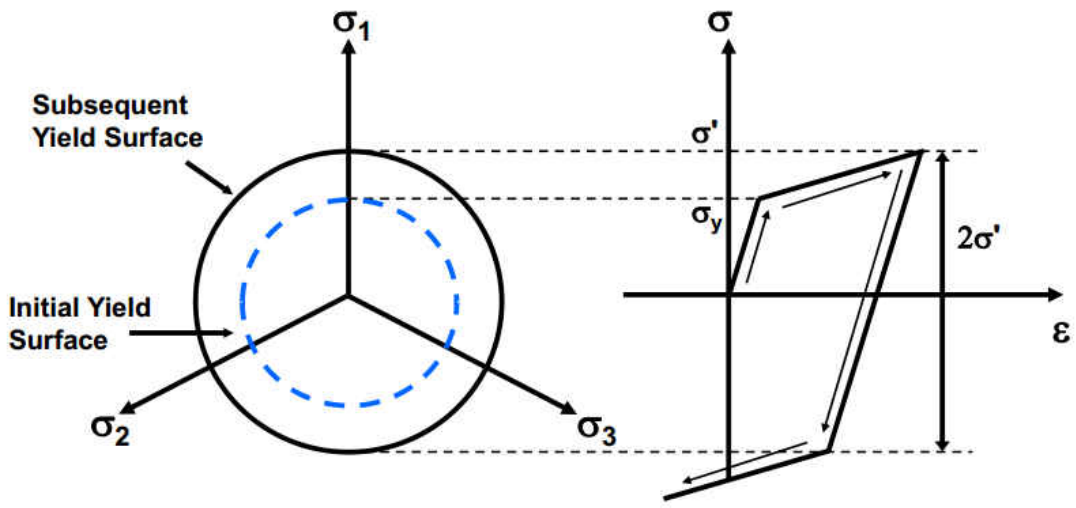

Figure 12: Yield surface expands uniformly during plastic flow [102]

On the other hand, kinematic hardening translates the yield surface in the principal stress space only (see Figure 13). Both isotropic and kinematic hardening describes metal behavior under reverse loading (i.e. tension and compression). In this section, hardening models will be introduced and explained to set a solid knowledge base for the reader.

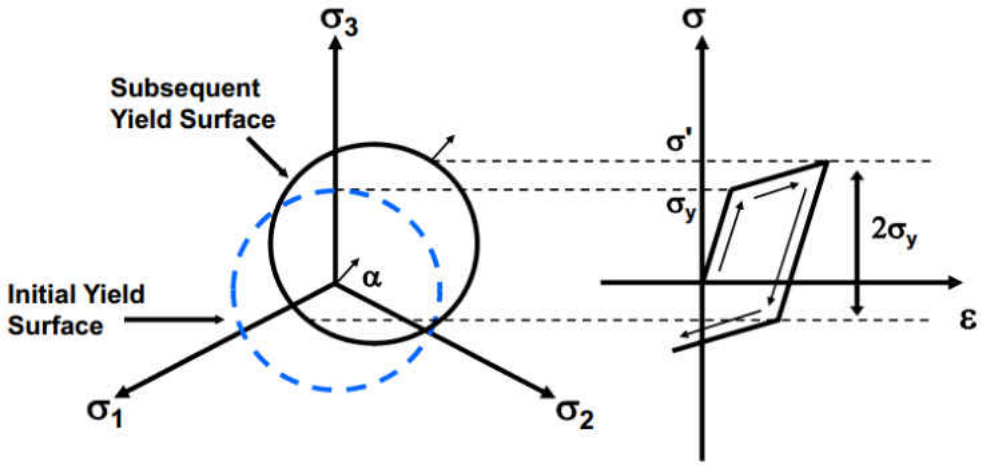

Figure 13: Yield surface translate in the principal stress space in reverse loading [102]

2.3.1 Isotropic Hardening Models

The general form of the flow potential has no effect of the isotropic hardening nor the kinematic hardening where the initial yield here σ_o is in a scalar form.

$$f = \sqrt{\frac{3}{2}\left[S_{ij}\right] : \left[S_{ij}\right]} - \sigma_o = 0 \qquad (57)$$

For the material that behaves isotopically, we substitute σ_o to σ_y, where the yield stress σ_y is a function of the equivalent plastic strain $\bar{\varepsilon}_{pl}$. Accordingly, σ_y increases monotonically as the plastic strain deformation increases.

$$f = \sqrt{\frac{3}{2}\left[S_{ij}\right] : \left[S_{ij}\right]} - \sigma_y = 0 \qquad (58)$$

There are many forms of σ_y equations that simulates the isotropic behavior and the plastic flow of many metals. The most known simple forms that neglects temperature variation and deformation rates are as follows:

The Hollomon equation [103]: $\sigma_y = C\ \bar{\varepsilon}_{pl}{}^{n}$ (59)

The Ludwik equation [104]: $\sigma_y = \sigma_o + C\ \bar{\varepsilon}_{pl}{}^{n}$ (60)

The Swift equation [105]: $\sigma_y = C\ (\varepsilon_o + \bar{\varepsilon}_{pl})^{n}$ (61)

The Samanta equation [106]: $\sigma_y = \sigma_o + C\ \ln \bar{\varepsilon}_{pl}$ (62)

The Voce equation[107, 108]: $\sigma_y = \sigma_s - (\sigma_s - \sigma_o)\ exp\ (-n\bar{\varepsilon}_{pl})$ (63)

The Misiolek equation[109]: $\sigma_y = C\ \bar{\varepsilon}_{pl}{}^{n} \exp(n\bar{\varepsilon}_{pl})$ (64)

where C, n, σ_o, ε_o, σ_s are material constants. The best and common way to calibrate these equations is by conducting a standard tensile test for a round smooth bar to examine the stress–strain curve for a homogeneous material.

2.3.2 Kinematic Hardening Models

It was seen that the isotropic hardening effect was not enough to describe the material behavior in the case of reversal loading. To help simulate the materials' response under reversal loading, kinematic hardening is introduced to illustrate the Bauschinger effect where the yield surface translates in the stress space (see Figure 13.). The Bauschinger effect states that "*Pre-straining in any direction, as defined by the principal axis of the strain tensor, will introduce an anisotropy for further deformation in any other direction. The intensity of this pre-strain-associated anisotropy is at maximum when the direction of further straining is opposite to that of the pre-strain*" [110]. In other words, the tension yielding point and the compression yield point of a material under reversal loading are asymmetric. The kinematic hardening in the flow potential equation is described as:

$$f = \sqrt{\frac{3}{2}\left[S_{ij} - \alpha_{ij}\right] : \left[S_{ij} - \alpha_{ij}\right]} - \sigma_o = 0 \qquad (65)$$

where α_{ij} is the 2nd order tensor backstress. The kinematic and isotropic combined hardening rule becomes:

$$f = \sqrt{\frac{3}{2}\left[S_{ij} - \alpha_{ij}\right] : \left[S_{ij} - \alpha_{ij}\right]} - \sigma_y = 0 \qquad (66)$$

2.3.2.1 Linear Kinematic hardening

Many linear hardening models were proposed since the 1950's. Prager [111] was the first to suggest a linear model to depict a materials' behavior under cyclic loading.

$$d\alpha_{ij} = C\, d\varepsilon_{ij}^{pl} \qquad (67)$$

where $d\varepsilon_{ij}^{pl}$ is the plastic strain increment tensor and C is a material constant. Years later, Ziegler [112] modified Pragers' rule to incorporate the mean stress influence on the kinematic hardening as follows:

$$d\alpha_{ij} = (\sigma_{ij} - \alpha_{ij})d\mu \qquad (68)$$

where $d\mu$ is a multiplier. Although Prager and Ziegler models differ in the Tresca case, they are similar in the von-Mises case [17].

The linear kinematic hardening is capable of portraying the Bauschinger effect but not the ratcheting. Therefore, the need for a model that incorporates tension-compression asymmetry yielding point, Bauschinger effect, and ratcheting raised.

2.3.2.2 Nonlinear Kinematic Hardening

In order to accurately present the materials' behavior under cyclic loading, many nonlinear models were proposed. It started with Mroz model [113] and Dafalias & Popov models [114, 115] presenting a simple bounding surface plasticity model that describes the materials nonlinear kinematic hardening effect. Soon later, new models holding a new concept were proposed [116, 117] that explained the kinematic hardening rule on a two-surface perception: yield surface and bounding surface. The yield surface was to capture the isotropic and kinematic hardening while bounding captures the isotropic hardening only. This notion of two surfaces was significantly modified by Minagawa et al. [118], Bower [119], Mizuno et al. [120], Shen et al. [121], Basuroychowdhury and Voyidjis [122], Montáns [123], Geng and Wagoner [124], Yoshida and Uemori [125-127], and Lee et al. [128]. They all tried to attain a constitutive model with a more realistic behavior. However, the primary difference among these nonlinear kinematic models is in the way of expressing the generalized plastic modulus. The most known and most used nonlinear kinematic hardening model was introduced in 1966 by Armstrong and Frederick (AF) [129]. Its main advantage is that it is relatively straightforward to write a code for a subroutine in any finite element packages. AF model predicts the evolution of the backstress as follows:

$$\dot{\alpha}_{ij} = \frac{2}{3} C \dot{\varepsilon}^{"}_{ij} - B \alpha_{ij} \dot{p} \qquad (69)$$

where $\dot{\varepsilon}^{"}_{ij}$ is the rate of effective plastic strain, C and B are material constants, and $\dot{p}$ is the accumulated plastic strain rate defined as

$$\dot{p} = \sqrt{\frac{2}{3}\,\dot{\varepsilon}^{"}_{ij}\,\dot{\varepsilon}^{"}_{ij}}\,. \qquad (70)$$

Chaboche and co-workers [14-17] improved the ratcheting prediction and better simulates the hysteresis loops under different loading conditions by expanding the AF backstress evolution rule to three compositions (eq.). In other words, Chaboche model decomposes a stable hysteresis loop into three major parts: (1) the initial high modulus at beginning of yielding (α_1), (2) the transient nonlinear part (α_2) and (3) the constant modulus part at a higher strain extent (α_3) [11].

$$\dot{\alpha}_i = \frac{2}{3}\,C_i\dot{\varepsilon}^{"} - B_i\,\alpha_i\,\dot{p}\ \ , \qquad where\ i = 1,2,3,\ldots \qquad (71)$$

$$\alpha\ = \sum_1^n \dot{\alpha}_i \qquad (72)$$

where n is the number of the back stresses This leads to having more material constants to simulate Bauschinger effect accurately, ratcheting effect and combined hardening. To calibrate Chaboche's material parameters, many researchers have been investigating many approaches to explore the easiest and optimum algorithm to attain the material parameters that describe the material behavior under numerous loading conditions [11, 22, 130-133] as in Figure 14.

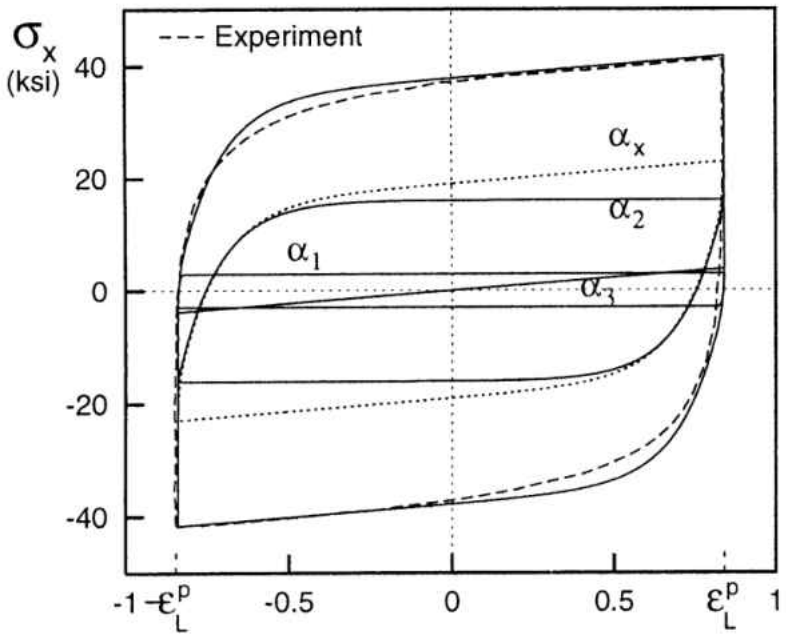

Figure 14: The three decomposed rule of Chaboche model in a strain controlled stable hysteresis loop [11].

2.4 Fatigue life

In cyclic loading, the stress-strain behavior differs from what is seen in a monotonic tension or compression test. The yielding strength, hardening, softening behavior may increase or decrease from a cycle to another. In a stress-strain cyclic loading, the variables used to express the hysteresis loop are the following. The stress range $\Delta\sigma$ is the difference between the maximum stress σ_{max} and the minimum stress σ_{min} in a hysteresis loop.

$$\Delta\sigma = \sigma_{max} - \sigma_{min} \quad (73)$$

The mean stress σ_m is the average of the minimum and maximum stress.

$$\sigma_m = \frac{\sigma_{max} + \sigma_{min}}{2} \quad (74)$$

Likewise, the same definitions that apply for stress may apply to strain. The elastic and plastic strains are defined as below where K', n' and E are the strain hardening coefficient, the strain hardening exponent and elastic modulus, respectively.

$$\varepsilon_{el} = \frac{\sigma}{E} \quad (75)$$

$$\varepsilon_{pl} = \left(\frac{\sigma}{K'}\right)^{1/n'} \quad (76)$$

The total strain range $\Delta\varepsilon_{tot}$ is the summation of the elastic and plastic strain ranges as illustrated in Figure 15.

$$\Delta\varepsilon_{tot} = \Delta\varepsilon_{el} + \Delta\varepsilon_{pl} \quad (77)$$

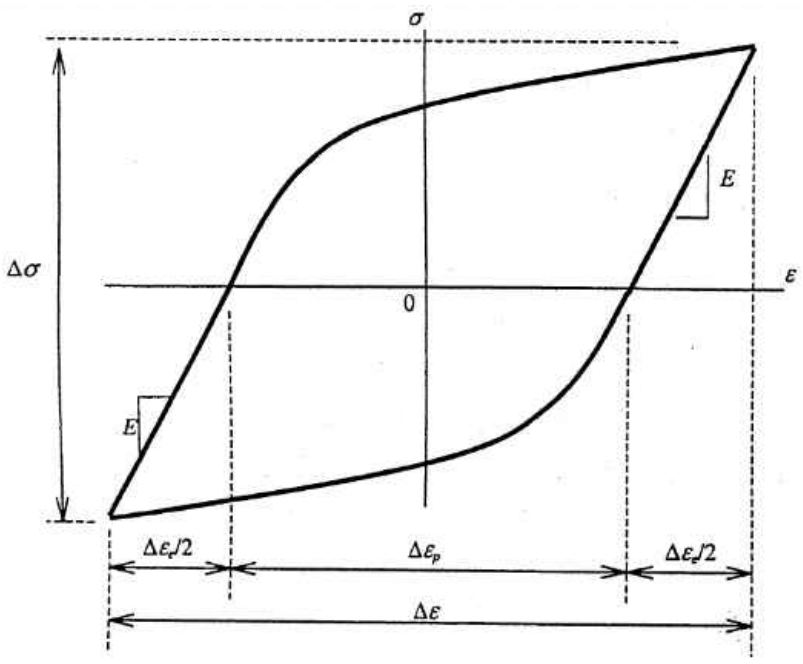

Figure 15: A stable stress-strain hysteresis loop showing strain and stress ranges [134].

The stress amplitude σ_a is half the stress range $\Delta\sigma$ and strain amplitude ε_a is half the strain range $\Delta\varepsilon$.

$$\sigma_a = \frac{\Delta\sigma}{2} \quad (78)$$

$$\varepsilon_a = \frac{\Delta\varepsilon}{2} \quad (79)$$

The stress ratio R_σ and strain ratio R_ε are described as below:

$$R_\sigma = \frac{\sigma_{min}}{\sigma_{max}} \quad (80)$$

$$R_\varepsilon = \frac{\varepsilon_{min}}{\varepsilon_{max}} \quad (81)$$

The Basquin equation [135] presents the strain life equation using the elastic strain term only where σ_f' and b are the fatigue strength coefficient and fatigue strength exponent, respectively.

$$\frac{\Delta\varepsilon_{el}}{2} = \frac{\sigma_f'}{E}(N_f)^b \quad (82)$$

The Coffin-Manson equation [136, 137] presents the strain life equation using the plastic strain term only where ε_f' and c are the strain ductility coefficient and the strain ductility exponent.

$$\frac{\Delta\varepsilon_{pl}}{2} = \varepsilon_f'(N_f)^c \quad (83)$$

The total strain-life equation is the combination of the Basquin equation and the Coffin-Manson equation expressed below and shown in Figure 16. The four fatigue material constants ($\sigma_f',\ b,\ \varepsilon_f',\ and\ c$) can be approximated by many methods such as in Ref. [138-142]

$$\frac{\Delta\varepsilon_{tot}}{2} = \frac{\Delta\varepsilon_{el}}{2} + \frac{\Delta\varepsilon_{pl}}{2} = \frac{\sigma_f'}{E}(N_f)^b + \varepsilon_f'(N_f)^c \quad (84)$$

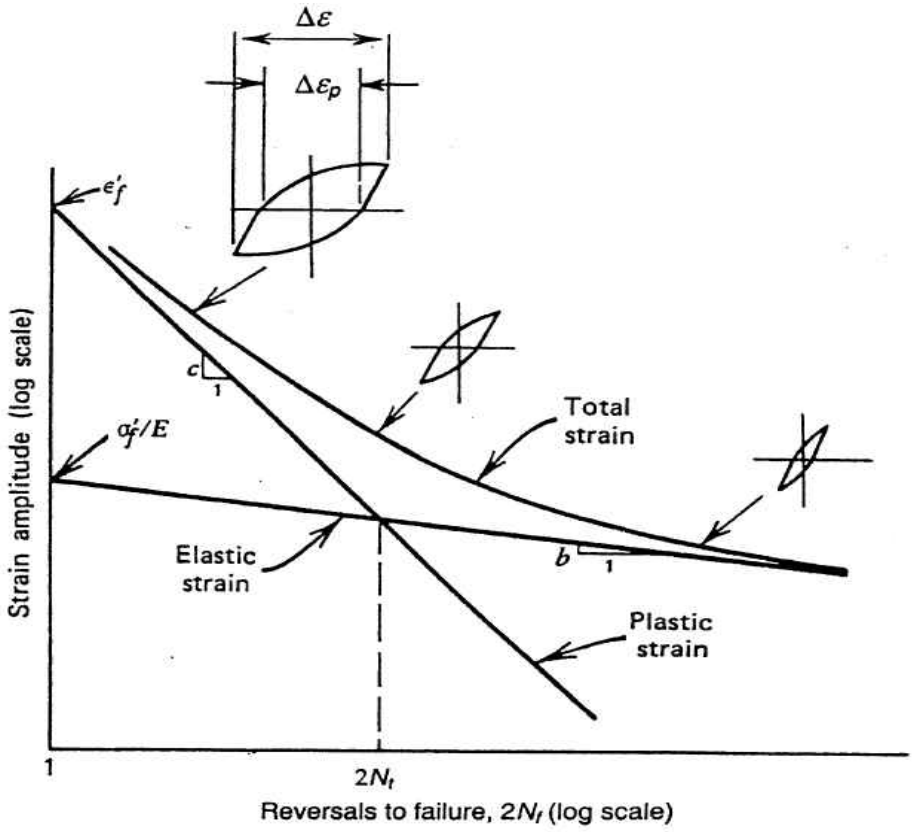

Figure 16: Strain-life curves are showing total strain, elastic strain (Basquin model), and plastic strain (Coffin-Manson model) [134].

The strain-life is expressed in term of cycles (N). To be more precise, the number of cycles to failure will be specified as (N_f) which is the number of cycles for the specimen to fail. It is worth to notice that the strain-based life equation of Basquin and Coffin-Manson equations are for zero mean stress σ_m or known as fully reversed loading $(R_\sigma = -1)$. In a case where the mean stress is not zero, a modified model of Basquin and Coffin-Manson equations known as Modified Morrow includes the effect of the mean stress in the plastic strain part only [143].

$$\frac{\Delta\varepsilon_{el}}{2} = \frac{\sigma_f' - \sigma_m}{E}(N_f)^b \qquad (85)$$

$$\frac{\Delta\varepsilon_{tot}}{2} = \frac{\sigma_f' - \sigma_m}{E}(N_f)^b + \varepsilon_f'(N_f)^c \quad (86)$$

Manson and Halford [144] included the effect of the mean stress in the elastic and plastic strain parts of the strain-life equation.

$$\frac{\Delta\varepsilon_{tot}}{2} = \frac{\sigma_f' - \sigma_m}{E}(N_f)^b + \left(\frac{\sigma_f' - \sigma_m}{\sigma_f'}\right)^{c/b}(N_f)^c \quad (87)$$

It was seen that this model overestimate the mean stress effect on the LCF regimes because of the vast amount of the plastic deformation in this particular regime [145].

CHAPTER THREE:
LINKAGE BETWEEN DUCTILE FRACTURE AND EXTREMELY LOW CYCLE FATIGUE OF INCONEL 718 UNDER MULTIAXIAL LOADING CONDITIONS

3.1 Abstract

Ductile fracture and extremely low cycle fatigue (ELCF) [146] are two common failure modes in aircraft engines and turbomachinery designs; however, the linkage between these two failure modes under multi-axial loading conditions has never been systematically studied. Inconel 718 (IN718) is one type of high temperature alloys widely used in turbomachines. Specially designed specimens and tests were used to achieve desired multi-axial loading conditions. Two groups of tests were conducted: (a) round bar specimens with different notches; (b) plane strain specimens. Similar types of tests were conducted for IN718 under both types of failure modes (ductile fracture and ELCF). It is found that the ductile fracture of IN718 under multi-axial loading conditions is strongly dependent on stress triaxiality, but weakly dependent on the Lode angle parameter [4]. A 3D fracture locus was calibrated using modified Mohr-Coulomb (MMC) criterion proposed by Bai and Wierzbicki [25]. It is found that the same phenomenon of stress state dependency exists in the ELCF, which need to be addressed. The mechanism linkage between these two failure modes was explored.

3.2 Introduction

Ductile fracture is an important failure mode for many materials and structures including turbomachines. For example, the foreign object damage (FOD) on the blade

and casing is a design factor in aircraft engines and turbomachinery under extreme loading conditions [70], Here are two examples of FOD on turbomachines. The first one is bird/ice/hail strike on aircraft engines fan blades and further ingestion into the engine hot sections, which may cause blade out and further damage on engine casing. Each year, bird and other wildlife strikes to aircraft (including engines and fuselage) cause more than $600 million in damage to U.S. civil and military aviation [147]. The second one is the bolts and nuts (or other hard bodies) passing screen and ingestion into gas/steam turbines, which may cause damage on high speed rotating blades. One critical technique here is the accurate prediction of ductile fracture under complex loading conditions. Extremely low cycle fatigue (ELCF) is another critical failure mode for turbomachinery. For example, the damage caused by frequently turning on and off in gas turbines. It is also one of important failure mechanisms of aircraft engine casings under blade out events, which can be caused by, for instance, foreign object impacts as described above.

Fatigue crack growth and life prediction of Inconel 718 was studied by Chen et al. [148] at different temperatures. They discovered that the fatigue strength is considerably lesser at room temperature than at elevated temperature. A recent published paper by Shamsaei et al. [149] studied the fatigue life estimation of Inconel 718 when subjected to multiaxial loading based on their basic tensile properties and the without using any fatigue data. It was found that fatigue life could be estimated using simple tensile properties and suitable damage models. Lately, Ince & Glinka [150] proposed a generalized fatigue damage parameter for multiaxial fatigue life prediction. This new parameter was examined using steel and Inconel 718 superalloy. Their numerical results

show good agreement with the experimental data. Generally, low cycle fatigue under multiaxial loading damage models (strain-based models) has shown great results and correlations. Strain based damage models implicitly incorporates the significance of the plastic deformation [151-155].

The common thing between these two failure modes is that notable plastic deformation is involved before material failure. Material fatigue failure can be divided into three groups: high cycle fatigue, low cycle fatigue and extremely low cycle fatigue. The ductile fracture can be treated as an extreme case of ELCF with only 1/4 cycle. The ELCF is the bridge to link the fatigue and fracture mechanics. Study on ductile fracture and ELCF of Inconel 718 (IN718) under multiple axial loading conditions and failure mechanism/linkage of these two failure modes is the main subject of this paper. The chemical composition of IN718 studied by the authors is listed inTable 5: Material composition of the used IN718.

Table 5: Material composition of the used IN718

Element	Content wt%	Element	Content wt%
Ni	52.90	Al	0.58
Cr	18.41	Co	0.19
Mo	2.89	C	0.04
Cb+Ta	5.17	S	0.0005
N	0.0078	Mn	0.09
Si	0.08	B	0.004
Cu	0.06	P	0.007
Fe	Bal.		

3.3 Multiaxial Ductile Fracture

Multiaxial ductile fracture under monotonic loading condition is the baseline for studying ELCF. Four types of specimens (Figure 17) are designed and tested: smooth round bars (denoted by type R0), round bar with notch ratio 1 ($\frac{a}{R} = \frac{0.125"}{0.375"} = \frac{1}{3}$) where a is the minimal cross-section radius, and R is the notch radius, denoted by type R1), round bar with notch ratio 2 ($\frac{a}{R} = \frac{0.125"}{0.125"} = 1$, type R2), and plane strain tension (denoted by type PE). The dimensions of all four different specimens shape are clearly shown in Figure 18, and all units declared are mm in the drawings.

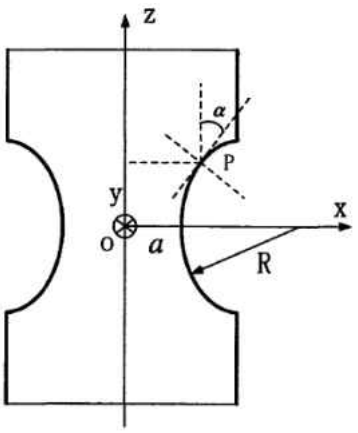

(a)

(b)

Figure 17: (a) Symbol notation of the cross section of a notched specimen (b) Four different shapes of the specimens before fracture.

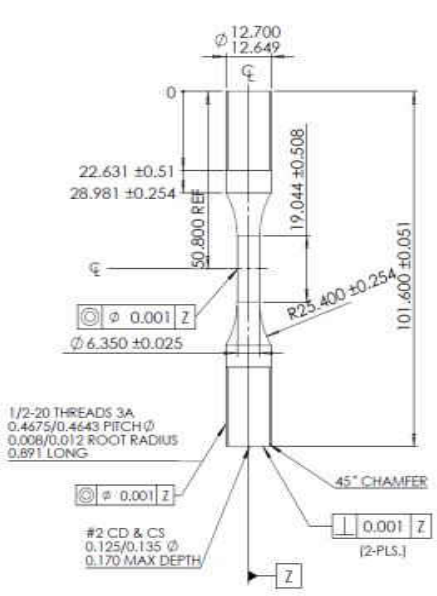

(a)

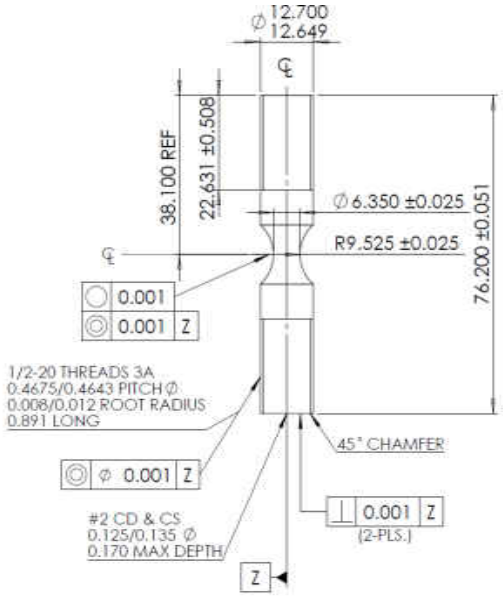

(b)

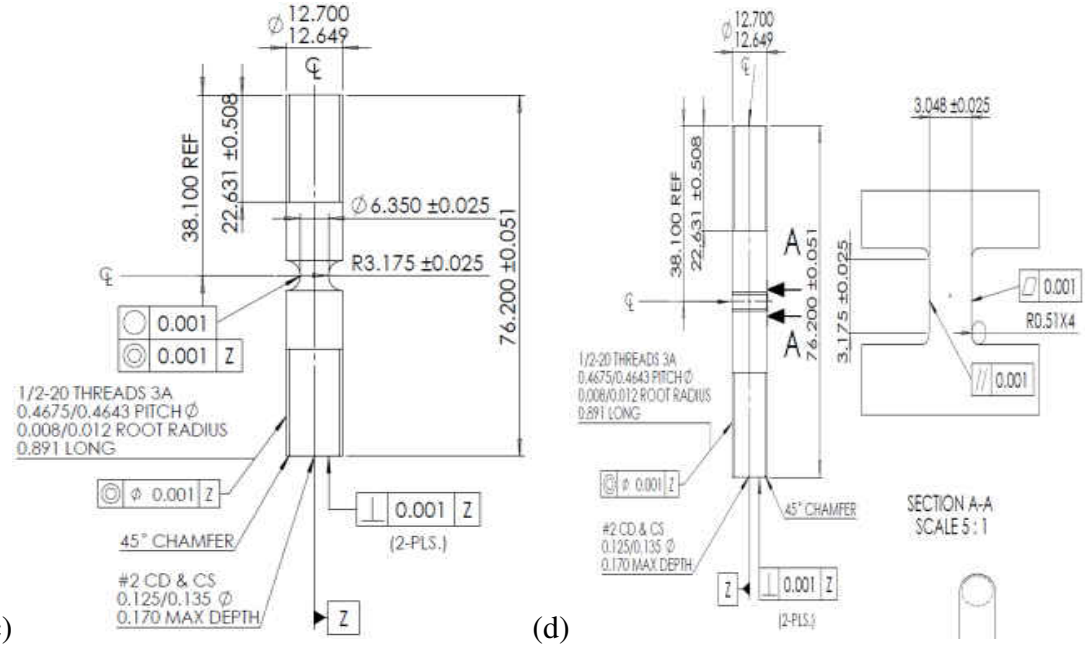

Figure 18: Drawings show different dimensions of four types of specimens. The specimens notation used are R0, R1, R2, and PE (a, b, c, and d, respectively)

All the tests were conducted at room temperature and quasi-static loading conditions at a MTS servo-hydraulic testing machine. The used MTS hydraulic machine has a capacity of 100kN. A collection of one of each specimen before testing is shown in Figure 17(a). The fractured surfaces of specimens are shown in Figure 20. Cup-cone failure modes and slant fracture surface indicate that the fracture is shear dominated. The material initial yield stress is about 1050MPa, and the engineering stress-strain curve is shown in Figure 19(a). The material strain hardening can be described by the following power hardening law, $\bar{\sigma} = 1480.3\bar{\varepsilon}^{\,0.0813}$.

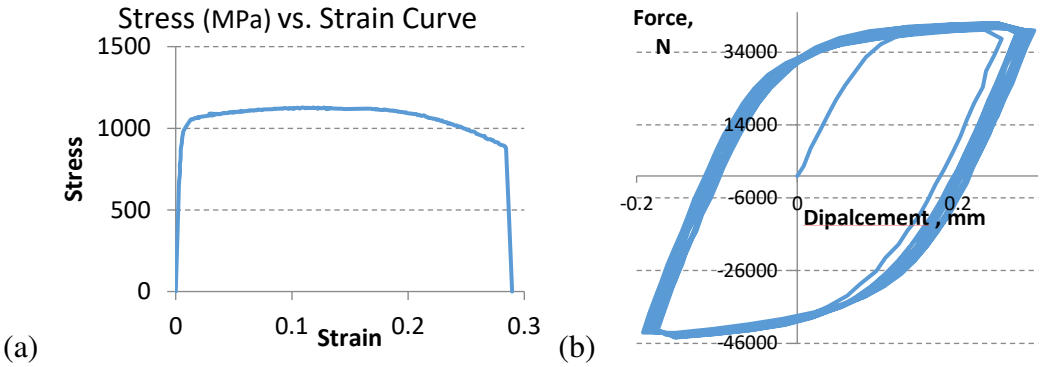

Figure 19: (a) Engineering stress vs. strain hardening curve obtained from smooth round bar specimen (R0). (b) One example of the displacement controlled extremely low cycle fatigue test for R1 notched specimen.

Figure 20: (a) The specimens were spray painted in black and white before the ELCF test for optical measurement and digital imaging correlation (DIC). From left to right are R0, R1, R2, and PE, respectively. (b) Fractured specimens after ELCF tests of R1 (a/R=1/3, left) and R2 (a/R=1, right)

The classical Mohr-Coulomb criterion was extended by Bai and Wierzbicki [25] to describe ductile fracture under multi-axial loading conditions. This model is referred as the modified Mohr-Coulomb (MMC) model. The equivalent plastic strains to fracture of all tests are directly measured by area reduction or thickness reduction. The stress triaxiality and Lode angel parameter are calculated using derived analytical solutions

[43]. For round specimens (R0, R1, & R2), the Lode angle parameter is $\overline{\theta} = 1$, and the stress triaxiality η can be estimated using the Bridgman equation (Eq. (88)).

$$\eta = \frac{1}{3} + \ln\left(1 + \frac{a}{2R}\right) \quad (88)$$

$$\eta = \frac{\sqrt{3}}{3}\left[1 + 2\ln\left(1 + \frac{a}{2R}\right)\right] \quad (89)$$

For plane strain specimens, the Lode angle parameter is $\overline{\theta} = 0$, and Eq. (89) is used for stress triaxiality [43]The calibrated 2D and 3D fracture locus using MMC model are shown in Figure 21. Note that the stress triaxiality and Lode angle parameter are used to describe different stress states under multi-axial loading conditions. Experiment results show that the fracture limits of IN718 are strongly dependent on the stress triaxiality and weak dependent on the Lode angle parameter.

(a)

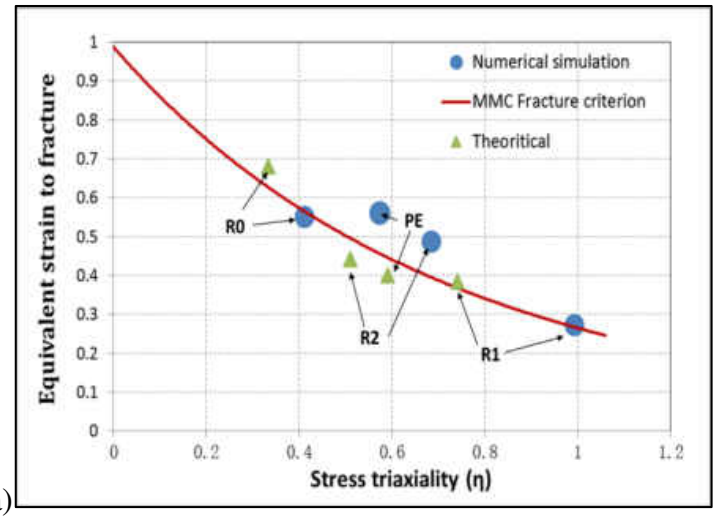

(b)

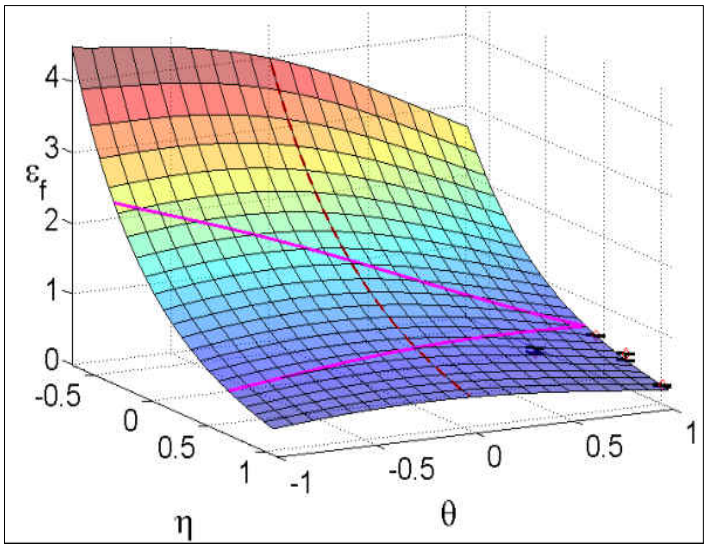

Figure 21: (a) Calibrated ductile 2D fracture locus of IN718 and a generic 3D fracture surface with the Lode angle dependency. (b) 3D fracture locus of IN718. Stress triaxiality is denoted by η, Lode angle parameter θ, and equivalent strain to fracture εf

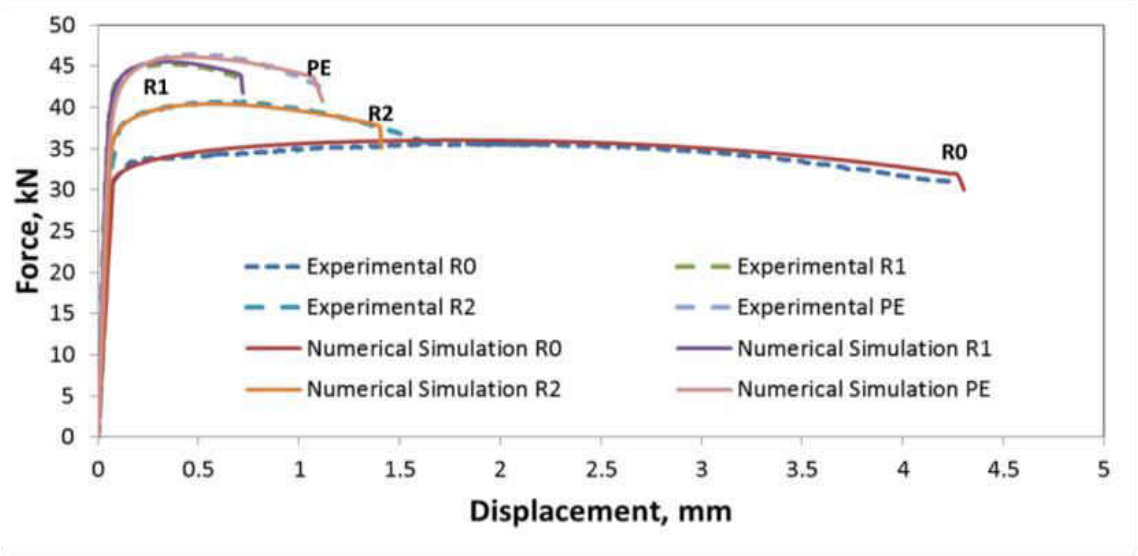

Figure 22: The applied modified Mohr-Coulomb failure criterion in Finite Elements simulations shows good agreement with the experimental results in monotonic ductile fracture tests.

3.4 Extremely Low Cycle Fatigue

Fully reversed displacement controlled fatigue tests were conducted on the same type of specimens as ductile fracture tests to calibrate the ELCF properties of IN718. The test had a total number of 16 specimens with 4 pieces for each shape. Before testing, the estimated numbers of cycles to failure range from 5 to 100 cycles. Note that the real cycles to failure were different. Real failure cycles are used when the data are presented in strain life diagram. Digital Imaging Correlation (DIC) was utilized to capture the full field strain and determine strain amplitude during tests. The force displacement hysteresis loops were observed and recorded by the help of the DIC. It is noticeably observed in Figure 19.(b) that the plasticity of Inconel 718 should be described using a combined

hardening law (isotropic and kinematic hardening). The tests were run until total failure and the numbers of cycles were counted.

The measured strain results are divided into two parts: elastic strain amplitude and plastic strain amplitude for ELCF (see Eq.(90)). Using Eqs. (91) & (92) and with accurate measurements of the changes in the diameters and axial displacement during the ELCF tests by the help of the DIC, we can measure the changes of the total strain in each cycle during tests. Eq. (91) is used for R0, R1, and R2 while Eq. (92) is only applied for plane strain (PE) stress state. The strain in each cycle for specimen R1 is presented in Figure 23.

$$\bar{\varepsilon} = \bar{\varepsilon}_e + \bar{\varepsilon}_p \qquad (90)$$

$$\bar{\varepsilon} = 2 \ln\left(\frac{D_0}{D}\right) \qquad (91)$$

$$\bar{\varepsilon} = \frac{\sqrt{3}}{2} \ln\left(\frac{L}{L_0}\right) \qquad (92)$$

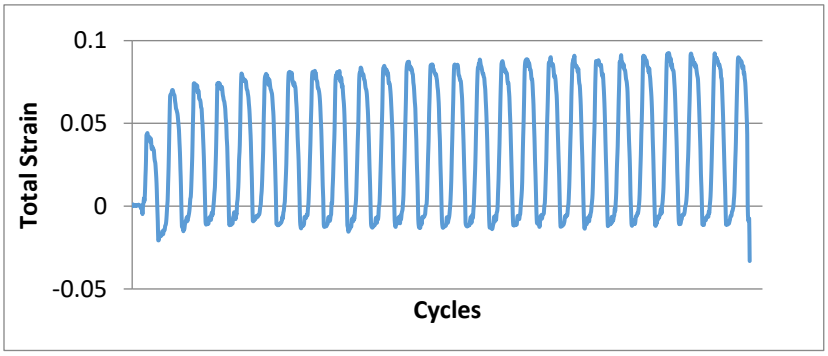

Figure 23: Total Strain vs. cycles for specimen R1.

These results are illustrated in the strain life curve, as shown in Figure 24. The fractured specimens of two ELCF tests are shown in Figure 24.

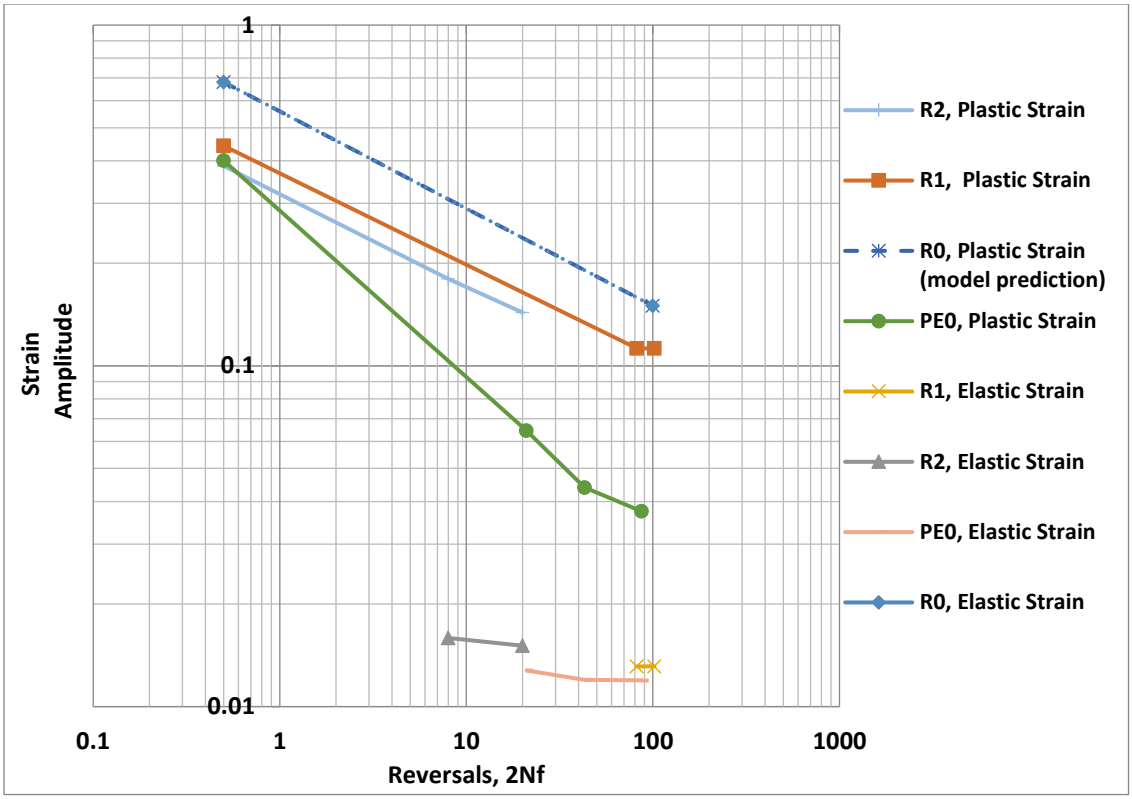

Figure 24: Dependence of fatigue life on plastic strain and different stress states (each cycle has two strain reversals)

The results shown in Figure 24 can tell us that fracture strain's strongly dependency on stress states (due to the difference of stress triaxiality and Lode angle parameter) give different starting points at 1/4 to failure in strain-life plot. These differences have propagated to the region of ELCF. It should be noted that the data point of smooth round specimen (R0) at 100-cycle ELCF is from model estimation because significant buckling was found in the compression loading and tests were stopped.

3.5 Conclusion and Discussion

This paper presents results on ductile fracture of IN718 under multi-axial loading conditions, which is achieved by novel design of specimen geometry. Four types of specimens are used to calibrate the fracture of IN718. It is found that ductile fracture strain of IN718 is strongly dependent on the stress states, especially the stress triaxiality. This phenomenon is usually contributed to the effect of hydrostatic pressure on the micro void growth and nucleation rate. The ELCF tests on IN718 on the same group of specimens indicate that the similar pressure dependent mechanism applies to ELCF, which was seldom addressed in the literatures. This paper presents a novel method using stress triaxiality to describe the notch effect on material fatigue.

The current tests were conducted under room temperature, quasi-static loading and fully reverse loading conditions. The effect of frequency, temperature, and loading history effects will be needed to investigate as well, and the coupling effects of these parameters should also be studied in the future.

CHAPTER FOUR:
A STUDY OF INCONEL 718 DEPENDENCY ON STRESS TRIAXIALITY AND LODE ANGLE IN PLASTIC DEFORMATION AND DUCTILE FRACTURE

4.1 Abstract

A numerical and experimental study of monotonic tensile tests on Inconel 718 with different stress states has been investigated. Focus was put to dependencies of stress triaxiality and Lode angle parameter on plastic behavior and ductile fracture. The constitutive plasticity model proposed by Bai and Wierzbicki [4] and the modified Mohr-Coulomb (MMC) ductile fracture model [25] were adapted with suitable extensions. Experimental results were used to calibrate the models. By setting up parameter optimization for model calibration, the experimental results and numerical simulations were well correlated. Finally, the MMC fracture model well predicted both fracture initiation and fracture propagation modes.

4.2 Introduction

Inconel 718 is a nickel-base high temperature super alloy, which is used in space navigation, nuclear industries, power plants, shipping industries, and extensively used in gas turbine engine hot section parts. Its weldability is deemed good because of its resistance to strain-age cracking. However, it is known to be very difficult for machining, forging and fabrication manufactures due to its high hardness and toughness. Inconel 718 can be widely found in high temperature applications due to its high strength and

corrosion resistance at high temperature. The melting point of this material is about 1336°C.

Ductility is defined as the ability of a material to accept large amounts of plastic deformation without crack [42]. Bai and Wierzbicki [4] have proposed a new model for metal plasticity and ductile fracture that includes the effect of the hydrostatic pressure (related to the stress triaxiality) and the effect of the third invariant of the deviatoric stress tensor. The effect of the hydrostatic pressure is responsible for controlling the size of the yield surface whereas the effect of the third invariant of stress deviator is responsible for the shape of the yield surface [156]. An efficient numerical integration algorithm for this model was presented in Ref. [44], where the simulation results in finite element (FE) analysis are satisfactory.

Decades ago, McClintock [45], Rice and Tracey [46], Hancock and Mackenzie [47], Hancock and Brown [48] have showed that ductile fracture strain is a function of the hydrostatic pressure (stress triaxiality). As a result, the Johnson-Cook ductile fracture model [26] was provided and widely used. On the other hand, many ongoing numerical and experimental studies on ductile materials have verified that a new parameter (along with the stress triaxiality) needs to be considered in predicting the ductile fracture. This parameter is the third invariant of deviatoric stress tensor (which is related to the Lode angle). It plays a key role in providing a better fracture prediction along with the stress triaxiality [4, 5, 7, 8, 25, 49-55]. These intense research works showed decisive relation of the Lode angle to predict correctly ductile material failure. An extension to the classical Mohr-Coulomb fracture criterion was postulated in Ref. [25] under assumption

of proportional loading and asymmetric metal plasticity (considering both the pressure sensitivity and the Lode angle dependence). This model predicts shear fractures as well as tensile cracks under multiaxial loading conditions. Over the past few years, this model has been successfully applied to various applications, especially the metal sheet ductile fracture [6, 38, 56-60].

Inconel 718 was tested to calibrate a multiaxial constitutive model that accounts for the strength-differential [61]. The term "strength-differential" means different plastic flow behavior under uniaxial tension and uniaxial compression. This multiaxial constitutive model differs from the classical metal plasticity by adding all three stress-invariants in its yield function. This promising model is a general form of Durcker [62] and Drucker-Prager [63] models. The plastic deformation behavior of Inconel 718 at different strain rates was studied in Refs. [64, 65] and [66] using the Johnson-Cook (J-C) constitutive relation [10]. Nevertheless, the J-C plasticity model does not take the stress triaxiality ratio nor the Lode angle into account. A study was reported in Ref. [67] to investigate the effect of superimposed hydrostatic pressure using a pressure vessel. The pressure used ranges from 210 to 630 MPa using Ar gas. It was concluded that the plasticity of Inconel 718 is independent of superimposed ambient hydrostatic pressure.

Recently, Inconel 718 is tested to validate a coupled elastoplastic-damage constitutive model with Lode angle dependent failure criterion by Eric and Galvez [9]. This model introduced a new factor, called the weakening function, to the classical Johnson-Cook relationship [10]. It was shown that the combination of a Lode angle dependent failure criterion with weakened constitutive equations is necessary to predict

fracture patterns of the mechanical tests performed and provide reliable results. The same research group [68] investigated the ductile failure of Inconel 718 superalloy under quasi-static and impact loading using the proposed hardening model and the coupled elastoplastic-damage constitutive model with failure criterion [9].

In comparison, this paper will study the plasticity and ductile fracture of Inconel 718 using the recent uncoupled continuum plasticity model proposed by Bai and Wierzbicki [4] and the modified Mohr-Coulomb (MMC) ductile fracture criterion [25]. Mechanical tests under different stress states are designed and conducted. Numerical simulations are set up using ABAQUS/explicit to provide information when direct measures are not possible. The material model of plasticity and fracture was implemented in ABAQUS non-linear code by means of a user defined material subroutine (VUMAT). The results show strong stress state effects on the plastic behavior and the ductile fracture of this material, which can be described by the combination of stress triaxiality and Lode angle parameter. Excellent correlation between FE simulations and experimental results are achieved. By introducing the element or material softening behaviors after fracture initiation, the proposed model can well predict not only the fracture initiation but also the correct fracture propagation modes.

4.3 Material description

Inconel 718 is a polycrystalline nickel-base superalloy with high content of Cr and Fe. The phases presented in Inconel 718 are austenitic with FCC structure. Its chemical composition (as received) in %wt. is shown in Table 6. Inconel 718 superalloy

is used in many aggressive applications due to its superior properties like wear resistance, high corrosion and creep resistance at high temperatures, and high melting temperatures. This encourages industries to use it in power plants and rotary parts in gas turbine engines such as blades and disks.

Table 6: Chemical composition in %wt. of Inconel 718 as received for testing.

Ni	Cr	Mo	Cb + Ta	N	Si	Cu	Al	C	S	Mn	P	Fe
52.9	**18.41**	**2.89**	**5.17**	**0.0078**	**0.08**	**0.06**	**0.58**	**0.04**	**0.0005**	**0.09**	**0.007**	**Bal.**

4.4 Characterization of stress state

This paper is primarily to investigate Inconel 718 dependencies of stress triaxiality (η) and Lode angle (θ) on its plastic behavior and ductile fracture modes. The Bai-Wierzbicki plasticity model and the MMC fracture criterion are formulated in terms of the stress triaxiality (η, normalized pressure) and the Lode angle parameter ($\bar{\theta}$). For a given stress tensor [σ] and its stress deviator[S], three stress invariants (p, q, r) can be expressed by the following equations [4, 7, 157-167].

$$\mathrm{p} = -\sigma_{\mathrm{m}} = \frac{1}{3}\,\mathrm{tr}([\boldsymbol{\sigma}]) = -\frac{1}{3}(\,\sigma_1 + \sigma_2 + \sigma_3\,) \tag{93}$$

$$\mathrm{q} = \bar{\sigma} = \sqrt{3J_2} = \sqrt{\frac{3}{2}\,[\mathbf{S}] : [\mathbf{S}]} = \sqrt{\frac{1}{2}[(\sigma_1-\sigma_2)^2 + (\sigma_2-\sigma_3)^2 + (\sigma_3-\sigma_1)^2]} \tag{94}$$

$$\mathrm{r} = \left[\frac{27}{2}\det([\mathbf{S}])\right]^{1/3} = \left[\frac{27}{2}(\sigma_1 - \sigma_{\mathrm{m}})(\sigma_2 - \sigma_{\mathrm{m}})(\sigma_3 - \sigma_{\mathrm{m}})\right]^{1/3} \tag{95}$$

$$[\mathbf{S}] = [\sigma\,] + \mathrm{p}[\mathbf{I}] \tag{96}$$

Here, [S] and [I] are the deviatoric stress tensor and the identity tensor, respectively. The three principle stresses are denoted by σ_1, σ_2, and σ_3 and it is usually assumed that $\sigma_1 \geq \sigma_2 \geq \sigma_3$. Note that the pressure $\boldsymbol{p}$ is positive when a compression load is applied, while $\boldsymbol{\sigma_m}$ is positive in tension. Stress triaxiality (η) is a dimensionless hydrostatic pressure defined by

$$\eta = \frac{-p}{q} = \frac{\sigma_m}{\bar{\sigma}} = \frac{\sigma_1 + \sigma_2 + \sigma_3}{3\bar{\sigma}} \tag{97}$$

For more analogy to explain the concept of stress triaxiality and Lode angle, a 3-D differential volume having three-principle stress (σ_1, σ_2, and σ_3) can be geometrically represented in the Cartesian coordinate system as illustrated in Figure 25. The stress triaxiality becomes

$$\eta = \frac{\sigma_m}{\bar{\sigma}} = \frac{\sqrt{2}}{3} \frac{|\overrightarrow{OO'}|}{|\overrightarrow{O'P}|} \tag{98}$$

The Lode angle (θ) is defined on the deviatoric plane (or π plane), and it is known as the angle between the stress tensor that passes through the deviatoric plane and the axis of the principal stresses.

$$\tan\theta = \frac{2\sigma_3 - \sigma_2 - \sigma_1}{\sqrt{3}(\sigma_2 - \sigma_1)} \tag{99}$$

In addition, Lode angle can be written in a way to show the relation with the normalized third deviatoric stress invariant [168, 169] by the following equation.

$$\xi = \left(\frac{r}{q}\right)^3 = \cos(3\theta) \tag{100}$$

The range of the Lode angle is $0 \leq \theta \leq \pi/3$, and consequently the range of ξ is $-1 \leq \xi \leq 1$. Thus, the Lode angle also can be normalized and known as the normalized Lode angle or Lode angle parameter ($\bar{\theta}$) [156].

$$\bar{\theta} = 1 - \frac{6\theta}{\pi} \tag{101}$$

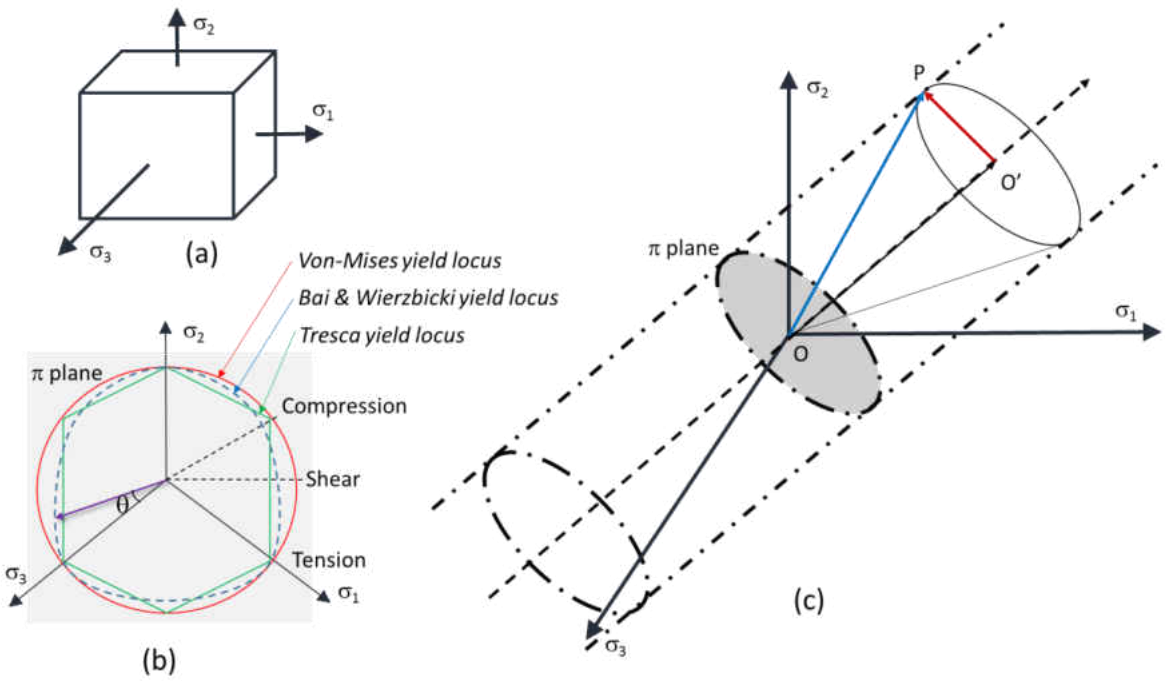

Figure 25: (a) Differential volume with principal stress axes, (b) Lode angle definition on the π-plane, the red circle shape represents von-Mises yield locus, the green hexagon shape represents Tresca yield locus, and the dotted line shape represent Bai-Wierzbicki yield locus, (c) schematic representation of an arbitrary stress state on the space of three principal stresses [4]

4.5 Design of Specimen

In this study, specimens of four different shapes were tested. The four distinctive shapes are a smooth round bar, a round bar with small external circular notch, a round bar with large external circular notch, and a flat plane strain bar. Three-dimension (3D) sketches and real machined parts for these geometries are illustrated in Figure 26 and Figure 27. In addition, more information about detail dimensions is demonstrated in Figure 28, Figure 29, Figure 30 and Figure 31. These geometries are designed in a way to

ensure fractures initiate at desired stress states. Also, there are analytical solutions of stress state parameters available for these specimens. These four types of specimen will help to study the stress triaxiality and Lode angle dependencies on plasticity and fracture. To easily distinguish each specimen, the Table 7 explains the denotation used hereinafter.

Table 7: Denotation of sample names with their key dimensions (unit: mm)

Specimen type	**Denotation**	**Notch radius**	**Minimum diameter**	**Minimum thickness**
(a) Smooth round bar	R0	N/A	6.350	N/A
(b) Small radius notched bar	R1	3.175	6.350	N/A
(c) Large radius notched bar	R2	9.525	6.350	N/A
(d) Plane strain	PE	N/A	N/A	3.048

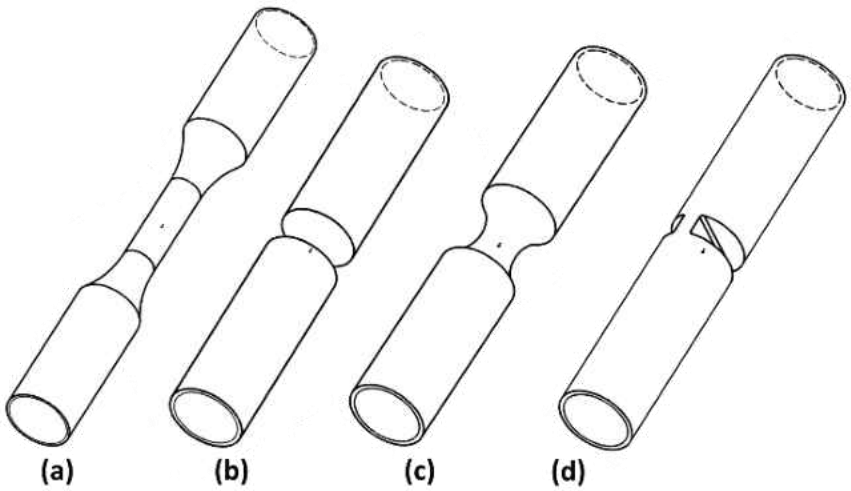

Figure 26: A 3D sketch of (a) smooth round bar, (b) small radius notch bar, (c) large radius notch bar, and (d) plane strain flat bar

Figure 27: Real specimens before testing denoted as R0, PE, R2, and R1 from left to right.

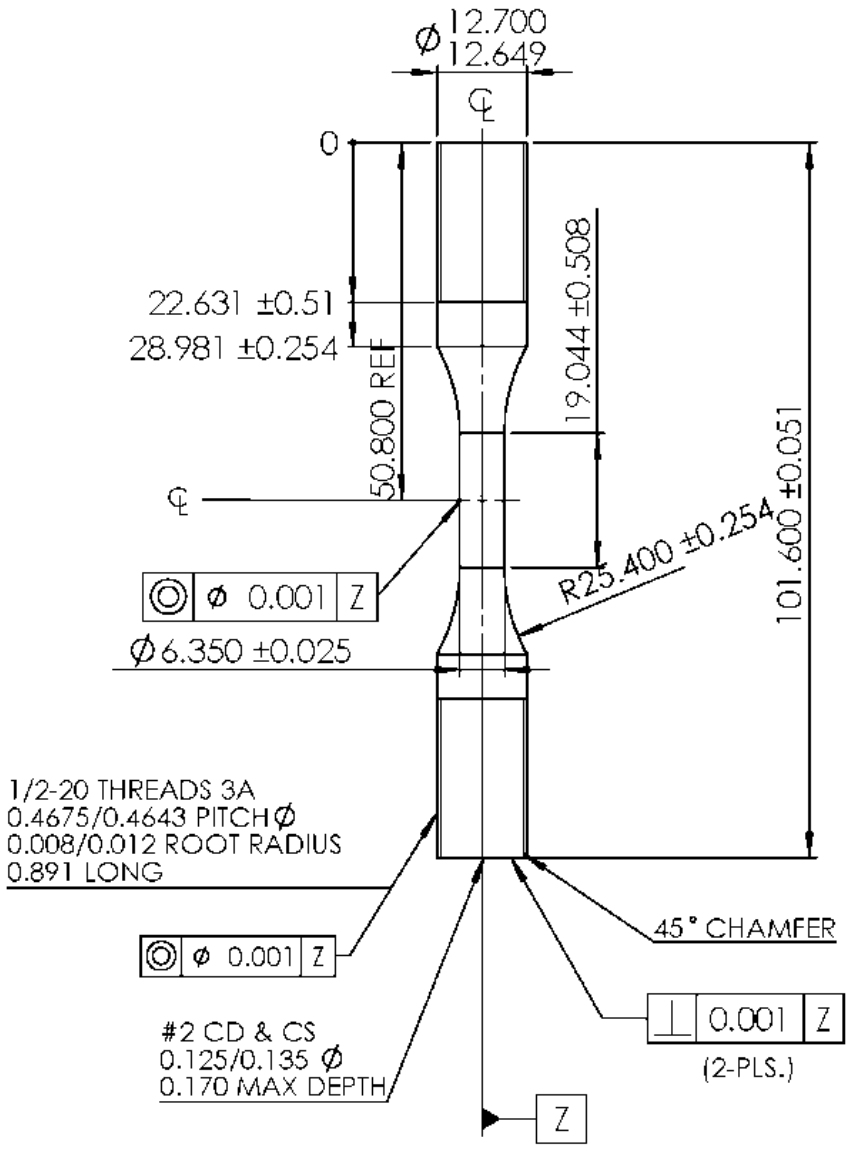

Figure 28: Geometry and dimensions in mm of the smooth round bar, R0.

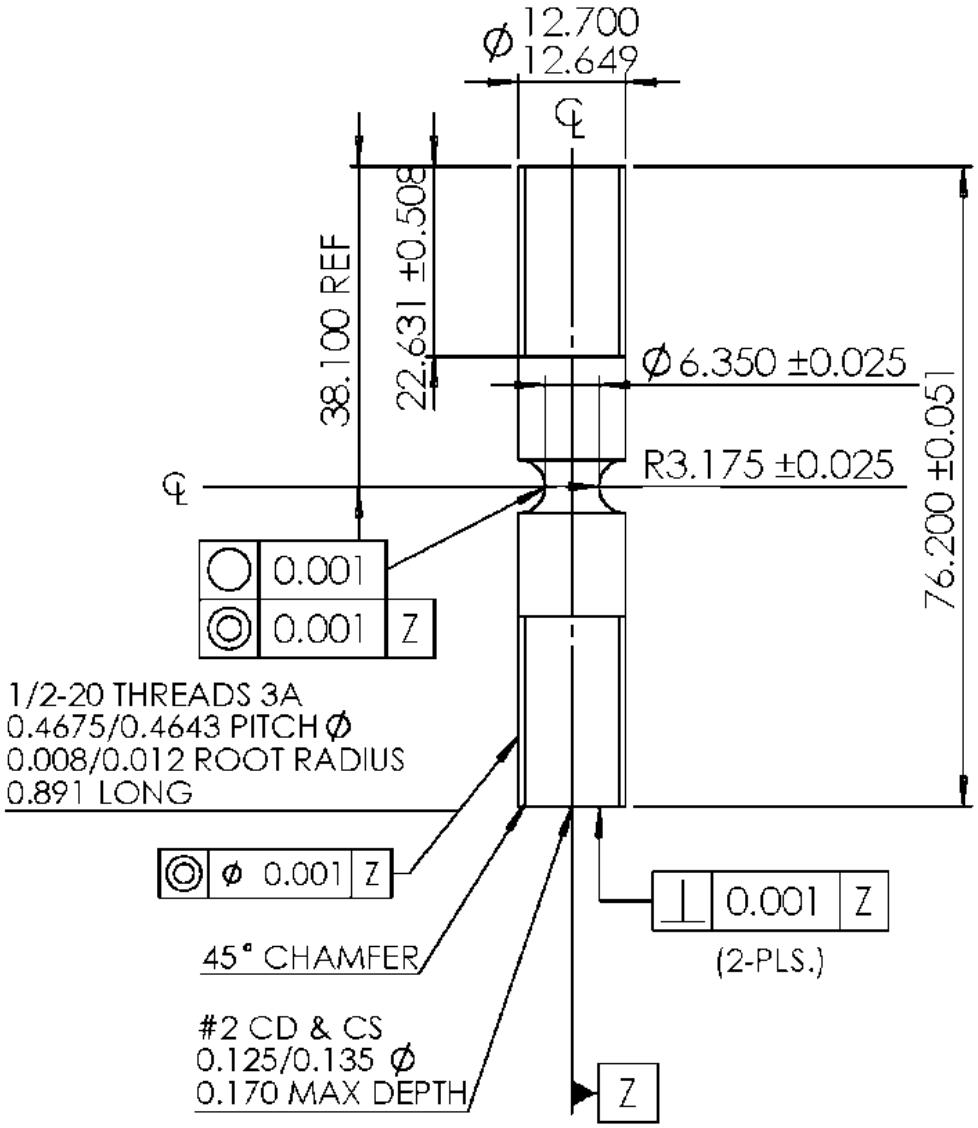

Figure 29: Geometry and dimensions in mm of the small notched bar, R1.

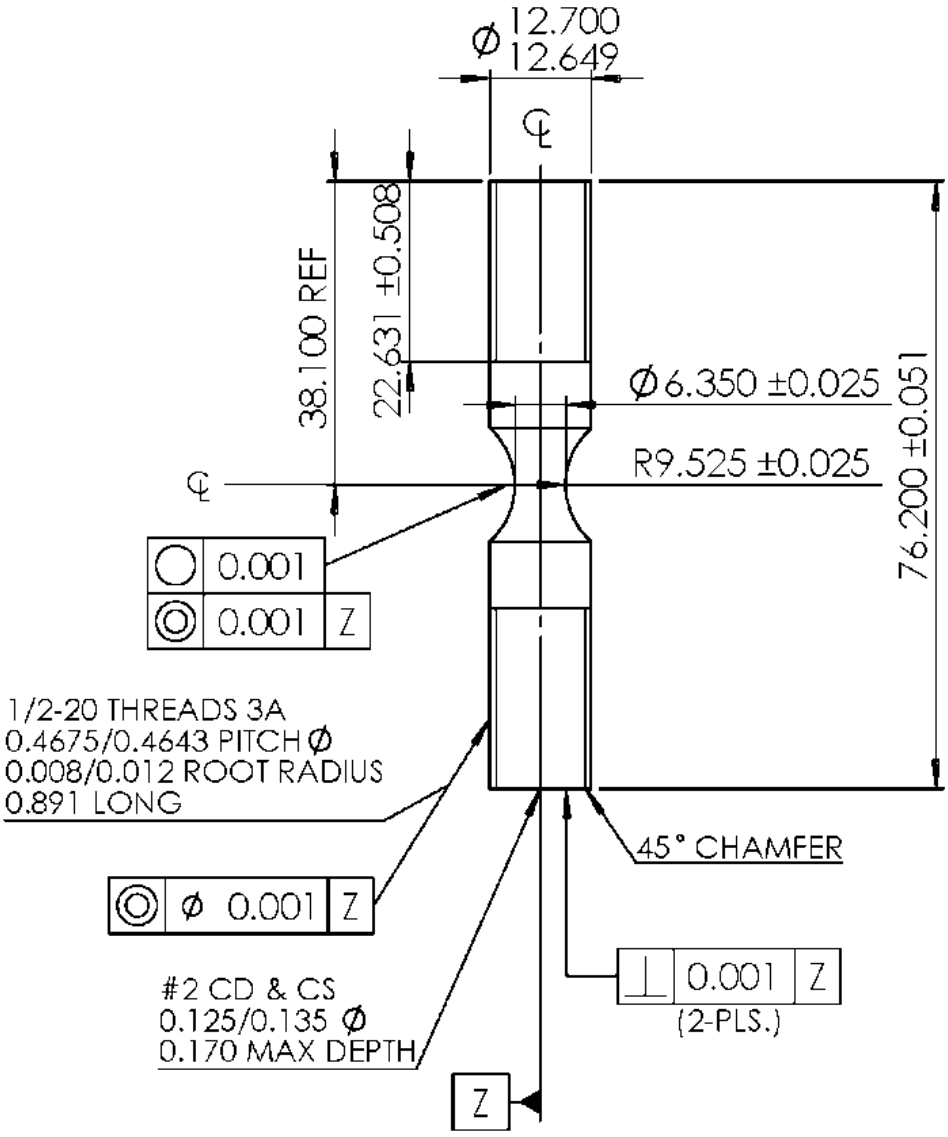

Figure 30: Geometry and dimensions in mm of the large notched bar, R2.

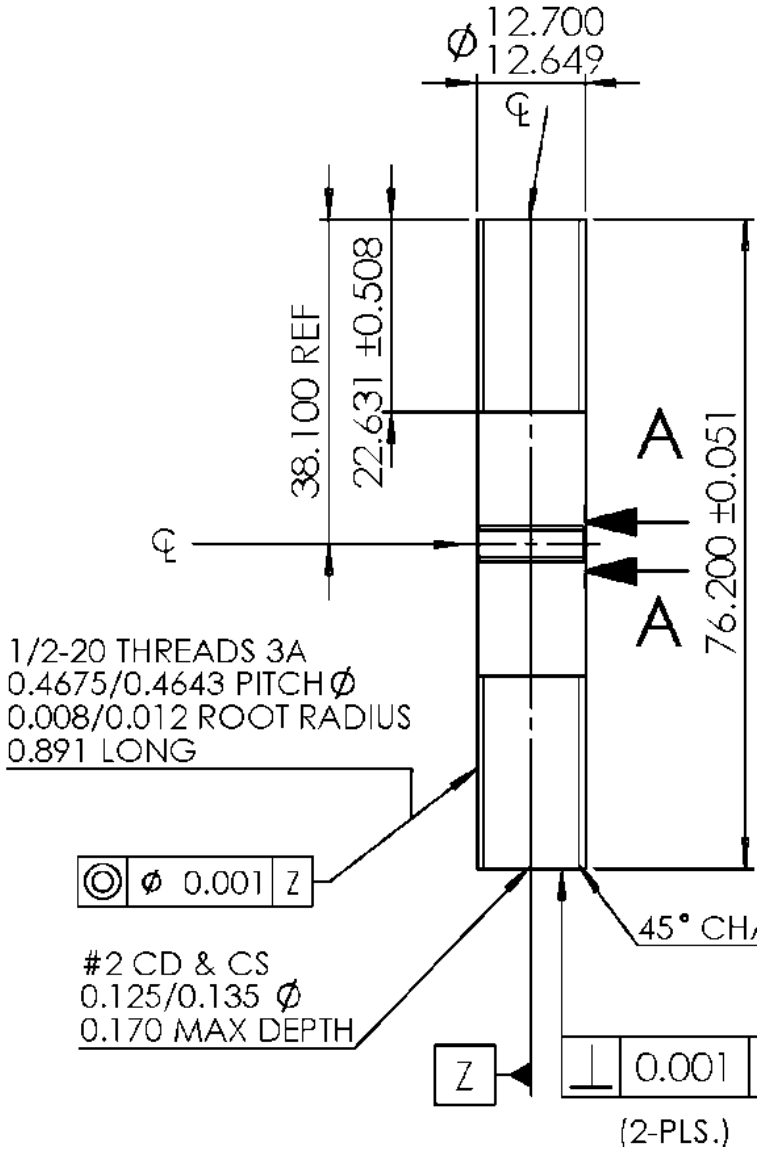

Figure 31: Geometry and dimensions in mm of the plane strain bar, PE.

4.6 Theoretical analysis of stress states

Hypothetically, each specimen with different geometries and stress state is expected to experience different values of stress triaxiality (η), Lode angle parameter ($\bar{\theta}$), and equivalent fracture strain ($\bar{\varepsilon}_f$). In this section, analytical solutions will be presented for these four types of specimens.

4.6.1 Smooth Round Bar

This type of specimen (denoted as "R0") is the most common type used in tensile tests by many studies. Tensile tests on smooth round bars (axial symmetry) helps to get the material properties and other constants related to plasticity and fracture models. The critical location is the site where necking occurs. Necking was clearly observed before fracture initiation for this material (see Figure 33 later). Fracture strain in this test can be estimated by area reduction at the necking area:

$$\bar{\varepsilon}_f = 2\ln\left(\frac{a_o}{a}\right) \quad (102)$$

A sketch of the necking area is shown in Figure 32. The classical Bridgman solution gives the stress components inside the necking area:

$$\sigma_{zz} = \bar{\sigma}\left[1 + \ln\left(\frac{a^2+2aR-r^2}{2aR}\right)\right] \quad (103)$$

$$\sigma_{xx} = \sigma_{yy} = \bar{\sigma}\ln\left(\frac{a^2+2aR-r^2}{2ax}\right) \quad (104)$$

By definition, the stress triaxiality inside the necking can be calculated using the following equation. [42, 43, 71]

$$\eta = \frac{\sigma_m}{\bar{\sigma}} = \frac{1}{3} + \ln\left(\frac{a^2+2aR-r^2}{2aR}\right) \quad (105)$$

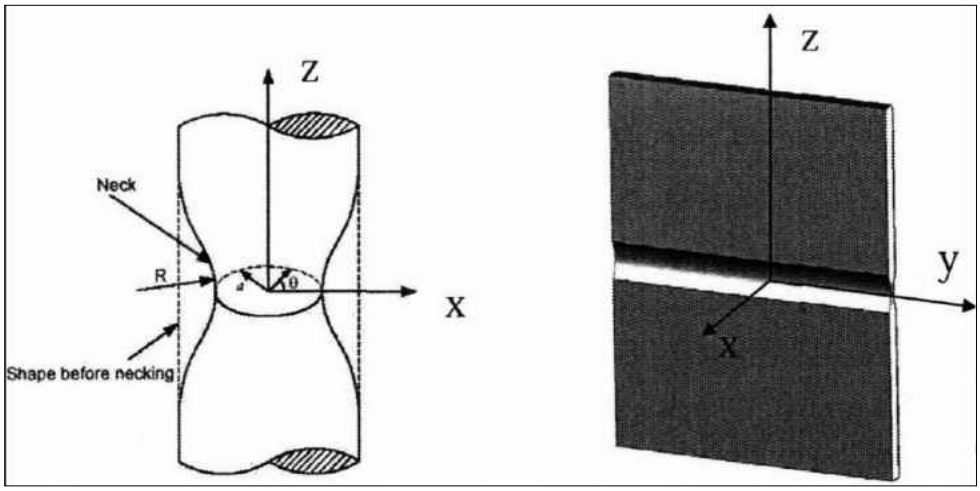

Figure 32: Stress distribution inside a neck of round bars, left and plane strain specimen, right. [43]

Here, $\sigma_{zz}, \sigma_{xx}, \sigma_{yy}, \sigma_m$ and $\bar{\sigma}$ are the axial, radial, hoop, mean and equivalent stresses, respectively. Other geometrical parameters (a, a_o, R) are demonstrated in Figure 32. The symbol r denotes the radial coordinate from the center of necking/notched area.

4.6.2 Notched Round Bars

Another two types of tensile tests are the notched round bar specimens (denoted as "R1" and "R2"). The term "notch" is defined as a localized discontinuity in a smoothly contoured geometry [170]. Similarly, the equations used to estimate local stress components, equivalent fracture strain (by area reduction) and stress triaxiality inside the necking are the same as the smooth round bar specimen and listed in section 4.6.1. We postulate these notched specimens to fail with lower strain fracture due to the higher stress triaxiality than that of smooth round bars. Two different external radii of the notch

are designed to examine the effect of stress triaxiality on ductile fracture strain. Detailed information regarding the notched bar geometries can be found in Figure 29 and Figure 30. The estimated initial stress triaxiality of these two specimens are $\eta = 0.7413$ for "R1" and $\eta = 0.5105$ for "R2". Note that the stress triaxiality will change as the neck area further develops. The average stress triaxiality will be calculated based on finite element simulations, which will be presented in section 4.6.

4.6.3 Plane Strain Specimen

This type of specimen is designed for a plane strain loading condition (denoted as "PE"). Compared to the other three specimens, this specimen has a different value of the Lode angle parameter ($\bar{\theta}$) but a similar range of stress triaxiality (η). This feature helps to investigate the effect of the Lode parameter on material plasticity and fracture [4]. A sketch of the necked area at plane strain condition is shown in Figure 32. When a necking is developed in the specimen, the equations to estimate the local stress distribution, equivalent fracture strain, and stress triaxiality are listed below, which are taken from analytical solutions provided in Ref. [171].

$$\bar{\varepsilon}_f = \frac{2}{\sqrt{3}} \ln\left(\frac{t_o}{t}\right) \quad (106)$$

$$\sigma_{xx} = \frac{2}{\sqrt{3}} \bar{\sigma} \ln\left(\frac{a^2+2aR-x^2}{2aR}\right) \quad (107)$$

$$\sigma_{yy} = \frac{2}{\sqrt{3}} \bar{\sigma} \left[\frac{1}{2} + \ln\left(\frac{a^2+2aR-x^2}{2aR}\right)\right] \quad (108)$$

$$\sigma_{zz} = \frac{2}{\sqrt{3}} \bar{\sigma} \left[1 + \ln\left(\frac{a^2+2aR-x^2}{2aR}\right)\right] \quad (109)$$

$$\eta = \frac{\sigma_m}{\bar{\sigma}} = \frac{\sqrt{3}}{3}\left[1 + 2\ln\left(1 + \frac{a}{2R}\right)\right] \quad (110)$$

4.7 Lab Experiment

The four types of specimens with different shapes were fabricated from the same piece of rod of Inconel 718 alloy. They were tested at room temperature and quasi-static loading conditions. Monotonic tensile tests were carried out on an MTS servohydraulic testing machine with a 100 kN (22kip) load cell capacity at a loading rate of 0.003 mm/sec. All tests were conducted until total fracture of specimens. The load-displacement curves were simultaneously recorded by testing machine and an optical measurement system. The full fields of surface strain were captured using a 2-D Digital Imaging Correlation (DIC) software provided by Correlated Solution Inc. (Vic2D 2009). The DIC measurement requires the samples to be spray painted in white then speckle patterned in black dots to get a perfect contrast for image correlation. This spackle pattern can be seen in Figure 33

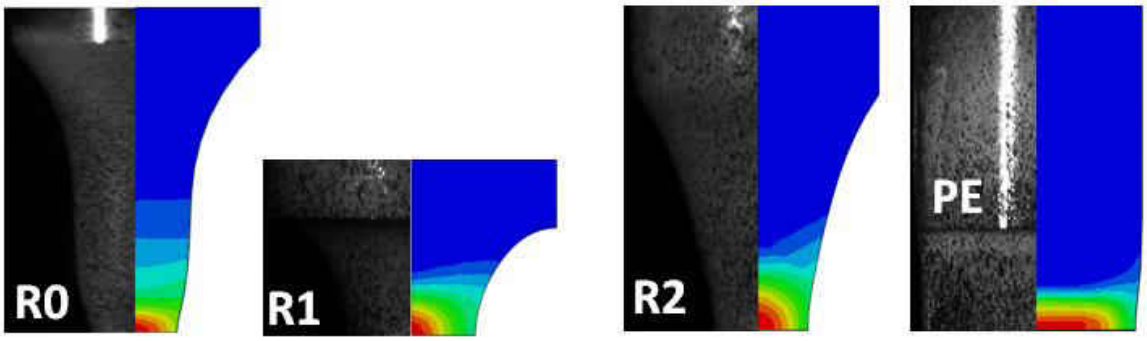

Figure 33: Deformed shapes prior to fracture of all specimens during the tests and the FE models showing a clear necking under all stress states. The contour plot shows the location of the high accumulation damage within the root of the necking area.

The measured force-displacement curves are shown in Figure 1 Figure 34. The reference gauge length (L_o) for these curves, corresponding axial displacement to fracture, gauge elongation, and area/thickness reduction at fracture site are summarized in Table 8. The experimental fracture strain can be estimated by area/thickness reduction at fracture site using the Equations in sections 4.6.1 and 4.6.3. The corresponding results are also listed in Table 8.

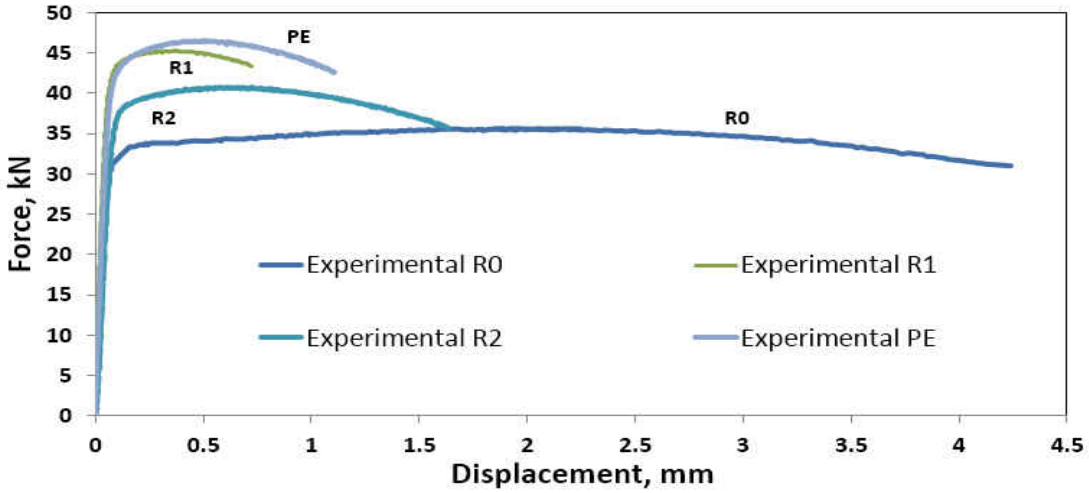

Figure 34: Experimental measured force-displacement responses along with the fracture occurrence with the gauge length of each test listed in Table 7.

Table 8: Experimental measurement of fracture for tensile tests of IN718.

Specimen	Gauge length	Displacement	Gauge Elongation	Gauge Area reduction	Fracture strain
R0	15.27 mm	4.23 mm	27.7%	50.6%	0.68
R1	9.16 mm	0.72 mm	7.9%	58.3%	0.39
R2	15.98 mm	1.63 mm	10.2%	55.3%	0.44
PE	4.19 mm	1.12 mm	26.7%	66.2% *	0.40

* Thickness reduction

4.8 Constitutive Models and Calibrations

4.8.1 Plasticity Model and Ductile Failure Criterion

A plasticity model that incorporates effects of strain hardening, hydrostatic pressure, and the Lode dependence was proposed by Bai and Wierzbicki [4]. This model is used for IN718 in the present paper. The plastic potential is shown as follows:

$$f = \sqrt{\frac{3}{2}\,[\mathrm{S}] : [\mathrm{S}]} - \sigma\left(\bar{\varepsilon}_{\mathrm{pl}}, \eta, \theta\right) = 0 \qquad (111)$$

The formulation to evince the plastic behavior in terms of plastic strain, hydrostatic pressure, and Lode dependency is described below:

$$\sigma\left(\varepsilon_{\mathrm{pl}}, \eta, \theta\right) = \sigma\left(\bar{\varepsilon}_{\mathrm{pl}}\right)\left[1 - c_{\eta}\left(\eta - \eta_{o}\right)\right]\left[c_{\theta}^{s} + \left(c_{\theta}^{ax} - c_{\theta}^{s}\right)\left(\frac{m+1}{m}\right)\left(\gamma - \frac{\gamma^{m+1}}{m+1}\right)\right] \qquad (112)$$

The first term of the plasticity model (above) is the Ludwik isotropic strain hardening function:

$$\sigma\left(\bar{\varepsilon}_{pl}\right) = \sigma_{y} + K\,\bar{\varepsilon}_{pl}^{\,n} \qquad (113)$$

where σ_y, K and n are the initial yield stress, strength index, and strain hardening exponent, respectively [104, 172].

The second term of the plasticity model is the effect of the hydrostatic pressure on yield where c_{η} is a material parameter which needs to be calibrated. The other parameter η_{o} is the reference value of stress triaxiality set from the calibration test to get the first hardening term. In our work, the parameter η_{o} is set to be 1/3 because the base hardening curve was obtained from uniaxial tension (specimen "R0"). It should be noted that the term of $\left[1 - c_{\eta}\left(\eta - \eta_{o}\right)\right]$ should be bounded within certain limits for the very high or very low stress triaxiality region. For example, $0.5 \leq \left[1 - c_{\eta}\left(\eta - \eta_{o}\right)\right] \leq 2.0$ was used in our simulations.

The third term in this model is the Lode dependence, where a correction term, $\left(\frac{m+1}{m}\right)$, is introduced to make it more user-friendly. This is slightly different from the original term in the paper [4]. The Lode angle term consists of four material

constants c_θ^s, c_θ^t, c_θ^c, and m that needs to be calibrated. The terms c_θ^s, c_θ^t, c_θ^c are relative and at least one of them equals one. This depends on the type of the calibration test when calibrating the strain hardening function. The parameter c_θ^t is set unity because the specimen "R0" is used.

$$c_\theta^{ax} = \begin{cases} c_\theta^t & \text{for } \bar{\theta} \geq 0 \\ c_\theta^c & \text{for } \bar{\theta} < 0 \end{cases} \quad (114)$$

Calibration of other material constants are stated and justified in the section 4.8.2 with details. The parameter γ defined in the following equation, is the strength difference between von Mises and Tresca in the deviatoric stress plane.

$$\gamma = 6.4641\,[\sec(\theta - \pi/6) - 1] \quad (115)$$

After modification and normalization, the range of γ is $0 \leq \gamma \leq 1$. In axial symmetry and plane strain conditions, the γ is 1.0 and 0.0, respectively.

The term c_θ^s in the Lode angle dependency part is not necessary a constant.

$$c_\theta^s\left(\bar{\varepsilon}_{pl}, \bar{\theta}\right) = \frac{\sqrt{3}}{2} + \left(B_1\, e^{-B_2 \bar{\varepsilon}_{pl}}\right) f\left(\bar{\theta}\right) \quad (116)$$

It is found that this parameter (c_θ^s) evolves for In718 as plastic deformation continues, which is the second extension from the original plasticity model. A new formulation is proposed, where c_θ^s is a function of the equivalent plastic strain ($\bar{\varepsilon}_{pl}$) and the Lode angle parameter ($\bar{\theta}$). FE simulations of individual cases revealed that the value of c_θ^s does not affect at $\bar{\theta}$ = 1 for "R0", "R1", and "R2" specimens (axisymmetric condition). On the other hand, c_θ^s for the PE specimen (plane strain condition) varies as a

function of the equivalent plastic strain (controlled by parameter B_2) and the Lode angle parameter.

$$f(\bar{\theta}) = \left(1 - \left|\bar{\theta}\right|^{B_3}\right)^{B_4} \quad (117)$$

The construction of B_3 and B_4 in function $f(\bar{\theta})$ was built in a way to ensure zero slopes at $\bar{\theta}$ = -1, 0, and 1 as shown in Figure 35. This consideration is to make the yield locus smooth. An example plot of the function $f(\bar{\theta})$ is illustrated in Figure 35.

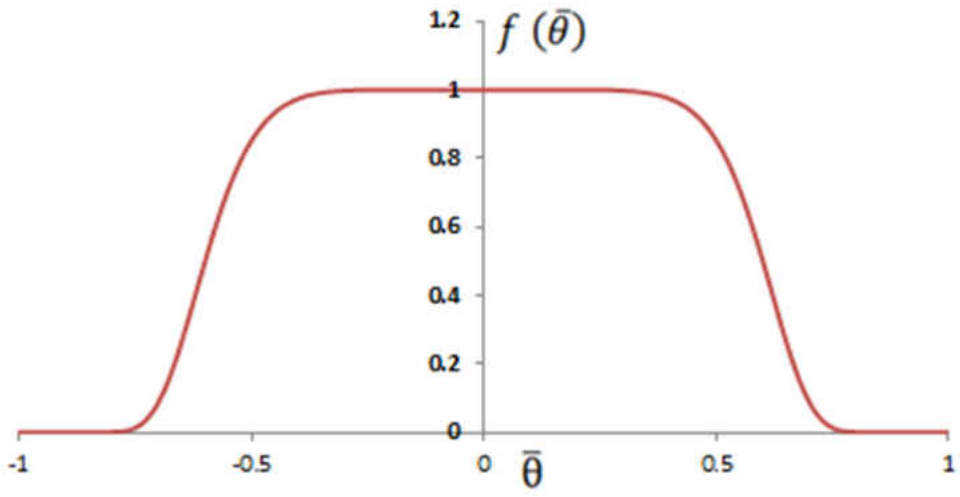

Figure 35: An example of function f ($\bar{\theta}$) used in the parameter (c_{θ}^{s}) controlling the Lode angle dependence on material plasticity

The proposed plastic flow potential with both pressure and Lode angle dependence is designed for material strength under different loading conditions. The plastic flow of metallic materials is usually believed to be incompressible [87], so a fully associated flow rule (AFR) cannot be directly applied. According to Ref. [4], a partially associated flow rule (or called deviatoric associated flow rule) is used, which neglects the

term of stress triaxiality while calculating derivative of plastic flow potential to get flow directions.

Regarding the ductile fracture modeling, the modified Mohr-Coulomb criteria (MMC) [25] is used to predict crack initiation and propagation under different stress states. The classical form of Mohr-Coulomb was transformed from the three principal stresses space to the mixed space of ($\bar{\varepsilon}_f, \eta, \bar{\theta}$) (equivalent strain to fracture, stress triaxiality, and Lode angle parameter, respectively) [25]. The coupling effect of stress triaxiality and Lode angle is captured by the MMC model. This phenomenological fracture criterion has shown great prediction capabilities to onset of fracture in various applications [49, 50, 57, 173-175]. The general representation of the MMC criterion in terms of $\varepsilon_f, \eta, \bar{\theta}$ is as below:

$$\varepsilon_f = \left\{ \begin{array}{c} \frac{A}{c_2}\left[1 - c_\eta\left(\eta - \eta_o\right)\right] \\ \times \left[c_\theta^s + \frac{\sqrt{3}}{2-\sqrt{3}}\left(c_\theta^{ax} - c_\theta^s\right)\left(\sec\left(\frac{\bar{\theta}\pi}{6}\right) - 1\right)\right] \\ \times \left[\sqrt{\frac{1+c_1^2}{3}}\cos\left(\frac{\bar{\theta}\pi}{6}\right) + c_1\left(\eta + \frac{1}{3}\sin\left(\frac{\bar{\theta}\pi}{6}\right)\right)\right] \end{array} \right\}^{-1/N} \quad (118)$$

Since the effects of c_η and c_1 are similar in stress triaxialtiy, one can omit the term of pressure dependence on yield surface due to its negligible effect [25]. The below form of fracture locus is employed for current investigation. The fracture locus of MMC model reads:

$$\bar{\varepsilon}_f(\eta,\bar{\theta}) = \left\{ \begin{array}{l} \frac{A}{c_2}\times\left[\tilde{c}_\theta^s + \frac{\sqrt{3}}{2-\sqrt{3}}(\tilde{c}_\theta^{ax} - \tilde{c}_\theta^s)\left(\sec\left(\frac{\bar{\theta}\,\pi}{6}\right) - 1\right)\right] \\ \times\left[\sqrt{\frac{1+c_1^2}{3}}\cos\left(\frac{\bar{\theta}\,\pi}{6}\right) + c_1\left(\eta + \frac{1}{3}\sin\left(\frac{\bar{\theta}\,\pi}{6}\right)\right)\right] \end{array} \right\}^{-1/N} \quad (119)$$

There are eight parameters, A, N, c_η , η_o, $\tilde{c}_\theta^s$, $\tilde{c}_\theta^{ax}$, c_1, and c_2, need to be calibrated. The parameters A and N are material strain hardening properties from the reference material strain hardening curve, and $\tilde{c}_\theta^{ax}$ is assumed to be one for simplicity, whereas $\tilde{c}_\theta^s$, c_1, and c_2 will be calibrated from the fracture tests.

In general, for the Von-Mises yielding function, the parameters become $c_\eta = 0$, $c_\theta^s = c_\theta^c = 1$, making the general equation to be:

$$\varepsilon_f = \left\{ \frac{A}{c_2}\left[\sqrt{\frac{1+c_1^2}{3}}\cos\left(\frac{\bar{\theta}\,\pi}{6}\right) + c_1\left(\eta + \frac{1}{3}\sin\left(\frac{\bar{\theta}\,\pi}{6}\right)\right)\right]\right\}^{-1/N} \quad (120)$$

While in the Tresca yield function, the parameters become $c_\eta = 0$, $c_\theta^s = \sqrt{3}/2$, $c_\theta^c = 1$, the general equation reduces to

$$\varepsilon_f = \left\{ \frac{A}{c_2}\left[\sqrt{\frac{1+c_1^2}{3}} + c_1\frac{\sqrt{3}}{2}\sec\left(\frac{\bar{\theta}\,\pi}{6}\right)\left(\eta + \frac{1}{3}\sin\left(\frac{\bar{\theta}\,\pi}{6}\right)\right)\right]\right\}^{-1/N} \quad (121)$$

In order to simulate the fracture propagation and get the correct crack modes (especially the slant fracture in plane strain conditions and the cup-cone failure mode in round bars), material or element softening after fracture initiation was found to be necessary [56, 60, 176]. A general form of the softening law is described by introducing a

softening coefficient β. The symbol $\tilde{\sigma}_{yield}$ is the softened flow stress, and $\bar{\sigma}_{yield}$ is the undamaged original flow stress:

$$\tilde{\sigma}_{yield} = \beta\, \bar{\sigma}_{yield} \quad (122)$$

$$\beta = \left(\frac{D_c - D}{D_c - 1}\right)^w \quad (123)$$

The coefficient β is assumed to be a nonlinear function of damage indicator D where D_c and w are material softening parameters that will be calibrated later. Note that the softening law is effective only after the fracture initiates ($D > 1$). The fracture initiates when $D = 1$, which corresponds to $\beta = 1$. Accordingly, a complete split of the material points happens when $D = D_c$, after which the material element shows no resistance [56]. In other words, the parameter D_c is the value of damage indicator when an integration point of an element in the ABAQUS user defined material subroutines will be deleted and shows zero resistance. It is assumed that the evolution of damage indicator D follows a linear damage rule, as shown:

$$D = D\left(\bar{\varepsilon}_{pl}\right) = \int_0^{\bar{\varepsilon}_{pl}} \frac{d\bar{\varepsilon}_{pl}}{\bar{\varepsilon}_f(\eta, \bar{\theta})} \quad (124)$$

4.8.2 Model Calibration

The proposed plasticity and fracture model was implemented to Abaqus/Explicit as a material subroutine (VUMAT). This section will present the detail calibration processes. The Ludwick isotropic strain hardening parameters in $\sigma\left(\varepsilon_{pl}\right) = \sigma_y + K\,\varepsilon_{pl}{}^n$ were calibrated by utilizing the true stress-true strain curve of the smooth round bar specimen ("R0"). The load-displacement curve of the smooth round bar was recorded

during the test. This curve was converted to the engineering stress-engineering strain curve (σ_E, ε_E). Then, the true stress-true strain curve (σ_t , ε_t) was obtained through the transformation equations.

$$\sigma_t = \sigma_E(1 + \varepsilon_E) \quad (125)$$

$$\varepsilon_t = \ln(1 + \varepsilon_E) \quad (126)$$

Note that these two equations are not valid after the necking initiation. The curve data before necking were fitted using the Ludwik isotropic strain hardening function.

Three parameters of the Ludwick model ($\sigma_y, K,$ and n) were Table 9. This calibrated strain hardening curve was then applied to all specimens for numerical simulations as a baseline.

The stress-strain curve after necking was firstly estimated by extrapolation of the Ludwick equation, and then it was followed by a trail-and-error method (adjusting parameters from the softening part) until the numerical load-displacement curve showed perfect agreement with the test one (specimen "R0").

Special consideration was taken in calibrating the pressure effect in the plasticity model in order to simulate the load-displacement responses of two notched-specimens ("R1" and "R2"). Compared to the smooth round bar ("R0"), these two specimens have the same Lode angle parameter ($\bar{\theta} = 1$) but higher stress triaxiality, so they can be used to investigate the pressure dependence on plasticity. It is found that the parameter c_η in the hydrostatic pressure term the plasticity model needs to be increased to have a satisfactory curve fit for specimens "R1" and "R2".

To characterize the Lode angle dependence on plasticity, efforts were put to the plane strain specimen ("PE"). Since the pressure dependency has been calibrated by notched round specimens, the plane strain specimen has same range of stress triaxiality but different Lode angle parameter ($\bar{\theta} = 0$), so it can be used to study the Lode angle effect. The corresponding parameter are c_θ^s and c_θ^c. Since there are no compression or equi-biaxial test data available, it is assumed that yield locus of IN718 is symmetric between tension and compression, so $c_\theta^c = 1$. In simulating the test of plane strain specimen, it is found that the parameter c_θ^s cannot be constant as plastic deformation continues. The interesting phenomenon will be discussed again in section 4.9.1 By adjusting the parameters in function $c_\theta^s\left(\bar{\varepsilon}_{pl}, \bar{\theta}\right)$ a nice correlation of force-displacement curves between test and simulation is achieved for specimen "PE". This concludes the calibration process for plasticity model. All the calibrated parameters for the proposed plasticity model are listed in Table 10.

The modified Mohr-coulomb model (MMC) was used to predict both fracture initiation and propagation. The power hardening parameters (A and N) for the MMC criterion takes from $\bar{\sigma} = A\,\bar{\varepsilon}^N = 1480\,\bar{\varepsilon}^{0.0813}$. Finite element simulations were conducted until fracture initiation without involving fracture option to get the history of stress triaxiality $\eta\left(\bar{\varepsilon}_{pl}\right)$, and history of Lode angle parameter $\bar{\theta}(\bar{\varepsilon}_{\mathrm{pl}})$. Subsequently, three fracture parameters ($\tilde{c}_\theta^s$, c_1, and c_2) were calibrated by evaluating the damage evolution $D(\bar{\varepsilon}_{pl})$ using the integral definition explained in page 86 . The hypothesis states that a material element fails when the limit of ductility is reached, $\bar{\varepsilon}_{pl} = \bar{\varepsilon}_f$, so

that $D(\bar{\varepsilon}_f) = 1$. The stress triaxiality, Lode angle, and equivalent plastic strain at fracture initiation sites are output from the numerical simulations at each time step. A Matlab code was created to run the damage evolution integration to get the best estimation for the three constants ($\tilde{c}_\theta^s$, c_1 and c_2) such that the calculated damage indicates (D) for all four cases are as close to unity as possible. The results of fracture model parameters are summarized in Table 11, which gives satisfactory simulation results.

Finally, in order to depict the experimental results of material post failure behavior (which affects the fracture propagation and final fracture modes), the softening of yield stress is introduced in the current investigation. There are two additional parameters need to be identified: D_c and w. It is found that the power parameter w must be large enough to get the best simulation of the experimental stress response when force-displacement curves instantly drop after fracture initiation. Many iterations of finite element simulation were conducted for each specimen with different values of the power coefficient *w* in order to simulate the actual experimental fracture patterns perfectly for each specimen. The calibrated softening parameters are listed in Table 11.

Table 9: List of material elastic-plastic properties used in the FEA.

young's modulus, E	**Poisson ratio, *v***	σ_y	**K**	**n**
200 GPa	0.284	945.1	835.4	0.425

Table 10: List of material parameters of yield locus used in the plasticity model.

c_η	η_o	c_θ^c	c_θ^{ax}	m	B_1	B_2	B_3	B_4
0.11	0.333	1	1	0.75	0.23	5.50	40.80	8.00

Table 11: List of material fracture parameters used for the MMC criterion and the material softening equation.

c_1	c_2	$\tilde{c}_\theta^s$	c_θ^{ax}	A	N	D_c	w
0.05896	764.588 MPa	0.86276	1	1480	0.0813	1.2	6

4.9 Experimental and Numerical Simulations Results

In this chapter, results from tests and finite element simulations using Abaqus/Explicit with VUMAT are presented together for a direction comparison. The detail constitutive/ductile fracture models and their calibration procedures have been described in sections 4.8.1 and 4.8.2.

4.9.1 Comparison of Plasticity and Fracture Results

The first three round specimens ("R0", "R1", and "R2") were developed in ABAQUS using quarter models due to symmetric conditions, and 4-node axisymmetric elements (CAX4R) were used. For the plane strain specimen, pure plane strain condition only exists at the central range of the specimen due to the limitation of specimen size and machine testing capacity for this tough material. The two edge regions are more close to plane stress and uni-axial tension. Therefore, an FE model was developed using 8-node

solid elements (C3D8R). Since the shape of the specimen is symmetric, only a quarter model of the specimen was created. Meshes of these four types of specimens are shown in Figure 36.

Comparisons of specimen deformation right before fracture initiations and configurations from FE simulations are shown in Figure 33. For round specimens, one can see that the developments of the circumferential neck are clearly shown in both tests and the simulations. This is observed for the smooth round bar ("R0") and the two notched round specimens ("R1" & "R2") as presented in Figure 33. The quantitative measurements of the final radius at neck for each specimen are listed in Table 12. The diffuse necking for the plane strain specimen ("PE") was also noticed in the test, and configuration of numerical simulation is illustrated in Figure 33.

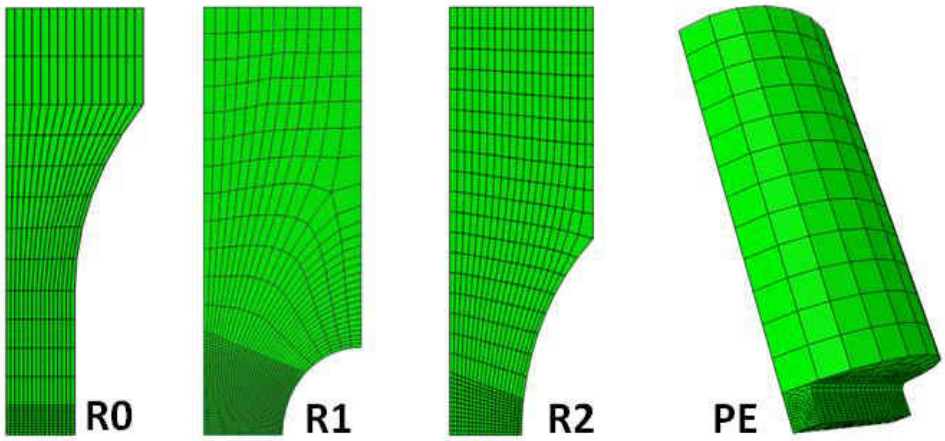

Figure 36: Meshes and different element types in Abaqus to conduct finite element simulations

Table 12: A summary of the characterized dimensions of the fracture radius/thickness.

Specimen	Analytical		Numerical Simulation	
	Neck diameter	Thickness	Neck diameter	Thickness
R0	4.54 mm	N/A	4.83 mm	N/A
R1	5.26 mm	N/A	5.59 mm	N/A
R2	5.13 mm	N/A	5.26 mm	N/A
PE	N/A	2.02 mm	N/A mm	2.00 mm

Comparisons of the predicted force-displacement curves are shown in Figure 37 for all four types of specimens. Solid curves represent test data, and dash curves are simulation results. One can see that an excellent correlation is achieved for the calibrated plasticity model. The comparative results of plastic deformation (Figure 33) and material strength (Figure 37) validate the proposed constitutive model.

The calibration procedure of proposed ductile fracture model is described in Section 4.8.2. To construct the fracture locus, one key step is to obtain the accurate histories of two stress state parameters, which vary as plastic deformation continues even under monotonic loading conditions. Obtaining the average stress triaxiality and the average Lode angle parameter will help in constructing a fitted 3D fracture locus and properly calibrating the failure criterion. These average values (η_{avg}, $\bar{\theta}_{avg}$) are defined in:

$$\eta_{avg} = \frac{1}{\bar{\varepsilon}_f} \int_0^{\bar{\varepsilon}_f} \eta\left(\bar{\varepsilon}_{pl}\right) d\bar{\varepsilon}_{pl} \quad (127)$$

$$\bar{\theta}_{avg} = \frac{1}{\bar{\varepsilon}_f} \int_0^{\bar{\varepsilon}_f} \bar{\theta}(\bar{\varepsilon}_{pl})\, d\bar{\varepsilon}_{pl} \quad (128)$$

The numerical simulations provide real histories of $\eta\ (\bar{\varepsilon}_{pl})$ and $\bar{\theta}\ (\bar{\varepsilon}_{pl})$, which are illustrated in Figure 38 and Figure 39. The average values of stress triaxiality are also plot in the same figure. The equivalent strains to fracture $\bar{\varepsilon}_f$ were obtained from FE simulations corresponding to the measured displacements to fracture (d_f). Those fracture strains are marked in Figure 38. The changes in the stress triaxiality with respect to the equivalent plastic strain were evident. The notched round specimens ("R1", "R2") and the plane strain specimen ("PE") show a dramatic increase of the stress triaxiality in the initial stages of plastic deformation, and then a gradual change follows. On the contrary, the smooth round bar ("R0") shows a steady increase in the stress triaxiality as the equivalent plastic strain increases with no sign of decrease in value.

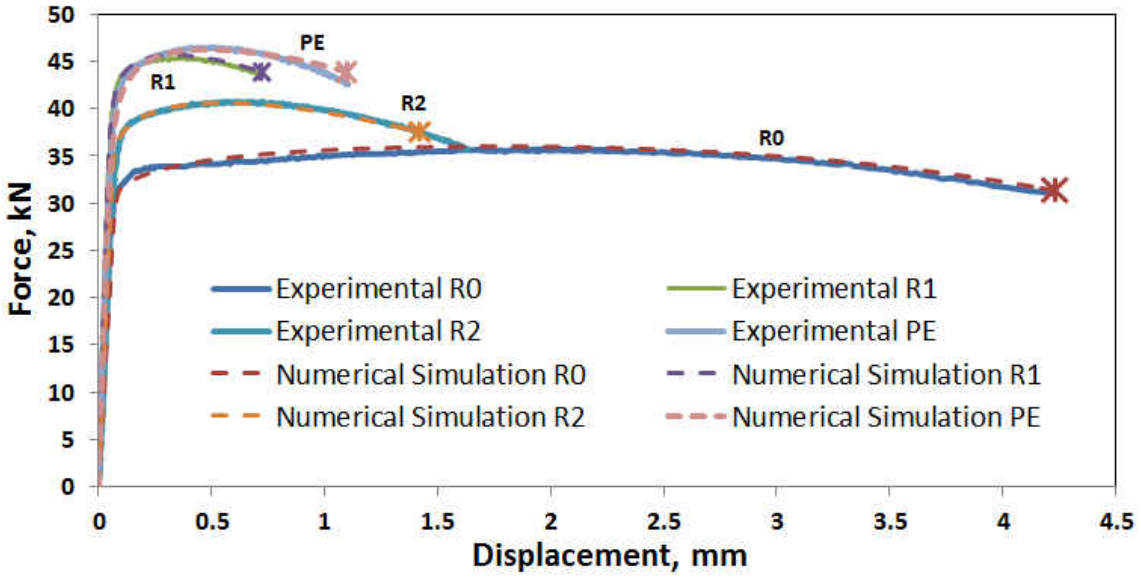

Figure 37: Measured force-displacement responses with the gauge length of each test listed in Table 8. A comparison of the numerical and experimental results along with the fracture occurrence for all specimens shows good correlation.

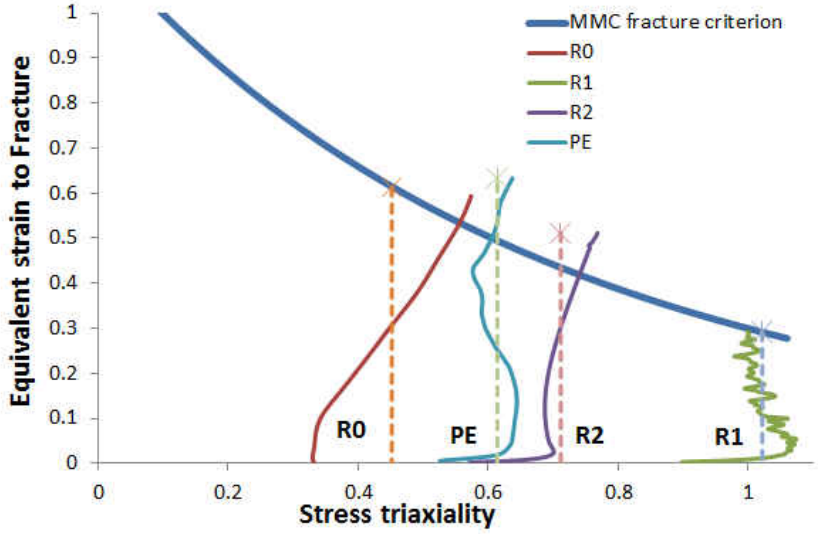

Figure 38: Numerical stress triaxiality values vs. equivalent strain in the necking center of each specimen (fixing $\bar{\theta}$=1 for MMC model). Fracture locus of Inconel 718 alloy from numerical simulations showing both the average stress triaxiality (dash lines) and the evolution of stress triaxiality (solid curves) in the loading process.

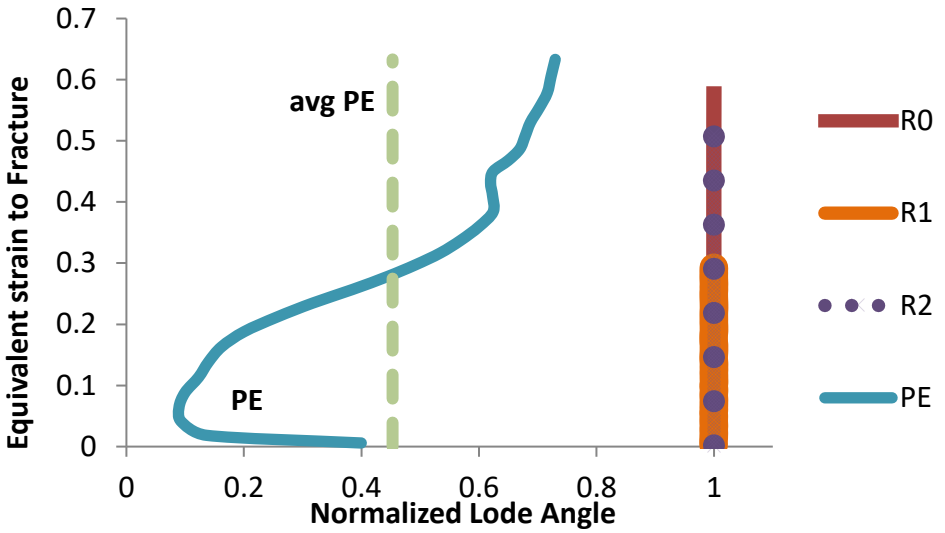

Figure 39: Numerical results of Lode angle parameter vs. equivalent strain in the necking center of each specimen.

Theoretical solutions of stress triaxiality and the fracture strain estimation based on area reduction are compared to the numerical results of η_{avg} and $\bar{\varepsilon}_f$, see Table 13. The comparison shows reasonable good agreement between analytical and numerical solutions for the values at the center of the neck, where cracks initiate. The existence of some differences is mainly due to two reasons. One is that the analytical solution of stress triaxiality is just the initial value rather than the average value. The second one is that the analytical solutions of fracture strain are based on the average value of the whole necking cross-section, while the numerical fracture strain is the local strain at the center. Another difference is the Lode angle parameter for the plane strain specimen. Theoretical solution of plane strain condition gives $\bar{\theta} = 0$, but the average value is 0.4530. The real history this parameter is shown in Figure 39. The main reason for this difference is due to the design of plane strain specimen. The "PE" specimen is not wide enough (subjected to

material size and testing machine limits) to achieve pure plane strain condition. However, the numerical simulation helps to construct its real loading condition.

Table 13: A summary of stress triaxiality, Lode angle, and equivalent plastic strain to failure from both experimental data and numerical simulations

Specimen	**Theoretical solution**			**Numerical simulations**		
	η	$\bar{\theta}$	$\bar{\varepsilon}_f$	η_{avg}	$\bar{\theta}_{avg}$	$\bar{\varepsilon}_f$
R0	0.3333	1	0.6804	0.4520	1	0.6129
R1	0.7413	1	0.3861	1.0213	1	0.2924
R2	0.5105	1	0.4424	0.7165	1	0.5123
PE	0.5774	0	0.4004	0.6141	0.4530	0.6331

The results in Table 13 is used to construct the 2D fracture locus in the space of stress triaxiality versus the equivalent strain to fracture as illustrated in Figure 40. It is seen that the equivalent plastic strain to fracture ($\bar{\varepsilon}_f$) of Inconel 718 generally decreases as the stress triaxiality increases except for the plane strain conditions. This is due to the effect of Lode angle parameter on ductile fracture.

The numerical simulation results are used to calibrate the MMC 3D fracture locus according to the procedures described in Section 4.8.2. The calibrated parameters of MMC fracture model are listed in Table 11. By invoking the fracture option in Abaqus simulation, the displacements corresponding to fracture initiation can be predicted in finite element simulations, which are marked in Figure 37. One can see that the plastic behavior and fracture initiation in the numerical simulation agree very well with test results of all four specimens. The fully calibrated 3D fracture locus of IN718 is shown in Figure 41. The differences between model prediction and test results for each specimen

are also marked. It is found that the fracture surface based on the MMC criterion in this study agrees with the that established by JCXd fracture model in Ref. [68]. Two test data under shear and plane strain tension ($\bar{\theta} = 0$) from Ref. [9] for the same grade of material are also plotted in the same figure for comparison. The comparison results show satisfactory agreement as in Figure 41. It is concluded that the MMC fracture model can be used to describe the ductile fracture of IN718 with good accuracy.

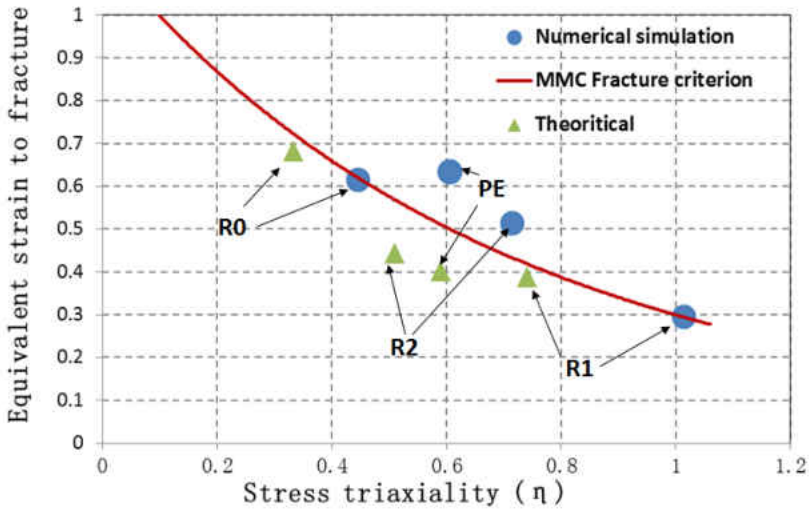

Figure 40: Calibrated MMC 2D ductile fracture locus (*setting* $\bar{\theta} = 1$) shows the relationship of average stress triaxiality and equivalent strain to fracture for Inconel 718. The theoretical solutions of stress triaxiality and fracture strains are marked as solid triangles for comparison.

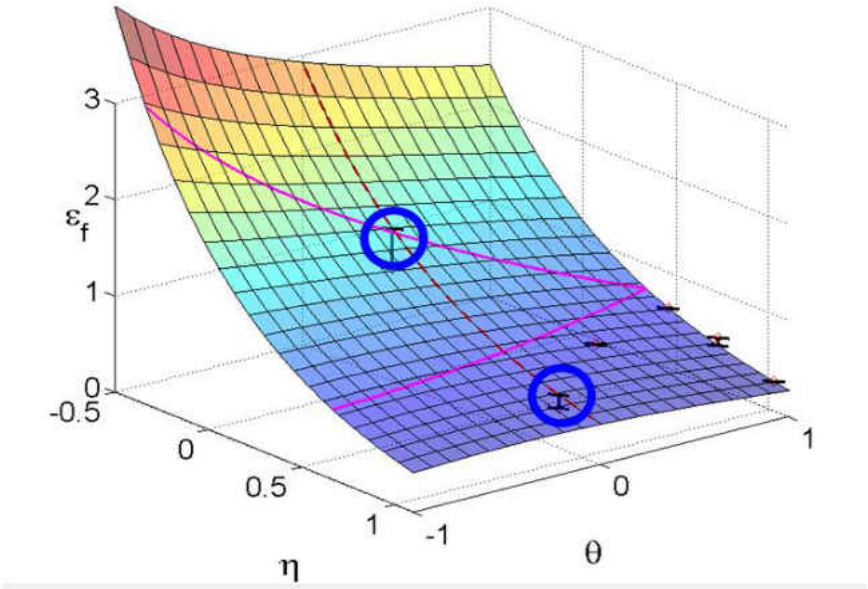

Figure 41: Calibrated MMC 3D fracture locus corresponding to monotonic tensile test of Inconel 718. Experimental data lie on the fracture surface. Two data points shown as blue circles on the plane strain line ($\bar{\theta}$=0) are taken from Ref. [9] for comparison.

4.9.2 Simulation of Ductile Fracture Propagation and Crack Modes

Conventional finite element simulations typically predict a flat fracture surface that is perpendicular to the load direction. In contrast, the experimental results show that crack propagated along a developed shear band with the least energy dissipation [98, 176]. During the tests, three round bars specimens ("R0", "R1", and "R2") exhibit vivid necking in the gauge section (the minimal cross section diameter) with a cup-cone fracture mode. Initial micro cracks occurred in the gauge center followed by crack propagation outward. Then, a shear lip was formed at the circumferential edge of the outer radius (which is close to plane strain condition). This created a cup-cone fracture mode. On the other hand, the plane strain specimen ("PE") shows a slant fracture mode,

which was caused by a shear band generated in the gauge section. The sudden fracture initiation and propagation for all specimens causes a quick load drop in the force-displacement curves. In reality, many local phenomena happened within this short increment of displacement.

It is found that the material/element post-failure softening behavior controls the prediction of fracture propagation. The calibration procedure of the softening function is described in Section 4.8.2. Through iterative finite element simulations, a suitable parameter, $w = 6$, is identified. The predicted fracture modes well correlate with test results for all specimens as illustrated in Figure 42, Figure 43, Figure 44, and Figure 45. The simulations of round specimen were presented using the sweep feature in ABAQUS to render a 2D axisymmetric model into a full 3D geometry. It is important to mention that fracture simulations are sensitive to the element mesh size. The finer mesh size will give clearer fracture surface configurations. The used mesh size was 0.05mm for all these simulations. It is concluded that the MMC fracture criterion is capable of depicting both the fracture initiation and the fracture propagation modes for all four types of specimens.

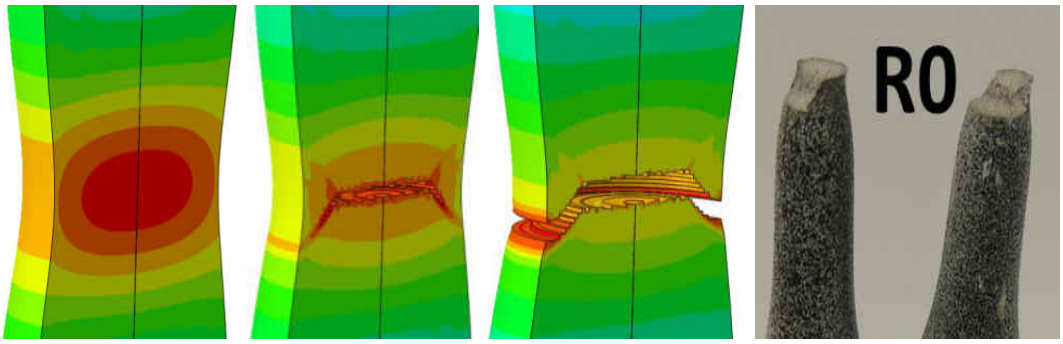

Figure 42: Deformation and fracture steps in the numerical simulation show a cup-cone fracture pattern for the smooth round bar ("R0"). The right figure shows the experimental result. The contour plot is the equivalent plastic strain in ABAQUS.

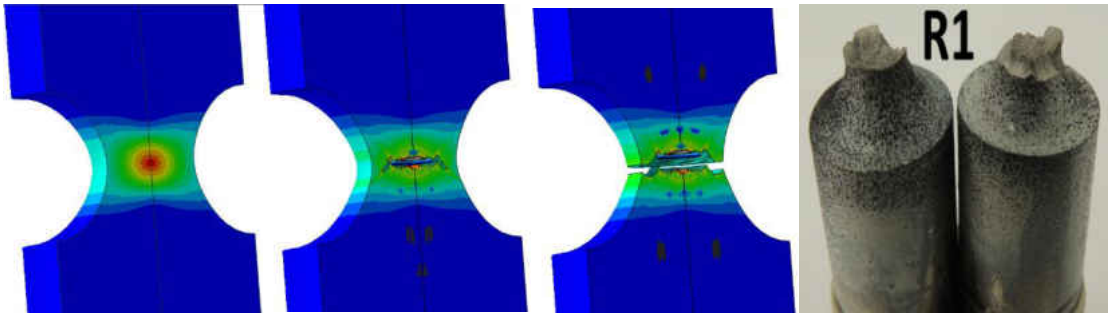

Figure 43: Deformation and fracture steps of the numerical simulation show a cup-cone fracture pattern for sharp notch round bar specimen ("R1"). The right figure shows the experimental result. The contour plot is the equivalent plastic strain in ABAQUS.

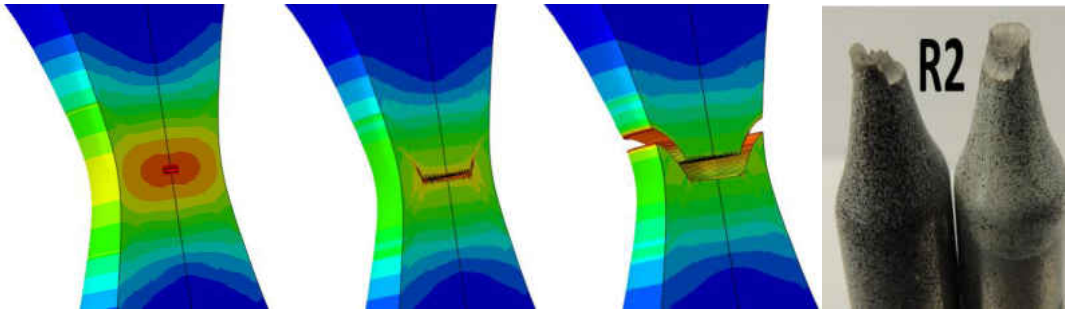

Figure 44: Deformation and fracture steps of the numerical simulation show a cup-cone fracture pattern for the large notch bar specimen ("R2"). The right figure shows the experimental result. The contour plot is the equivalent plastic strain in ABAQUS.

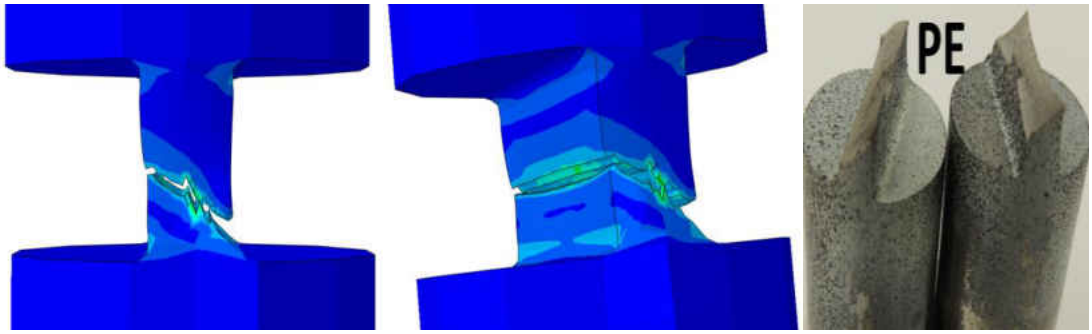

Figure 45: A comparison between the numerical simulation and experimental results shows a slant fracture mode for the plane strain specimen ("PE"). The right figure shows the experimental result. The contour plot is the equivalent plastic strain in ABAQUS.

4.10 Discussion and Conclusion

In this paper, the plasticity model with pressure and Lode angle dependence proposed by Bai and Wierzbicki [4] was extended to describe the evolution of yield surface for IN718. The Lode angle dependency parameter c_θ^s, which controls the shape of yield surface at the deviatoric plane, was found to be a function of equivalent plastic

strain and Lode angle parameter $c_\theta^s\left(\bar{\varepsilon}_{pl}, \bar{\theta}\right)$. The calibrated initial yield surface (2D plane stress condition) is shown in Figure 46. The classical von Mises and Tresca criteria are also plot for reference. Since there are no test data on compression or equi-biaxial tension, the yield behavior of IN718 was assumed to be symmetric between tension and compression ($c_\theta^c = 1$).

The evolution of yielding surface as plastic deformation continues is illustrated in Figure 47. This evolution can also be presented on the π-plane, as shown in Figure 48. It is worth noting that the yield surface changes its shape as plastic strain increases. It develops to an elliptical shape (von Mises criterion) when the equivalent plastic strain reaches about 0.10. It keeps changing shapes as it deformation continues, which develops to be a hexagon shape (Tresca criterion) at about 0.3 plastic strain. The current test number is very limited. More tests are needed to fully understand this evolution of yield surface since it describes the plastic behavior of Inconel 718 under different stress states. The suggested tests to examine this irregular yield surface include equibiaxial tension and shear/torsion loading conditions.

The calibrated 3D MMC fracture locus is shown in Figure 41. It is able to describe all test data points. It is interesting to find that the effect of the Lode angle on fracture is relatively small but the material plasticity has strong Lode angle dependency. The fracture locus is highly dependent on stress triaxiality while the plasticity has only some pressure dependency.

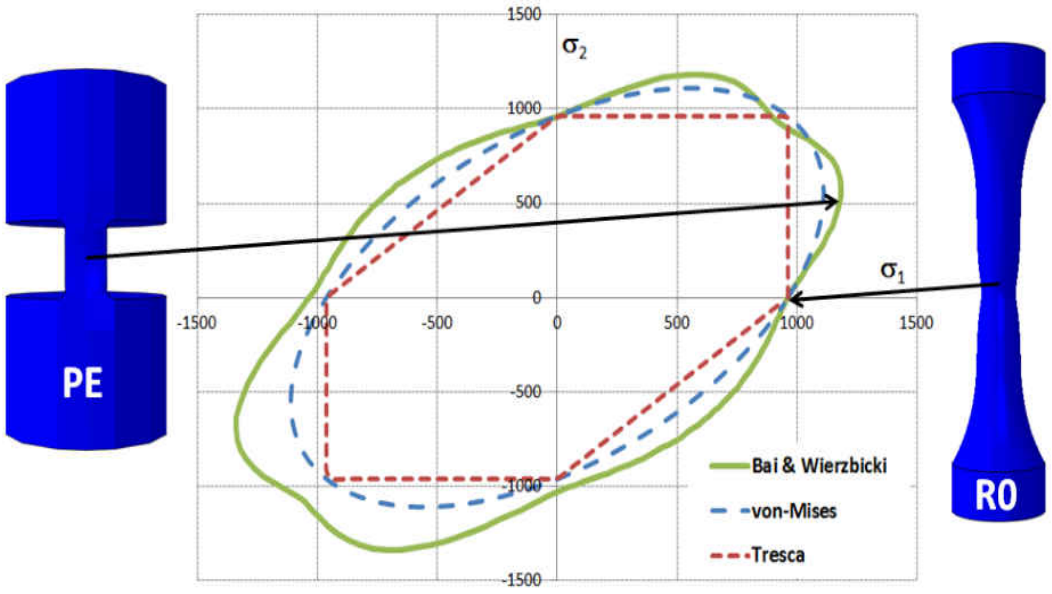

Figure 46: The calibrated initial yield surface for Inconel 718 (2D plane stress). The von-Mises and Tresca criteria are also plot for comparison. Two different stress states from the current tests are marked. The stress unit is MPa.

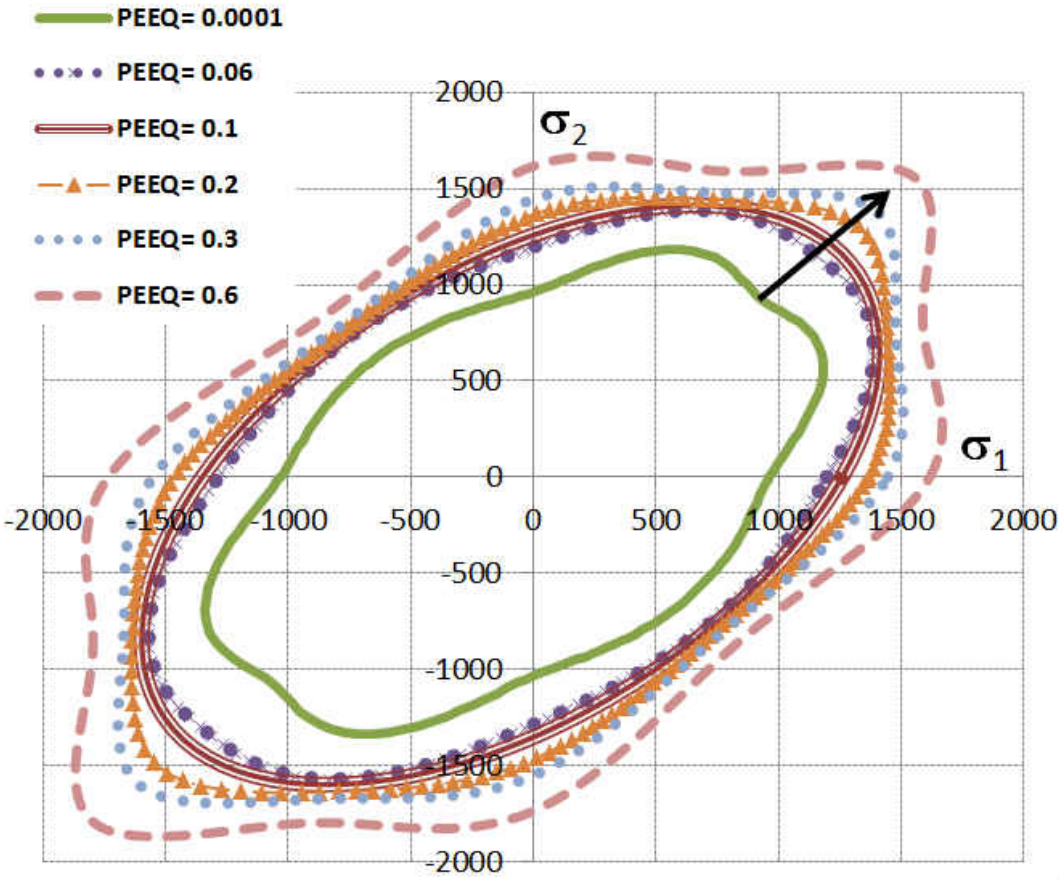

Figure 47: Evolution of 2D plane stress yield surface as the equivalent plastic strain (PEEQ) increases. The arrow shows the direction of evolution for the yield locus

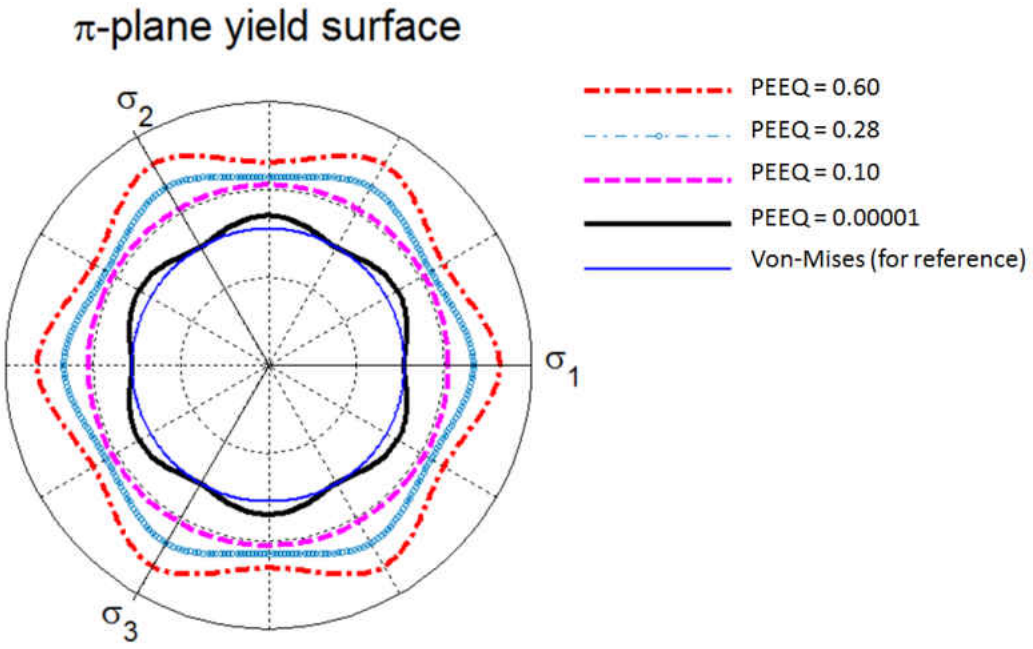

Figure 48: Evolution of the yield surface shape as the equivalent plastic strain (PEEQ) increases in the deviatoric stress plane (π-plane).

In summary, this paper presents experimental and numerical simulation results of Inconel 718 high temperature super alloy. Four types of specimens (one smooth round bar, two notched round bars, and one plane strain specimen) with different loading conditions were designed and tested under room temperature and quasi-static loading. It is found that the stress state parameters (stress triaxiality and Lode angle parameter) have noteworthy effects on the plasticity and fracture of Inconel 718. The plasticity model with pressure and Lode angle dependence proposed by Bai and Wierzbicki [4] was extended to describe the material's plasticity behavior, and the MMC fracture model [25] with post failure softening [60] was used to successfully predict both ductile fracture initiation and propagation.

In order to conduct model calibration and numerical verification, finite element analysis was set up. The proposed plasticity model and ductile fracture criterion were implemented into ABAQUS/Explicit by means of a user defined material subroutine (VUMAT). The final calibration gives satisfactory results. The force-displacement curves of the numerical simulations correlate very well with the experimental ones. An excellent match is achieved in terms of initial yield stress, strain hardening, and plastic deformation behaviors.

The MMC ductile fracture criterion was calibrated to fit the fracture test results. The sudden drop in the force-displacement curves was considered as the initiation of fracture. A Matlab code was created to help calibrate the MMC model. Material/element post-failure softening behavior was calibrated through iterative finite element simulations to match the correct fracture modes. Finally, both the fracture initiation and crack propagation in the finite element simulations show satisfactory agreement with test results for all four specimens.

CHAPTER FIVE:
A UNIFIED MATERIAL MODEL FOR MULTIAXIAL DUCTILE FRACTURE AND EXTREMELY LOW CYCLE FATIGUE OF INCONEL 718

5.1 Abstract

This paper summarizes an extensive work of experimental and numerical studies of extremely low cycle fatigue (ELCF) on IN718 under room temperature. The ELCF is focused on low numbers of cyclic loading (fewer than 100 cycles) of fatigue failure. The IN718 cyclic plasticity behavior and the Bauschinger effect are studied and simulated using the well-known nonlinear kinematic hardening law by J. L. Chaboche and his co-workers under different strain amplitudes and different stress states. Moreover, the Vocé isotropic hardening law was used in combination with the Bai-Wierzbicki plasticity model. The Bai-Wierzbicki plasticity model was used to capture the effect of different stress states on ELCF based on the stress triaxiality and Lode angle parameters. On the other hand, the modified Mohr–Coulomb (MMC) ductile fracture model for monotonic loading was extended by a new damage evolution rule to cover the ELCF regime. A new parameter was introduced to represent the effect of the cyclic loading at ELCF. The new parameter is responsible to capture the change of non-proportional loading direction between the current stress and the backstress tensors. A comparison between the experimental data and the finite element simulation results (by Abaqus/Explicit) shows excellent correlations. Lastly, a fractographic examinations and fracture modes simulations are presented.

5.2 Introduction

In-service complex engineering structures and their components are typically subjected to multiaxial stress states loading due to geometrical effects, residual stresses, or multi-directional loading [177]. Also, metal fatigue is considered to be one of the main mechanical failure modes in real applications [134, 178]. Therefore, the need to understand and investigate multiaxial fatigue of engineering materials has grown. Accurate and intensive studies, along with the advanced finite-elements simulations, will help to safely utilize materials and superalloys to their full capacity in engineering structures and components.

Inconel 718 (IN718) is a Nickel-base superalloy. IN718 has an FCC microstructure and is a polycrystalline Nickel-base superalloy with a high content of Cr and Fe that is fabricated by conventional melting and casting techniques. The examined IN718 chemical composition is shown in Table 14 as received. The usages of IN718 have been dramatically increased in many high-strength and high-temperature applications due to its exceptional characteristics. The common applications of IN718 are in the hot section of gas turbines, compressors and power generators (operating temperatures of 650°C.). For such applications, the machine start-up or shut-down are the most critical moments of the machines' life where most failures commonly occur. During these critical moments, Extremely Low Cycle Fatigue (ELCF) is highly susceptible due to the very large-strain cyclic loading. This would lead to an unexpected catastrophic failure in an unexpectedly short time. Hence, studying ELCF under different stress states and different

strain amplitudes will assist to understand and improve the materials' performance and life span in the machine's design stage [179-182].

The ELCF regime falls in between the ductile fracture due to monotonic loading and the Low cycle fatigue (LCF). The term ELCF describes cyclic loading with very-large strain that causes the material to fail under 100 cycles of reverse loading ($N_f < 100$) [183]. A common life example of ELCF are steel structures, i.e. steel bridge beams and welded joints, failing due to extreme loading conditions caused by earthquakes [184, 185]. ELCF, unlike other fatigue regimes, exhibits very large accumulated plastic strain during the very large-strain cyclic loading. This causes unique changes in the material hardening and softening behaviors during reverse loading processes. Another unique characteristic of ELCF different from other fatigue regimes is its fracture mode. ELCF fracture mode (fracture initiation and propagation) behaves similarly to ductile fracture mode and exhibits the same surface profile. This similarity is due to the very short life of this regime, as well as the rapid crack initiation and propagation of fatigue cracks in the ELCF regime. Lastly, the ELCF fracture initiates inside of specimens and propagates towards the outer radius. Conversely, the fracture of the other fatigue regimes usually initiates from the outer radius and propagates inwards [36, 183].

Throughout the past decades, numerous researches studied and developed many constitutive models to describe the metals cyclic plasticity behavior and the Bauchinger effect. The constitutive models that are directly influenced by its kinematic hardening rule in the yield surface consistency status are known as the "*coupled models,"* such as those in Refs. [15-19, 122, 129, 186-196]. All these models are originally based on

Prager model in Ref. [197]. The other constitutive models category is known as the "*uncoupled models."* These models are indirectly influenced by the material's kinematic hardening rule, such as those in Refs. [113, 115, 117, 198]. For the sake of simplicity, readers are advised to Refs. [11, 13] for more extensive explanations. The current research adopts a simple and well-known nonlinear kinematic hardening model that was invented by J. L. Chaboche and his co-workers [15, 17].

The cyclic plasticity behavior of Nickel-base superalloys under LCF regime has been studied [65, 130, 199-206]. Manonukul et. al. [199] examined the behavior of Nickel-base superalloy "*C263*" in the Low Cycle Fatigue regime (LCF) ($100 \leq N_f \leq 10000$) using a multiaxial physically-based constitutive model. The results of their research show reasonable correlations when compared to the experimental data. More Nickel-base superalloy researches were conducted for thermomechanical fatigue behavior using viscoplastic constitutive models [130, 200-203, 206]. Recently, Becker and Hackenberg [65] proposed a constitutive model for IN718 under LCF that considers a full range of thermal and mechanical fatigue conditions (TMF) at small strains. In addition, Gustafsson et. al. [204] proposed a simple constitutive model for IN718 using Ohno and Wang model [205] for intermediate temperatures (400°C) in LCF. Their model and numerical simulation results show good agreement with the experimental data.

Many ongoing researches have focused on studying and predicting the ELCF life of different materials under multiaxial stresses. Early studies, in Refs. [32, 35, 207, 208], show that the experimental specimens fail sooner than the fatigue life predicted by the Coffin-Manson strain-based law [209, 210]. Studies observed that the Coffin-Manson law

can well-predict the metal's life in LCF, yet it over-predicts the metal's life in ELCF regime [33, 35]. Thus, it is concluded that the predicted life by Coffin-Manson law does not fit well in the range of ELCF [34, 35]. Therefore, studies [33, 39, 208] suggest adding an additional factor to Coffin-Manson law to improve the ELCF life prediction. This additional factor is called the "*damage effect*" which represents the huge plastic damage accumulation in the materials ductility during ELCF. However, researches are not yet certain whether or not the huge damage is responsible for dropping the fatigue life. Nevertheless, the plastic damage accumulation in the material's ductility in ELCF is verified to be irreversible [211]. Moreover, other studies improved the ELCF prediction by contributing the effect of plastic internal void growth and coalescence in ELCF [212, 213]. It is apparent that studies on ELCF of IN718 are exceedingly rare, although abundant studies on IN718 in Low Cycle Fatigue (LCF) can be found in Refs. [40, 154, 203, 214-217].

Other approach of research studies [212, 218-220] predicted ELCF by extending ductile fracture models under monotonic loading to the case of cyclic loading, or ELCF. This approach was inspired by the similarities in the crack surface and crack modes under monotonic loading and ELCF (i.e. cup-cone fracture surface for round specimens). As a result, it was postulated that their failure mechanisms share similar crack formation characteristics of ductile fracture failure mode. This approach of research overcomes the shortcoming of traditional fatigue models, i.e. Coffin-Manson law. It was found that the traditional fatigue models could not accurately model ELCF due to the underlying fundamental physical processes, such as crack initiation and propagation mechanisms, in

ELCF. Mainly, the extreme plastic strain that accompanies ELCF nullifies the stress-intensity-based of ΔK or ΔJ models of *Paris and Erdogan* [221]. In addition, these types of stress-intensity-based models require or presume the existence of a sharp crack or defect, which is missing in most real application details. Secondly, in real applications such as earthquakes on steal bridges, loading histories are very random with few numbers of cycles. This makes it very challenging to count the cycles by adopting the conventional counting techniques, i.e. rainflow analysis [222] or the traditional strain-life approaches. Therefore, extending ductile fracture models from monotonic loading to the case of cyclic loading merits extensive consideration. Kanvinde and Deierlein [212] extended the Rice and Tracey ductile fracture model [46] to develop a cyclic void growth model (CVGM) that applies for ELCF life prediction. Although the CVGM shows fairly accurate results of predicting ELCF, it is limited by some assumptions stated in the study. Bao and Treitler [218] proposed a new ductile fracture model for compression-tension loading condition based on a model presented earlier in Ref. [223] . This fracture model gives good results but limited to a two-stage loading process; pre-compression followed by tension to failure. Bai [219] extended a ductile fracture model in Ref. [4] by proposing two weighting functions for 1045 steel. One function considers the nonlinear damage evolution and the other function incorporates the effect of change in loading directions. This study implies the importance of a nonlinear damage evolution in ELCF loading conditions. A very recent study by Wen and Mahmoud [220] extended their ductile fracture model in Ref. [224] to predict ELCF life span.

This study has three main objectives. First, it focuses on defining a simple constitutive model that describes both monotonic and very large-strain cyclic loading behavior of IN718 at room temperature. The plasticity behavior of IN718 is calibrated and modeled by combining the Chaboches' nonlinear kinematic hardening model [15, 17] with the Bai-Wierzbicki plasticity model [4]. The Bai-Wierzbicki plasticity model takes into account different multiaxial stress states. The multiaxial stress states are described by two parameters: stress triaxiality and Lode angle parameter. Second, it extends the application of the modified Mohr–Coulomb (MMC) ductile fracture model to ELCF. This study of IN718 under ELCF regime is a continuation of the parallel studies in Refs. [225, 226]. The model extension proposed herein extends the MMC ductile fracture application to cover the ELCF context by introducing a new factor that considers the cyclic loading effect, which is inspired by Ref. [219]. This model represents the fundamental physics of the accumulated plastic strain associated with ELCF and it can be conventionally investigated and simulated through FEM. Third, an evaluation of crack initiation and propagation due to ELCF will be addressed. This evaluation is assessed through a fractographic examination of the specimens' experimental fracture surfaces. A comparison between the experimental results and the finite element simulations (by Abaqus/Explicit) will be exposed. All the results of this paper are verified based on a series of experimental tests data.

Table 14: The IN718 specimen's chemical composition in %wt. (as received)

Ni	Cr	Mo	Cb + Ta	N	Si	Cu	Al	Co	C	S	Mn	B	P	Fe

52.9	**18.41**	**2.89**	**5.17**	**0.0078**	**0.08**	**0.06**	**0.58**	**0.19**	**0.04**	**0.0005**	**0.09**	**0.004**	**0.007**	**Bal.**

5.3 Characterization of the stress state

It is known that an arbitrary stress tensor $[\sigma_{ij}]$ can be simplified to three principal stresses ($\sigma_1, \sigma_2,$ and σ_3) by coordinate system rotation. It has been shown that a stress state can be uniquely described by two dimensionless parameters, stress triaxiality η (mean stress normalized by equivalent stress) and Lode angle parameter $\bar{\theta}$ (related to the normalized third deviatoric stress invariant), which is defined as follows [43]:

$$\eta = \frac{-p}{q} = \frac{\sigma_m}{\bar{\sigma}} = \frac{\sigma_1+\sigma_2+\sigma_3}{3\bar{\sigma}} \tag{129}$$

$$\bar{\theta} = 1 - \frac{6\theta}{\pi} = 1 - \frac{2}{\pi}\arccos\xi \tag{130}$$

Here, σ_m is the mean stress; $\bar{\sigma}$ is the equivalent stress; ξ is defined as normalized third deviatoric stress invariant, $\xi = \frac{J_3}{\bar{\sigma}^3}$. Here $J_3 = s_1 s_2 s_3$ is the third deviatoric stress invariant. The parameter ξ can be further related to the Lode angle θ by $\xi = \cos(3\theta)$. The range of $\bar{\theta}$ is $-1 \leq \bar{\theta} \leq 1$. Now, all isotropic loading conditions can be uniquely characterized by the above defined set of parameters ($\eta, \bar{\theta}$). These two parameters form a stress state plane [4, 43]. Material mechanical properties, for example, yield strength, necking and fracture limits, can be represented as the third axis to this plane. For a monotonic loading condition, these two stress state parameters (η and $\bar{\theta}$) remain constant, so it corresponds to one point on this plane. For a nonlinear strain/stress path, it

gives a curve on this plane. The set of parameters provide a novel way to describe arbitrary stress states and strain paths.

5.4 Design of specimen geometries

In this study, a number of specimens, with four different shapes, were tested under large-strain cyclic loading of tension and compression. The four distinctive shapes are a smooth round bar, a round bar with a small external circular notch, a round bar with a large external circular notch, and a flat plane strain bar. Three-dimension (3D) sketches and real machined parts for these geometries are illustrated in Figure 74. In addition, more information about key dimensions are demonstrated in Table 23 in reference to Figure 50. These geometries are designed in a way to ensure fractures initiate at desired stress states. Also, there are analytical solutions of stress state parameters available for these specimens in Ref. [43]. These four types of specimens are usually used to study the stress triaxiality and Lode angle effects on the plasticity and fracture of metals. To easily distinguish each specimen, Table 23 explains the denotations used hereinafter.

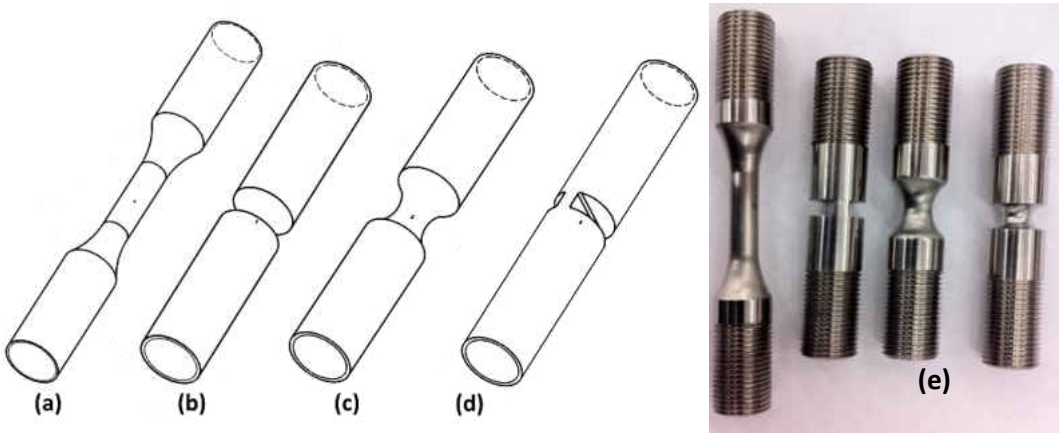

Figure 49: A 3D sketch of (a) smooth round bar , (b) small radius notch bar, (c) large radius notch bar, and (d) plane strain flat bar, (e) real specimens before testing denoted as R0, PE, R2, and R1. from left to right.

Table 15: Denotation of sample names with their key dimensions (unit: mm)

Specimen type	**Denotation**	**Notch radius, R**	**Minimum diameter, d**	**Shoulder diameter, D**
(a) Smooth round bar	**R0**	N/A	6.350	12.700
(b) Small radius notched bar	**R1**	3.175	6.350	12.700
(c) Large radius notched bar	**R2**	9.525	6.350	12.700
(d) Plane strain	**PE**	N/A	3.048	12.700

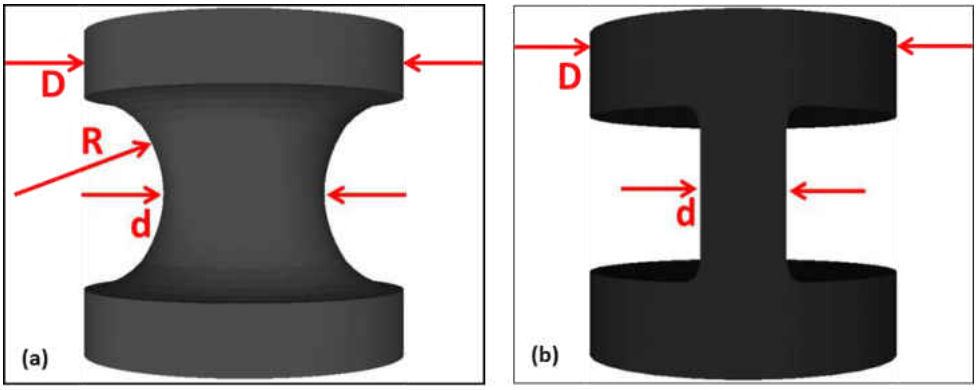

Figure 50: Main geometries and dimensions of the round bar (a), and the plain strain bar (b).

5.5 Experiments

All specimens were fabricated from the same piece of rod to ensure microstructure similarity. Four types of specimens with different shapes were tested at room temperature and under extreme large-strain cyclic loading of tension and compression. An MTS servohydraulic testing machine with a 100 kN load cell capacity was used in our cyclic load tests at a strain rate of 0.003 /sec. The tests data of load-displacement were simultaneously recorded by the testing machine and an optical measurement system. The surface strains were recorded and calculated using a Digital Imaging Correlation (DIC) software provided by Correlated Solutions Inc. (Vic2D 2009). In order to get an accurate image correlation in DIC, the specimens were spray painted in white then speckle patterned in black dots for better image contrast. The DIC results were used to obtain the experimental force-displacement curves, and to achieve full filed strain measurement. A test series were run until complete fracture of specimens under different large-strain amplitudes (as summerized in Table 24). The force-displacement curves of the cyclic loading are recorded and illustrated. The reference gauge length, gauge

elongation and number of cycles to fail (N_f) are summarized in Table 24. The gauge length (L_o) for each specimen is the initial gauge length (before testing) that was used to calculate the strain around/at the critical area. The engineering strain is defined as $\varepsilon_E = (L - L_o)/L_o$ where L is the current gauge length reading from the DIC. The gauge length is fixed to enable comparing the force-displacement results from the experiment and the simulation data. Also, the test elongation is provided in Table 24 to check if all the tests failed within the ELCF regime.

Table 16: Experimental data and measurements of the ELCF tests of IN718.

Test number	Specimen	Gauge length, mm	Test Elongation	Number of Cycles to fail, N_f
1	**R0**	15.2	33%	NA*
2	**R1**	9.16	33%	4
3	**R1**	9.16	16%	9
4	**R2**	15.98	33%	10
5	**R2**	15.98	16%	41
6	**R2**	15.98	5%	51
7	**PE**	4.19	33%	10
8	**PE**	4.19	16%	21
9	**PE**	4.19	5%	43

* The "R0" specimen significantly buckled after 10 cycles during the compression loading and accordingly, the test was stopped.

As a base line, the experimental measurements of fracture under monotonic loading conditions of the same IN718 are reported by the same authors and summarized in Table 17. The classical Bridgman solutions [42] was adopted to calculated the stress triaxiality and the fracture strain. These data were used to construct the 2D fracture locus in the space of stress triaxiality versus the equivalent strain to fracture as illustrated in Figure 51. It is seen that the equivalent plastic strain to fracture ($\bar{\varepsilon}_f$) of IN718 generally decreases as the stress triaxiality increases.

Table 17: An experimental data summary of stress triaxiality, Lode angle, and equivalent plastic strain to failure for IN718 under monotonic loading, taken from Ref. [225].

Specimen	Gauge length	Gauge Elongation	Displacement at fracture	Theoretical solution		
				η	$\bar{\theta}$	$\bar{\varepsilon}_f$
R0	15.27 mm	27.7%	4.23 mm	0.33	1	0.680
R1	9.16 mm	7.9%	0.72 mm	0.74	1	0.386
R2	15.978 mm	10.2%	1.63 mm	0.51	1	0.442
PE	4.19 mm	26.7%	1.12 mm	0.57	0	0.400

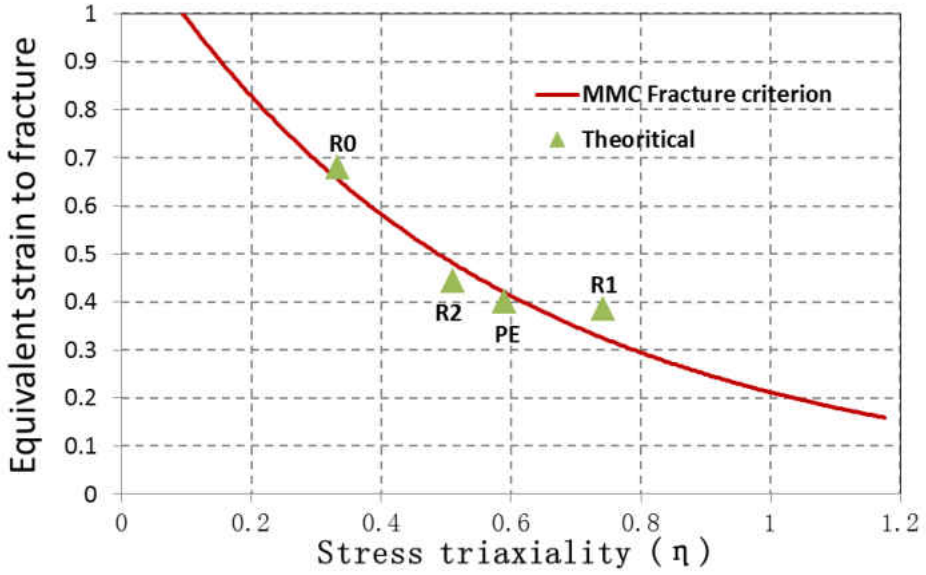

Figure 51: Calibrated MMC 2D ductile fracture locus (setting $\bar{\theta} = 1$) shows the relationship theoretical solution of stress triaxiality vs. the theoretical solution of equivalent fracture strain for IN718 [225].

The experimental results of ELCF are shown in Figure 52, which reveals a strong dependency of the fracture strain on the stress triaxiality. This effect can be firstly seen in the monotonic loading (¼ cycle to failure) in the strain-life plot. This fact propagates evidently into the ELCF regime. The slopes which represent R2 and PE strain–life curves are almost identical since the stress triaxiality of both specimens are very close. However, the strain–life curve slope of the R1 specimens is much steeper since it has a higher value

of stress triaxiality. Hence, we can affirm from the ELCF experimental results that the stress triaxiality is inversely proportional to the strain–life curve slope under the condition of fully reversed loading. The strain amplitudes were calculated using Eq. (131). The changes in the diameter and the axial displacement of the specimens during the ELCF tests were accurately recorded and measured by the aid of DIC.

$$\Delta\bar{\varepsilon} = \begin{cases} 2\ln\left(\frac{D_0}{D}\right), & for\ round\ bar\ specimens \\ \frac{\sqrt{3}}{2}\ln\left(\frac{t_o}{t}\right), & for\ plane\ strain\ specimens \end{cases} \tag{131}$$

where D_0 , D, t_0 and t are the initial gauge diameter, current gauge diameter, initial thickness, and current thickness, respectively. The initial diameter and the initial thickness were identified and recorded, by the DIC, before a test started. The current diameter and thickness were measured at the peaks of the displacement/strain during the cyclic test.

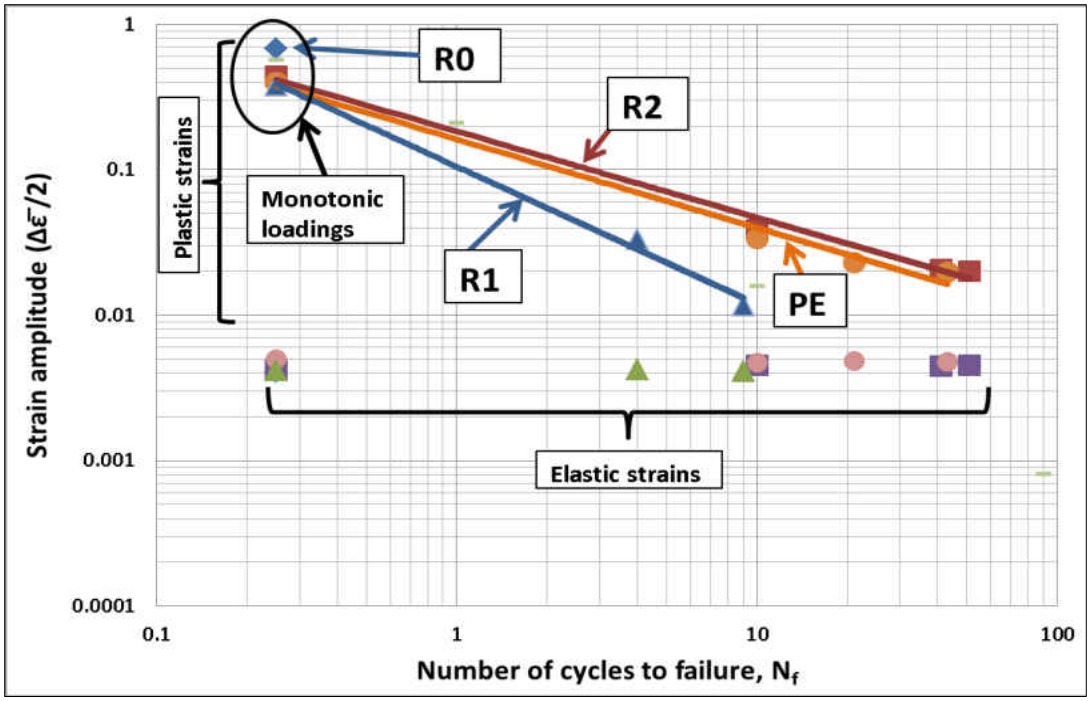

Figure 52: The strain–life curves for all specimens under ELCF regimes of IN718.

The fractured specimens under ELCF are shown in It is evident from the fracture surface morphologies of each specimen that the fracture mechanism is very similar to that of the ductile fracture under monotonic loading as shown in Figure 77.

. It is clear from the fracture surface morphologies of each specimen that the fracture mechanism of ELCF is very similar to that of the ductile fracture under monotonic loading. Fatigue cracks in ELCF tended to initiate in the gauge center and propagate towards the surface. The round bars specimens (R1, R2) exhibits a cup-cone fracture mode. The cup-cone fracture mode usually starts with micro cracks in the gauge center followed by crack propagation towards the outer radius. Then, a shear lip is formed at the circumferential edge of the outer radius (which is close to plane strain

condition). On the other hand, the plane strain specimens (PE) show a slant fracture mode, which was caused by a shear band generated in the gauge section.

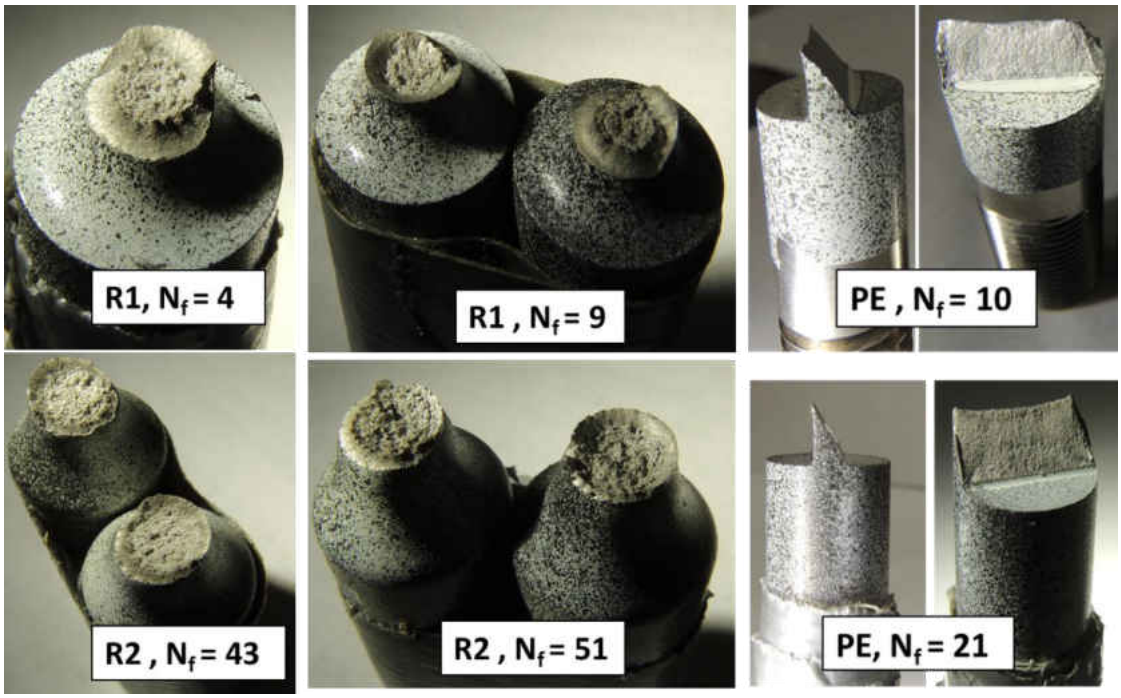

Figure 53: Some examples of fractured surfaces morphologies under ELCF conditions.

5.6 Plasticity Model and Fracture/Fatigue Criterion

5.6.1 Plasticity behavior model under cyclic loading conditions

The plasticity behavior of IN718 under tension-compression cyclic loading conditions is assumed to involve a combined hardening rule; kinematic hardening and isotropic hardening. Chaboche and his co-workers [15, 17] proposed a model of a decomposed nonlinear kinematic hardening rule of backstresses, which was adopted in this study (Eq. (149)). Essentially, the Chaboche model is a superposition of several Armstrong and Frederick kinematic hardening rules [129]. Three nonlinear backstress

components ($\boldsymbol{\alpha} = \boldsymbol{\alpha_1} + \boldsymbol{\alpha_2} + \boldsymbol{\alpha_3}$) were used in this paper to simulate the stable IN718 hysteresis loop of the smooth round bar specimen ("R0"). The Chaboche model, basically, decomposes a stable hysteresis loop into three major parts: (α_1) the initial high modulus at beginning of yielding that stabilizes rapidly, (α_2) the transient nonlinear part of a stable hysteresis curve, and (α_3) the linear constant modulus region at a higher strain extent with $B_3 = 0$.

$$\dot{\boldsymbol{\alpha}}_{\mathbf{i}} = \mathrm{C_i}\dot{\boldsymbol{\varepsilon}}^{\mathbf{pl}} - \mathrm{B_i}\,\boldsymbol{\alpha}_{\mathbf{i}}\ \ \dot{\bar{\varepsilon}}^{pl}, \qquad \boldsymbol{\alpha} = \sum_{\mathrm{i}=1}^{\mathrm{n}} \dot{\boldsymbol{\alpha}}_{\mathrm{i}}\ , \qquad where\ \mathrm{n} = 3 \tag{132}$$

$$\dot{\bar{\varepsilon}}^{pl} = \sqrt{\left(\frac{2}{3}\right)\,\dot{\boldsymbol{\varepsilon}}^{\mathbf{pl}}_{\mathbf{ij}} : \dot{\boldsymbol{\varepsilon}}^{\mathbf{pl}}_{\mathbf{ij}}} \tag{133}$$

where α_i is the backstress tensor, C_i and B_i are positive material constants, and $\dot{\bar{\varepsilon}}^{pl}$ is the accumulated equivalent plastic strain rate which is described in Eq. (133).

Moreover, a plasticity model proposed by *Bai and Wierzbicki* [4] has been adopted in combination with the isotropic strain hardening to describe the effect of different stress states (see Eq. (150)). This model incorporates the effects of hydrostatic pressure and the Lode angle parameter. The plastic flow potential used in this paper is shown in Eq. (135). The first term of Eq. (150), $\sigma\left(\bar{\varepsilon}_{\mathrm{pl}}\right)$, takes the Vocé isotropic strain hardening function, as shown explicitly in Eq.(136), where σ_y, Q and b are the yield stress at zero plastic strain, the maximum strain hardening of the yield surface, and the rate at which the size of the yield surface change, respectively [107, 108]. The second term of Eq. (150) is the effect of the hydrostatic pressure on yield, where c_η and η_o are two material parameters that need to be calibrated under monotonic loading conditions. It should be noted that the term of $\left[1 - c_\eta\left(\eta - \eta_o\right)\right]$ should be bounded within certain

limits for the very high or very low stress triaxiality region. For example, $0.5 \leq \left[1 - c_\eta \left(\eta - \eta_o\right)\right] \leq 2.0$ was used in our simulations. The third term in this model is the Lode angle dependence, where a correction term, $\left(\frac{m+1}{m}\right)$, was introduced to make it more user-friendly [225]. This is slightly different from the original term [4]. The Lode angle term consists of four material constants c_θ^s, c_θ^t, c_θ^c, and m that need to be calibrated under monotonic loading condition as well. The terms c_θ^s, c_θ^t, c_θ^c are relative and, at least, one of them equals one. The parameter γ, defined in Eq. (137), is the strength difference between von Mises and Tresca in the deviatoric stress plane. After modification and normalization of γ , it ranges from $0 \leq \gamma \leq 1$. In axial symmetry and plane strain conditions, the γ is 1 and 0, respectively. The first term of Eq. (135) considers the kinematic hardening, which is defined in Eq. (149).

$$\sigma\left(\varepsilon_{pl}, \eta, \theta\right) = \sigma\left(\bar{\varepsilon}_{pl}\right)\left[1 - c_\eta \left(\eta - \eta_o\right)\right]\left[c_\theta^s + \left(c_\theta^{ax} - c_\theta^s\right)\left(\frac{m+1}{m}\right)\left(\gamma - \frac{\gamma^{m+1}}{m+1}\right)\right] \quad (134)$$

$$f = \sqrt{\frac{3}{2}\left[\mathbf{S} - \boldsymbol{\alpha}\right] : \left[\mathbf{S} - \boldsymbol{\alpha}\right]} - \sigma\left(\bar{\varepsilon}_{pl}, \eta, \theta\right) = 0 \quad (135)$$

$$\sigma\left(\bar{\varepsilon}_{pl}\right) = \sigma_y + Q\left(1 - e^{-b\bar{\varepsilon}_{pl}}\right) \quad (136)$$

$$\gamma = 6.4641\left[\sec\left(\theta - \pi/6\right) - 1\right] \quad (137)$$

5.6.2 Ductile fracture criteria with damage accumulation for ELCF

The modified Mohr-Coulomb criterion (MMC) [25] is used to determine the fracture locus of IN718 and to predict crack initiation and growth under different stress states (Eq.

(151)). The MMC model had shown capable of capturing the coupling effect of stress triaxiality and Lode angle. This phenomenological fracture criterion has shown excellent prediction capabilities of fracture onset in various applications under monotonic loading conditions [49, 50, 57, 173-175]. The six parameters (A, N, $\tilde{c}_{\theta}^{s}$, $\tilde{c}_{\theta}^{ax}$, c_1, and c_2) in Eq. (151) are material parameters that need to be calibrated using proportional loading condition tests.

$$\bar{\varepsilon}_f(\eta,\bar{\theta}) = \left\{ \begin{array}{l} \frac{A}{c_2}\times \left[\tilde{c}_{\theta}^{s} + \frac{\sqrt{3}}{2-\sqrt{3}}(\tilde{c}_{\theta}^{ax} - \tilde{c}_{\theta}^{s})\left(\boldsymbol{sec}\left(\frac{\bar{\theta}\,\pi}{6}\right) - \mathbf{1}\right)\right] \\ \qquad \times \left[\sqrt{\frac{1+c_1^2}{3}}\ \boldsymbol{cos}\left(\frac{\bar{\theta}\,\pi}{6}\right) + \boldsymbol{c_1}\left(\eta + \frac{1}{3}\,\boldsymbol{sin}\left(\frac{\bar{\theta}\,\pi}{6}\right)\right)\right] \end{array} \right\}^{-1/N} \tag{138}$$

$$dD = \frac{d\bar{\varepsilon}_{pl}}{\bar{\varepsilon}_f(\eta,\bar{\theta})} \tag{139}$$

Under monotonic loading conditions, a linear damage accumulation rule (Eq.(139)) is often used, where dD is the damage incremental and $d\bar{\varepsilon}_{pl}$ is the change of equivalent plastic strain. The damage indicator D ranges within [0, 1], where $D = 0$ represents a virgin material (flawless) and $D = 1$ represents fracture initiation.

In this paper, the MMC ductile fracture model is extended to consider ELCF regime. Two more weighing functions are introduced in conjunction with the MMC fracture locus. They are set as shown in Eq. (140), and explicitly expressed in Eqs. (141), and (142). These two functions are presumed to act independently and concurrently throughout a loading process. They are essential in this research to consider the complex cycling loading condition in order to accurately predict the material's failure within the

ELCF regime. The first extension function, $g(D)$, takes role in calculating the damage indicator evolution ,as the equivalent plastic strain increases, in a nonlinear manner even under monotonic or proportional loadings. The effect of this part is seen in Figure 54(a). Varying the value of the controlling parameter (c_g) from a negative to positive values changes the damage accumulation behavior from convex to concave, respectively. The damage evolution can be reset to behave linearly by setting $c_g = 0.0001$, a very small value to avoid mathematical singularity.

$$dD = g(D)\,.\,h(D,\mu)\,\frac{d\bar{\varepsilon}_{pl}}{\bar{\varepsilon}_f(\eta,\bar{\theta})} \tag{140}$$

$$g(D) = \left(c_g D + \frac{c_g}{e^{c_g}-1}\right) \tag{141}$$

$$h(D,\mu) = \left(1 + c_h\, D^{\beta_1}\mu^{\beta_2}\right)^k \tag{142}$$

The second extension function, $h(D,\mu)$, considers the effect of the change in the non-proportional loading direction between the current stress and the backstress tensors. Hence, the function $h(D,\mu)$ takes an important role in incorporating the effect of cycling loading during ELCF. The effect of this part is seen in Figure 54(b). Accordingly, this extension function does not affect the damage evolution during proportional loading process. This extension function is based on a new scalar parameter (μ), which can capture the effect of cycling loading conditions and incorporate it in our ductile fracture model. The parameter μ is expressed explicitly in Eq. (143), which considers the accumulated change of another parameter (χ) defined in Eq. (144). This scalar parameter χ represents the key source of the loading path change. The range of χ is $0 \leq \chi \leq 2$. Here, the effect of cyclic loading is detected whenever the

parameter χ becomes non-zero. Finally, the two weighting functions consist of five material parameters c_g , c_h , β_1 , β_2, and k that need to be calibrated under cyclic loading condition tests.

$$\mu = \int_0^{\bar{\bar{\varepsilon}}_{pl}} \chi \; d\bar{\varepsilon}_{pl} \tag{143}$$

$$\chi = 1 - \frac{\boldsymbol{\sigma_{ij}} : \boldsymbol{\alpha_{ij}}}{\|\boldsymbol{\sigma_{ij}}\| \cdot \|\boldsymbol{\alpha_{ij}}\|} \tag{144}$$

where $\boldsymbol{\sigma_{ij}}$, $\boldsymbol{\alpha_{ij}}$ are stress tensor and backstress tensor, respectively.

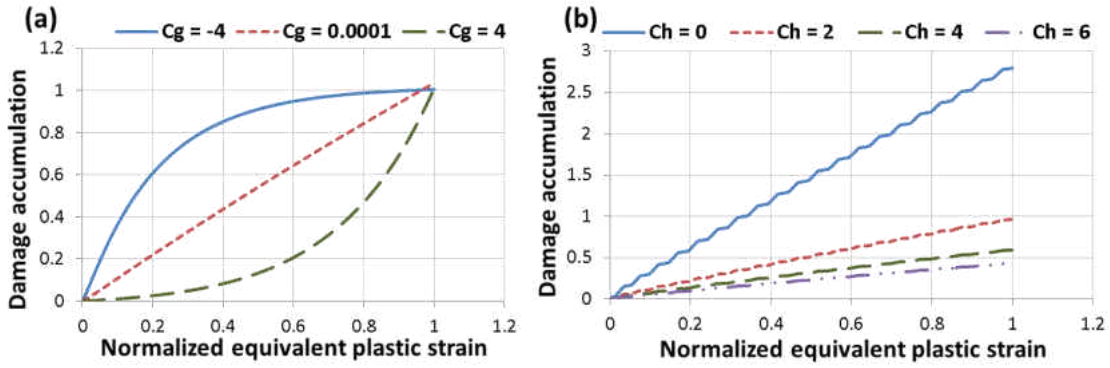

Figure 54: Two plots show the effect of two extended functions on the damage evolution during the loading process. The left plot (a) shows the effect of c_g on the nonlinear damage evolution. The right plot (b) shows the effect of c_h on the damage accumulation under non-proportional loading.

In the same vein, simulating the fracture propagation and getting the correct crack modes (especially the slant fracture in plane strain conditions and the cup-cone failure mode in round bars), a material or element softening after fracture initiation was found to be necessary [56, 60, 176, 225]. A general form of the post-fracture softening law is introduced and shown in Eq. (145). This is represented by the softening

coefficient β. The symbol $\tilde{\sigma}_{yield}$ is the softened flow stress, and $\bar{\sigma}_{yield}$ is the strain-hardening flow stress without damage. The coefficient β is assumed to be a nonlinear function of damage indicator D (see Eq. (146)), where D_c and w are two material softening parameters that will be calibrated later. Note that the softening law is effective only after the fracture initiates ($D > 1$). The fracture initiates when $D = 1$, which corresponds to $\beta = 1$. Accordingly, a complete split of the material points happens when $D = D_c$, after which the material element shows no resistance to load [56]. In other words, the parameter D_c is the value of damage indicator when an integration point of an element in the Abaqus/Explicit user defined material subroutines will be deleted.

$$\tilde{\sigma}_{yield} = \begin{cases} \bar{\sigma}_{yield} & if\ 0 \leq D < 1 \\ \beta\ \bar{\sigma}_{yield} & if\ 1 \leq D \leq D_c \end{cases} \tag{145}$$

$$\beta = \left(\frac{D_c - D}{D_c - 1}\right)^w \tag{146}$$

5.7 Model Calibration Procedures

This section will present the calibration procedures of the proposed plasticity and fracture model. Model parameters are determined by comparing the numerical simulation results (using Abaqus/Explicit) to the experimental results.

5.7.1 Plasticity model calibration

The proposed plasticity model was implemented to Abaqus/Explicit as a material subroutine (VUMAT) [227]. The calibration of the plasticity model went through two

stages to find the optimum parameters set. Firstly, the decomposed nonlinear kinematic hardening rule with three back stress tensors, Eq. (149), were calibrated by using a stable-large strain amplitude hysteresis loop of the smooth round bar ("R0") specimen, as seen in Figure 55. The method used in this research to obtain the initial calibration of the kinematic hardening model parameters (C_i and B_i) adopted from *Bari & Hassan* in Ref. [11]. The method, basically, divides a stable hysteresis loop into three critical segments: (α_1), (α_2), and (α_3). Secondly, the calibrated parameters (C_i and B_i) were then implemented to Abaqus/Explicit and optimized in order to perfectly simulate the experimental stable hysteresis loop (Figure 55). The optimized kinematic hardening model parameters are listed in Table 18. These parameters were implemented to the simulations of all other specimens.

The remaining material parameters of the plasticity model about the pressure dependency and Lode angle dependency have been discussed comprehensively in Ref. [225]. However, two slight changes took place in this paper. These two changes were related to the parameters (c_η) and (c_θ^s) in Eq. (150). The value of (c_η) has been increased from 0.11 to 0.40 due to the material's high pressure dependency in the presence of the nonlinear kinematic hardening rule. The other change is the parameter (c_θ^s) becomes a constant instead of a function of the equivalent plastic strain. The remaining plasticity model parameters remain the same, as in Ref. [225] and are listed in Table 19.

Table 18: List of material parameters used in the kinematic hardening model

C_1 (MPa)	B_1	C_2 (MPa)	B_2	C_3 (MPa)	B_3
310000	355	240000	1999	900	0

Table 19: List of material parameters used in the plasticity model

E, (GPa)	***ν***	**σ_y,** (MPa)	**Q ,** (MPa)	**b**	**c_η**	**η_o**	**c_θ^s**	**c_θ^{ax}**	**m**
200	0.284	45.1	100.4	35.425	0.40	0.333	0.866	1	0.75

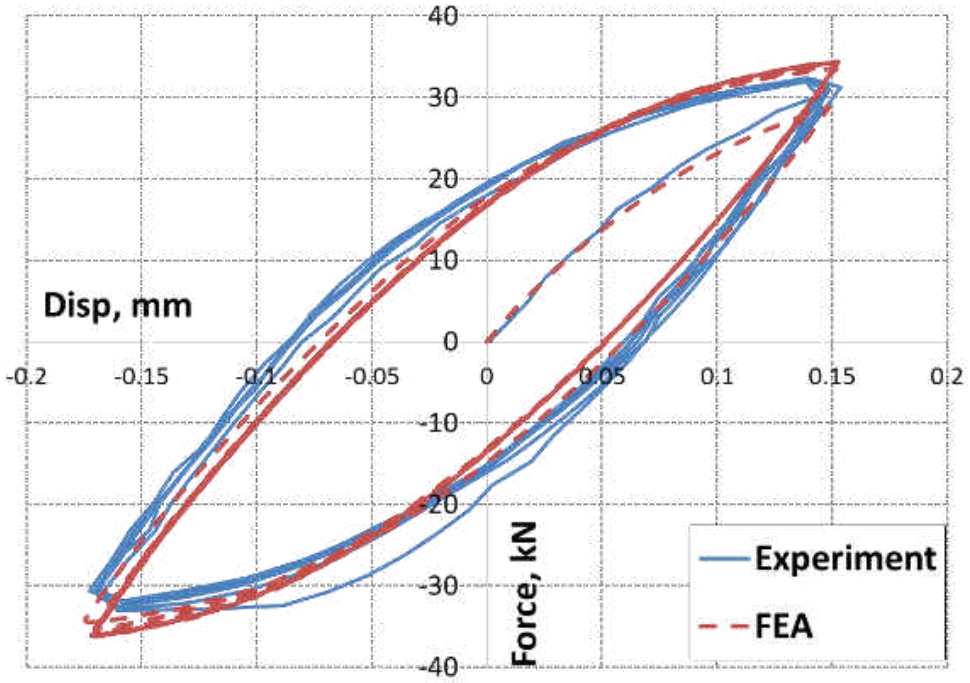

Figure 55: Strain-controlled stable hysteresis loops of the smooth round bar ("R0"). The comparison between the experiment and numerical force-displacement curves shows excellent correlation.

5.7.2 MMC fracture locus and the damage accumulation rule calibration

The MMC ductile fracture locus parameters have been calibrated under monotonic loading and extensively explained in the parallel paper [225]. These calibrated

parameters (see Table 10 and Table 11) well predicted ductile fracture initiation under monotonic loading conditions. A 3D geometrical representation of the MMC fracture locus is shown in Figure 57.

The remaining five material parameters (c_g , c_h , β_1 , β_2, and k) of the extension functions for damage accumulation were calibrated by using the cyclic loading tests data. Firstly, finite element simulations were conducted up to fracture initiation for each test case without involving the fracture option in order to get the histories of stress triaxiality, Lode angle parameter, and the accumulation of nonlinearity parameter (μ) under the cyclic loading conditions. A Matlab code was created to run the damage evolution integration, as in Eq. (140), to get a good estimation of the five constants such that the calculated damage accumulation (D) for all the cases is as close to unity as possible (Figure 56). An optimization code was set to optimize starting from the initial set of parameters of the extension functions. The optimized parameters are summarized in Table 21.

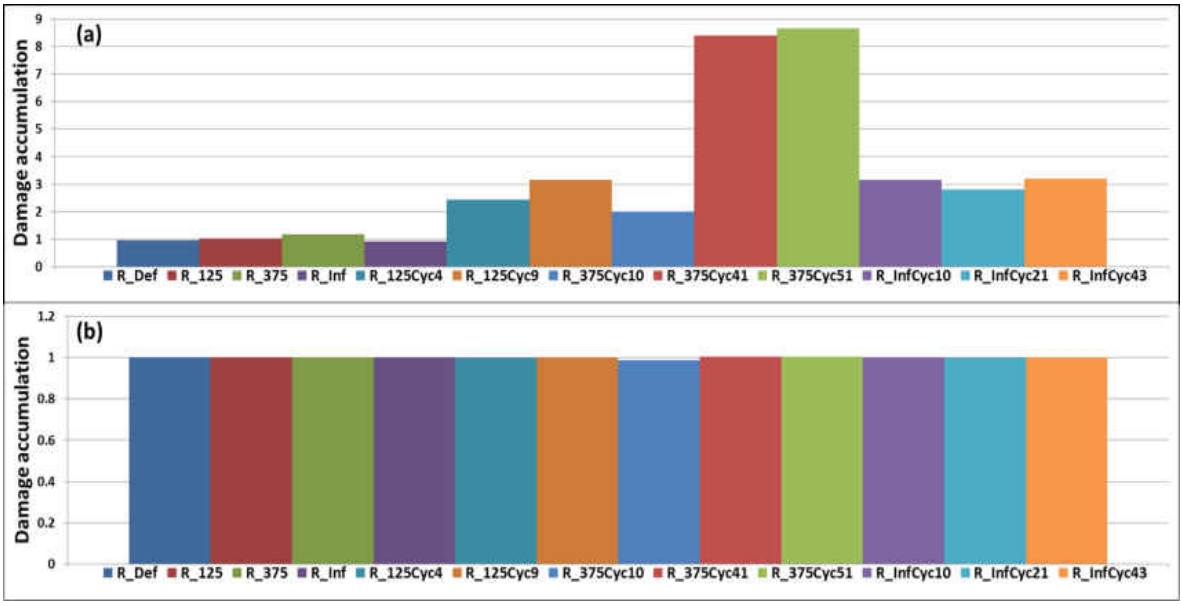

Figure 56: A comparison of damage accumulation for ELCF with (a) linear damage evolution law (Eq.(139)) and (b) nonlinear damage evolution law (Eq. (140)). The damage accumulation of (b) is close to unity for all tests of ELCF after adopting the extension functions of damage evolution law.

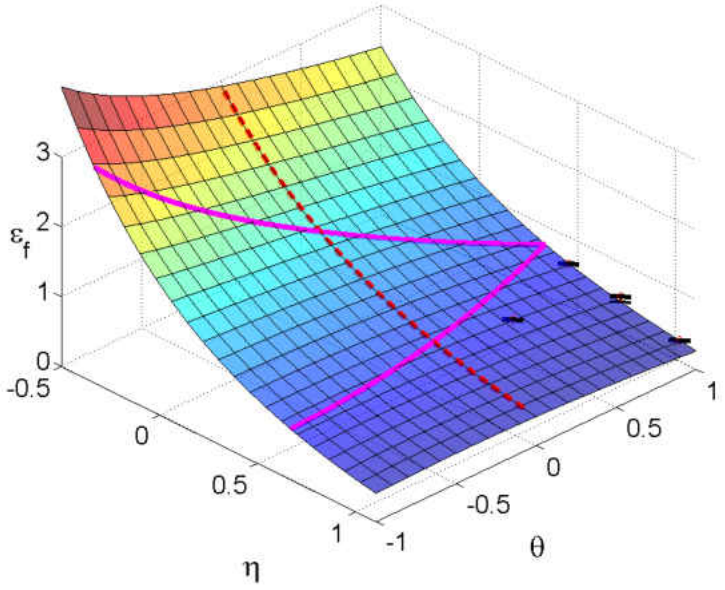

Figure 57: The calibrated 3D fracture locus of IN718 superalloy for ductile fracture tests [225].

Table 20: List of material ductile fracture parameters used in the MMC criterion

$\mathbf{c_1}$	$\mathbf{c_2}$ (MPa)	$\tilde{c}_{\theta}^{s}$	$\mathbf{c_{\theta}^{ax}}$	A	N	D_c	w
0.05896	764.588 MPa	0.86276	1	1480	0.0813	1.03	6

Table 21: List of material non-proportional parameters used for the two extended functions.

c_g	c_h	β_1	β_2	k
-6.0	3	0.05	0.00001	-1

5.8 Experimental and Numerical Simulations Results

In this section, results from tests and finite element simulations (using Abaqus/Explicit with material user subroutine VUMAT) are presented together for a direct comparison. The detail constitutive/ductile fracture models and their calibration procedures have been described in section 5.6 and 5.7.

5.8.1 Comparison of plasticity and fracture results

The three round specimens ("R0", "R1", and "R2") were simulated in Abaqus using quarter models due to symmetric conditions, and 4-node axisymmetric elements (CAX4R) were used. The 2D quarter model simulations help reduce the computational time. For the plane strain specimens, pure plane strain condition only exists at the central

range of the specimen due to the limitation of specimen size considering the load limit of our testing machine for this tough material. The two edge regions are closer to plane stress and uni-axial tension. Therefore, an FE model was developed using 8-node solid elements with reduced integration (C3D8R). Since the shape of the specimen is symmetric, a quarter model of the specimen was created. The density of mesh increases in the critical area, as seen in Figure 58. The specimen deformation during the monotonic and cyclic loadings is clearly observed during the tests and FE simulations. The smooth round bar ("R0") and the two notched round bars ("R1" and "R2") exhibit localized necking before fracture initiations in their minimum diameter locations. In addition, the plane strain specimen displayed lateral deformation during tests and FE simulations. For comparison, a set of examples of the specimens' deformation during the cyclic loading are shown in Figure 59 to Figure 62.

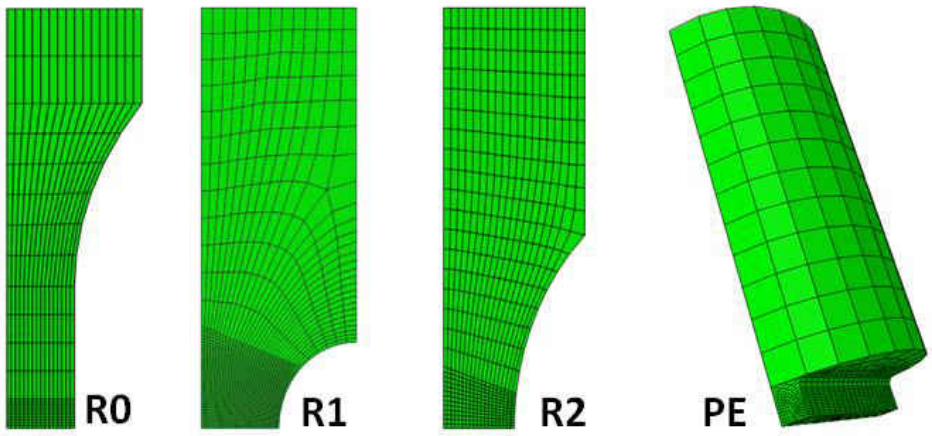

Figure 58: Meshes and different element types in Abaqus to conduct finite element simulations. The mesh density increases in the critical areas.

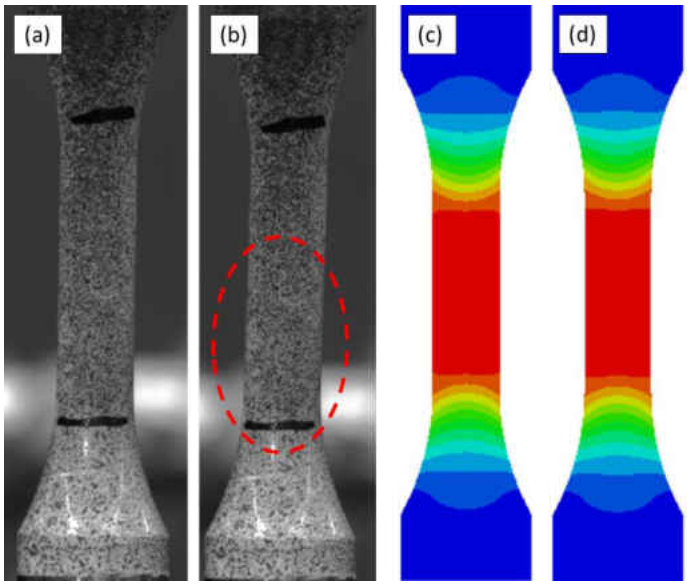

Figure 59: A comparison of the specimens' deformation during tension-compression cyclic loading for "R0" specimen. (a) Pretesting condition. (b) Specimens' buckling during compression. Note that ELCF of "R0" specimens are not available due to some buckling observed in compression. (c) Cross-section of FE simulation under tension. (d) Cross-section of FE simulation under compression. The contour plot shows the areas of high accumulation damage (D).

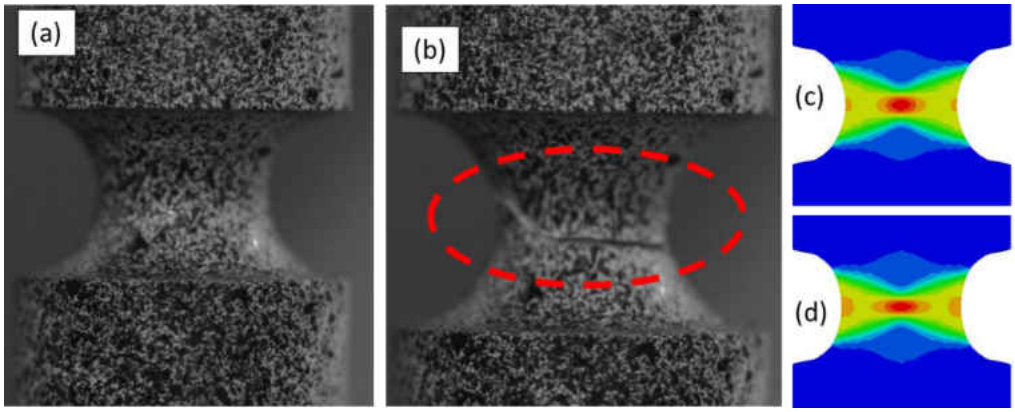

Figure 60: A comparison of the specimens' deformation during tension-compression cyclic loading for "R1" specimen. (a) Pretesting condition. (b) Post-failure and crack

propagation. (c) Cross-section of FE simulation under tension. (d) Cross-section of FE simulation under compression. The contour plot shows high accumulation damage within the center of the necking area during ELCF.

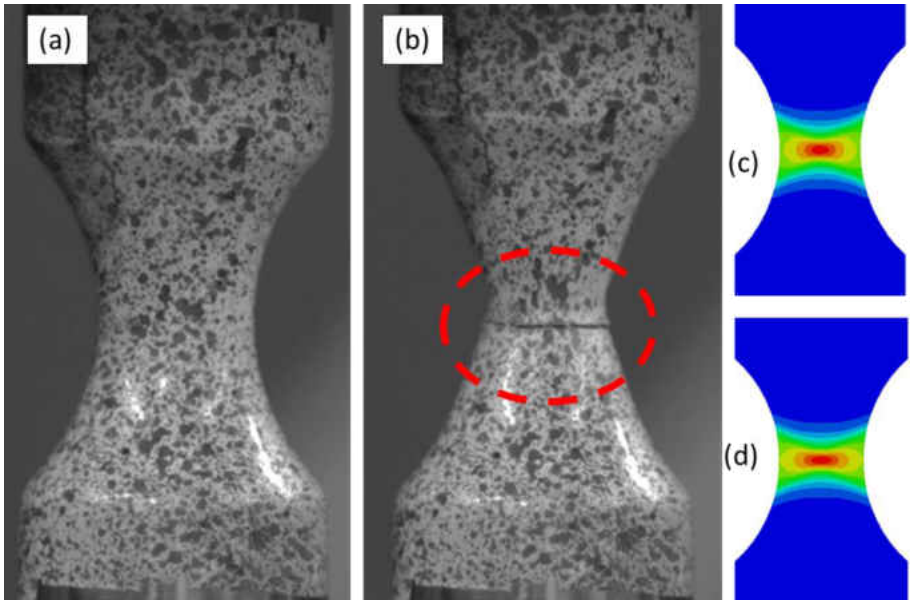

Figure 61: A comparison of the specimens' deformation during tension-compression cyclic loading for "R2" specimen. (a) Pretesting condition. (b) Post-failure and crack propagation. (c) Cross-section of FE simulation under tension. (d) Cross-section of FE simulation under compression. The contour plot shows high accumulation damage within the center of the necking area during ELCF.

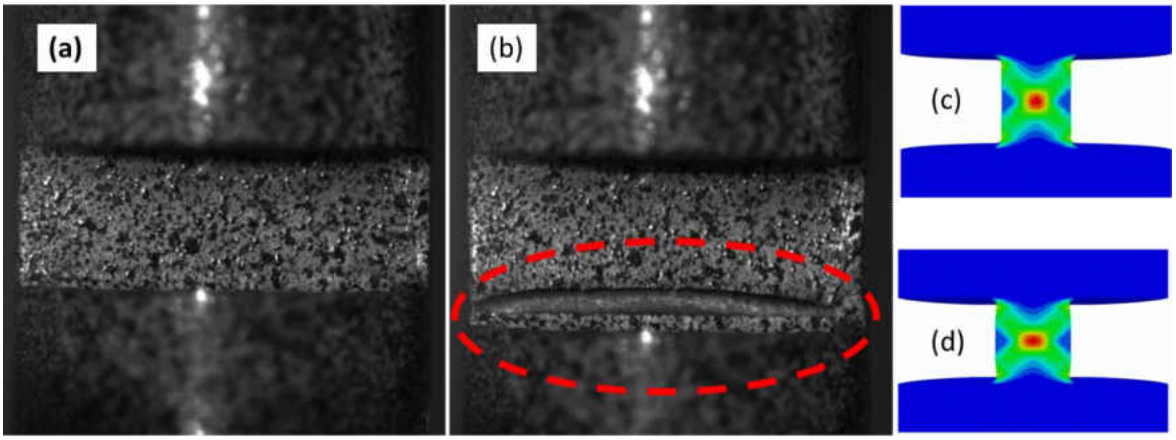

Figure 62: A comparison of the specimens' deformation during tension-compression cyclic loading for "PE" specimen. (a) Pretesting condition. (b) Post-failure and crack propagation. (c) Cross-section of FE simulation under tension. (d) Cross-section of FE simulation under compression. The contour plot shows high accumulation damage within the center area during ELCF.

The validity of the plasticity and ductile fracture models was assessed by comparing the finite element simulations with the experimental results for all tested cases. The numerical vs. experimental force-displacement curves for each case of monotonic and cyclic loading are illustrated in Figure 63 to Figure 66. Very good correlations are achieved for all the monotonic and cyclic loading force-displacement curves.

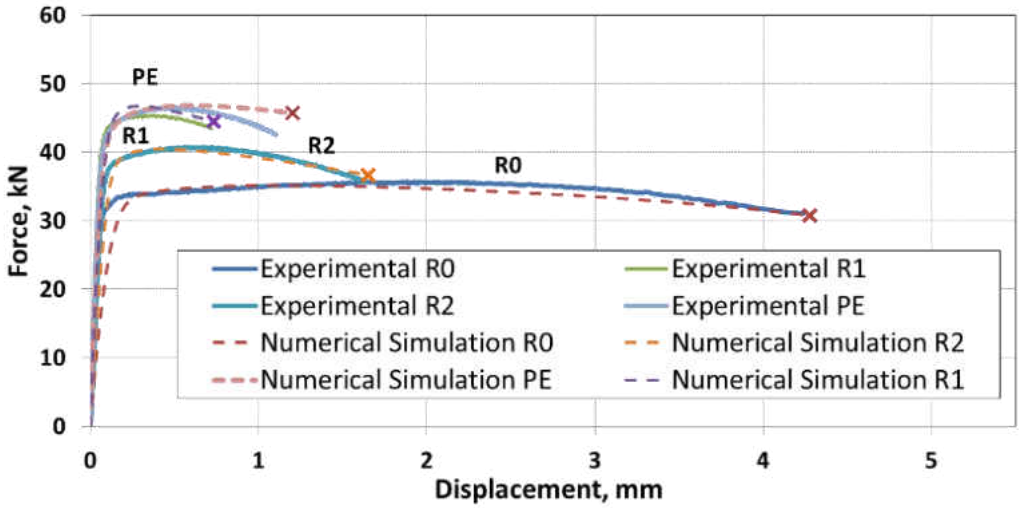

Figure 63: A comparison of the numerical and experimental results of the monotonic loading along with the fracture occurrence for all four specimens shows good correlation.

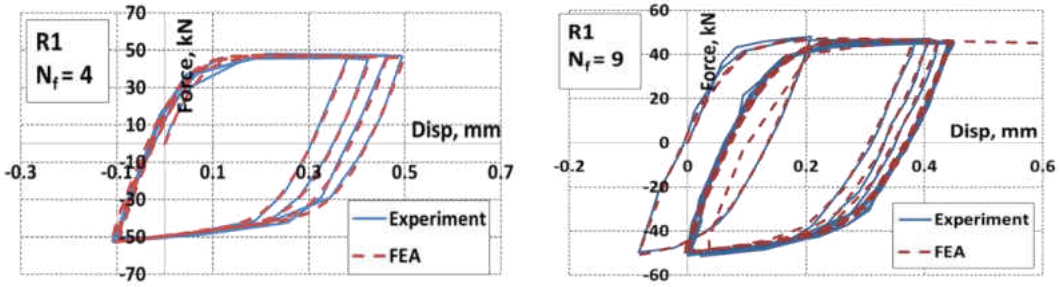

Figure 64: A comparison of force-displacement loops for the sharp notch specimens ("R1") which failed after 4 cycles (*left*) and 9 cycles (*right*).

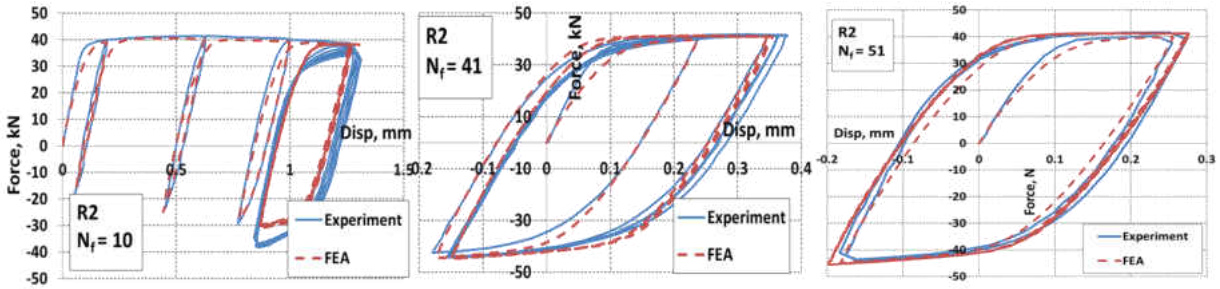

Figure 65: A comparison of force-displacement loops for the large notch specimens ("R2") which failed after 10 cycles (*left*), 41 cycles (*middle*) and 51 cycles (*right*).

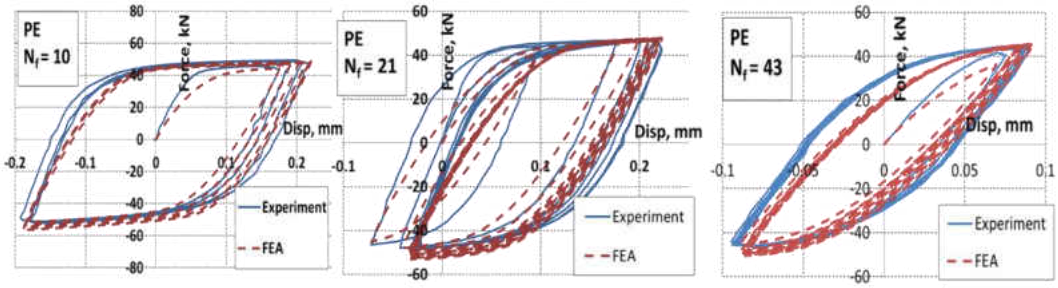

Figure 66: comparison of force-displacement loops for the plane strain specimens ("PE") which failed after 10 cycles (*left*), 21 cycles (*middle*) and 43 cycles (*right*).

On the other hand, the behaviors of the damage evolution for all the tests are simulated and portrayed in Figure 67. It is seen that the damage accumulation increment develops rapidly as the loading process starts and then it decelerates significantly as the equivalent plastic strain increases. The damage accumulation (D) increment decelerates dramatically after a few cycles of the loading and reaches a stable minimal increment as D approaches unity. The assumption asserts that the experimental fracture initiation onsets at D = 1.

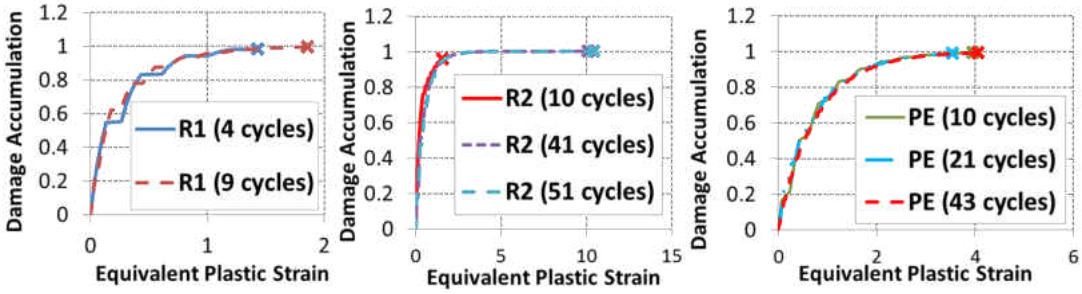

Figure 67: The damage evolutions for "R1", "R2", and "PE" specimens, respectively.

5.8.2 FE simulation of ELCF crack propagation and crack modes

This section aims to provide a method to predict crack initiation and propagation under ELCF based on the proposed fracture model (Eq. (140)). Conventional finite

element simulations typically predict a flat fracture surface that is perpendicular to the load direction. In contrast, the experimental results show that crack propagated along a developed shear band with the least energy dissipation [98, 176]. The numerical simulation of crack initiation and propagation in IN718 under monotonic loading has been achieved in the parallel paper [225]. The test results of the monotonic loading show that all three round bar specimens (‘‘R0”, ‘‘R1”, and ‘‘R2”) exhibit vivid necking with a cup-cone fracture mode. The ductile fracture starts with micro cracks that occurs in the necked center and followed by crack propagation towards the outer radius. Then, a shear lip was formed at the circumferential edge of the outer radius (which is actually close to plane strain condition). This creates a cup-cone fracture mode. On the other hand, the plane strain specimen under monotonic loading (‘‘PE”) shows a slant fracture mode, which was caused by a shear band generated in the gauge section.

Similarly to ductile fractures under monotonic loading, ELCF undergoes extremely large plastic strain before fracture. However, ELCF involves cycling load as well as extremely large plastic strain accumulation. Therefore, two different damage mechanisms are involved in the ELCF failure process: ductile fracture and fatigue mechanisms. Many researches [36, 183, 185], including this paper, found that the ductile fracture mechanism takes the dominant role in ELCF failures. This is evident form the tested material’s fracture surface feature where cracks initiated in the gauge center and propagated outwards, which was identical to that of the monotonic loading tests. The comparison fractographies in Figure 77 between monotonic loading and ELCF are very clear to study the underlying fracture mechanism. For the round bar cases, a clear cup-

cone fracture mode occurs for both loading conditions. Similarly, a slant fracture mode appears in the plain strain specimens for both loading conditions. It is potentially concluded that the underlying fracture mechanism in ELCF is the ductile fracture, which is controlled by the internal crack initiation, propagation and coalescence.

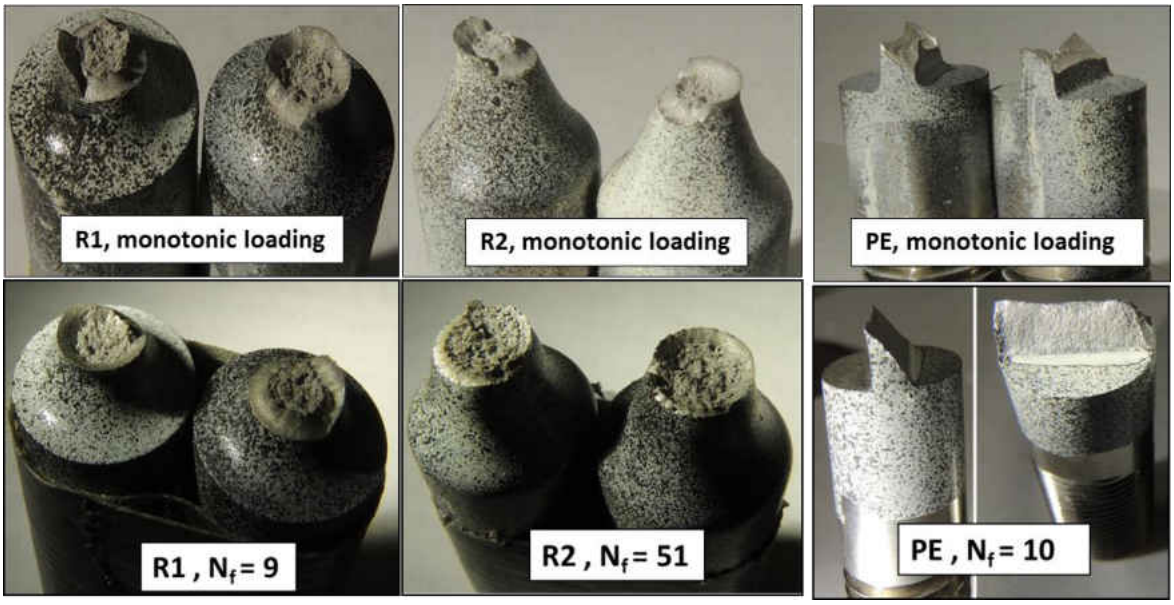

Figure 68: A comparison between the fracture modes of ductile fracture under monotonic loading (upper row) and the ELCF (lower row). Similar fracture modes are observed.

The method of simulating the fracture modes will be described in this paragraph. The damage accumulation indicator D starts from zero (material assumed virgin) and evolves (based on Eq. (140)) as the equivalent plastic strain accumulation increases during the cyclic loading. The D continues to evolve until it reaches unity. Once the damage accumulation indicator D equals to unity, which is after fatigue failure initiation, the parameter c_g in Eq. (141) changes its value to 0.001 in order to increase the damage accumulation indicator D rapidly and linearly to reach the value of D_c. An illustration of the D evolution throughout the loading process until fracture is shown in Figure 69.

Accordingly, a complete deletion of material points happens when $D = D_c$, after which, the material element shows no resistance to load. In other words, the parameter D_c is the value of the damage indicator when an integration point of an element in the Abaqus/Explicit user defined material subroutines will be deleted and show zero resistance to load. It is found that this modification of parameter c_g in Eq. (141) is essential to simulate the fracture modes under ELCF. The sudden fracture initiation and propagation for all specimens, caused by the jump of c_g, causes a quick load drop in the force–displacement curves. In reality, many local phenomena happened within this short increment of displacement.

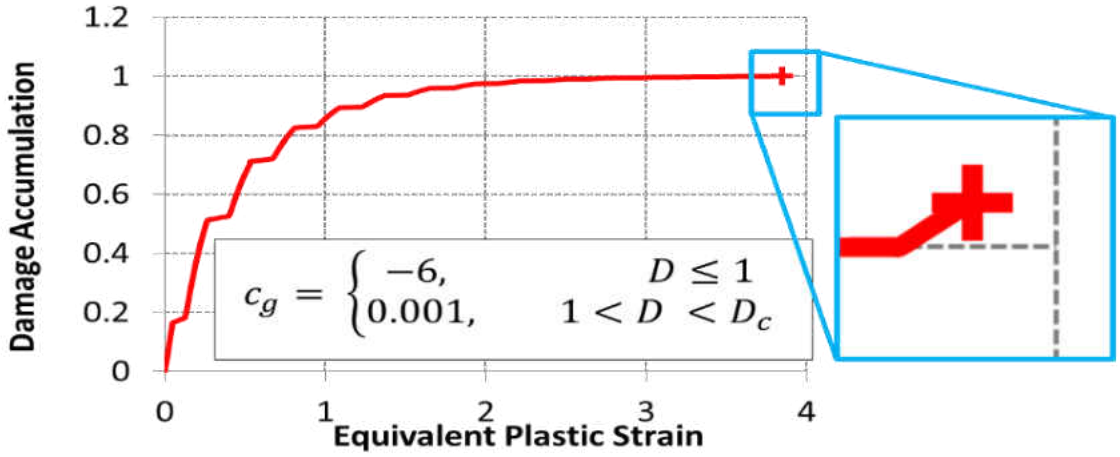

Figure 69: An illustration of the damage evolution before D = 1 and the sudden jump of the damage evolution after D =1. The zoom-in view at the end of the damage evolution path shows this change.

Finally, the predicted fracture modes were closely correlated with test results for all specimens as illustrated in Figure 80, Figure 71, and Figure 72. The simulations of the round specimen were presented using the sweep feature in Abaqus to render a 2D axisymmetric model into a full 3D geometry. It is important to mention that fracture

simulations are sensitive to mesh size. The finer mesh size will give clearer fracture surface configurations. The used mesh size was 0.05 mm for these simulations. It is concluded that the proposed fracture model with the extension functions is capable of depicting both the fracture initiation and the fracture propagation modes for all types of specimens under large-strain cyclic loading.

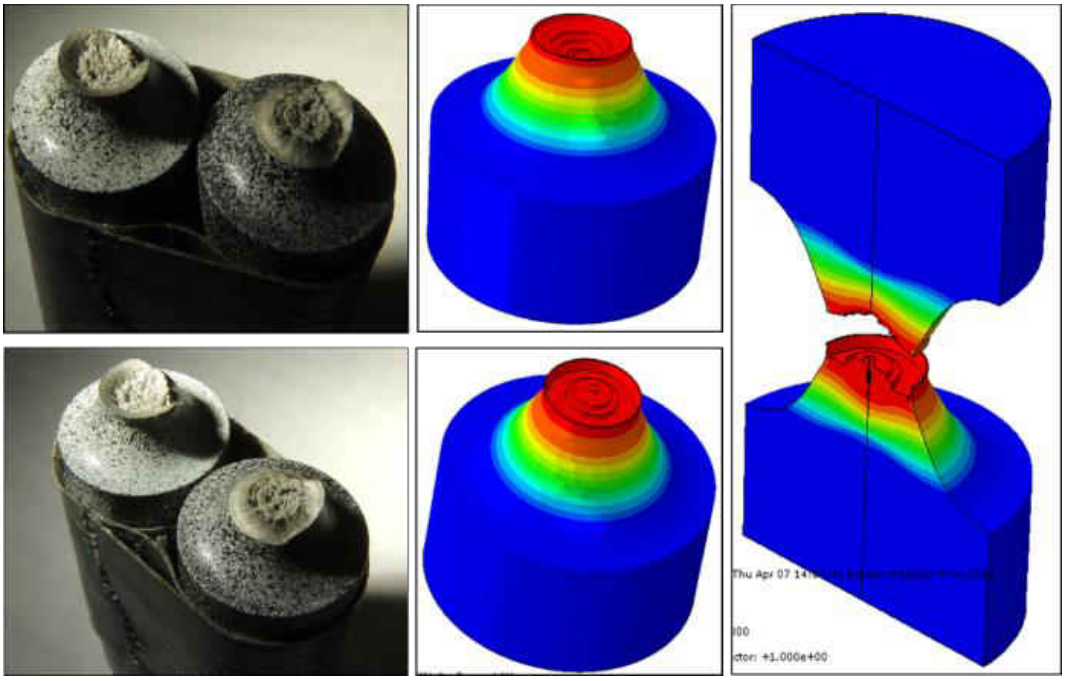

Figure 70: Numerical fracture simulation shows a cup-cone fracture pattern for the sharp notch bar specimen (‘‘R1”) under ELCF. The left figures show the experimental results. The contour plot is the damage accumulation in Abaqus.

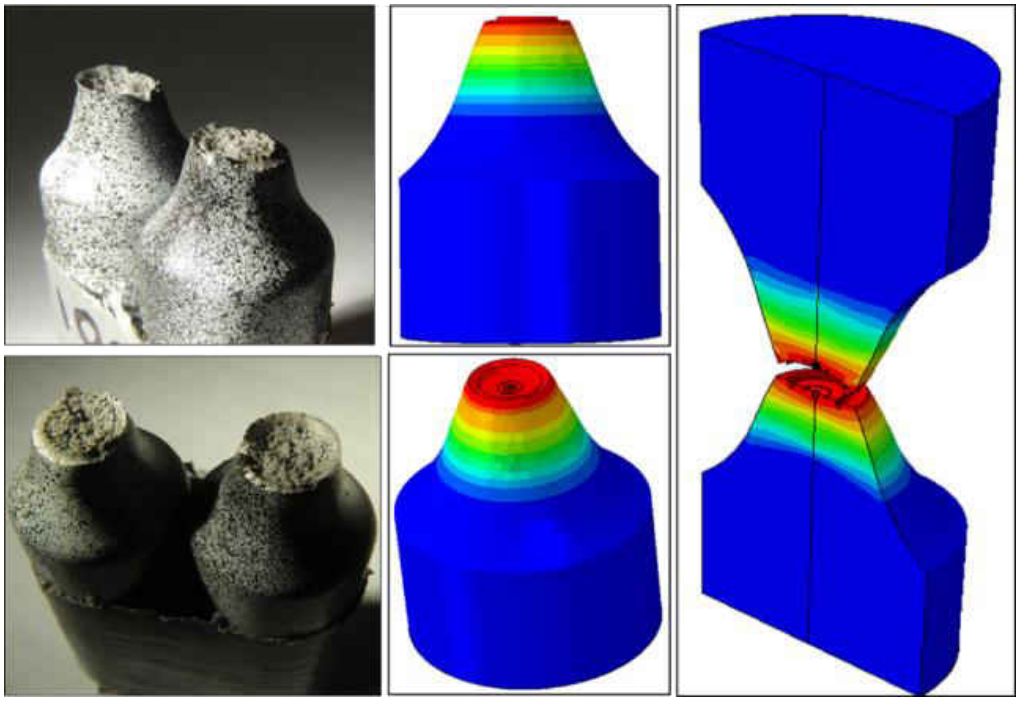

Figure 71: Numerical fracture simulation shows a cup-cone fracture pattern for the large notch bar specimen (‘‘R2”) under ELCF. The left figures show the experimental results. The contour plot is the damage accumulation in Abaqus.

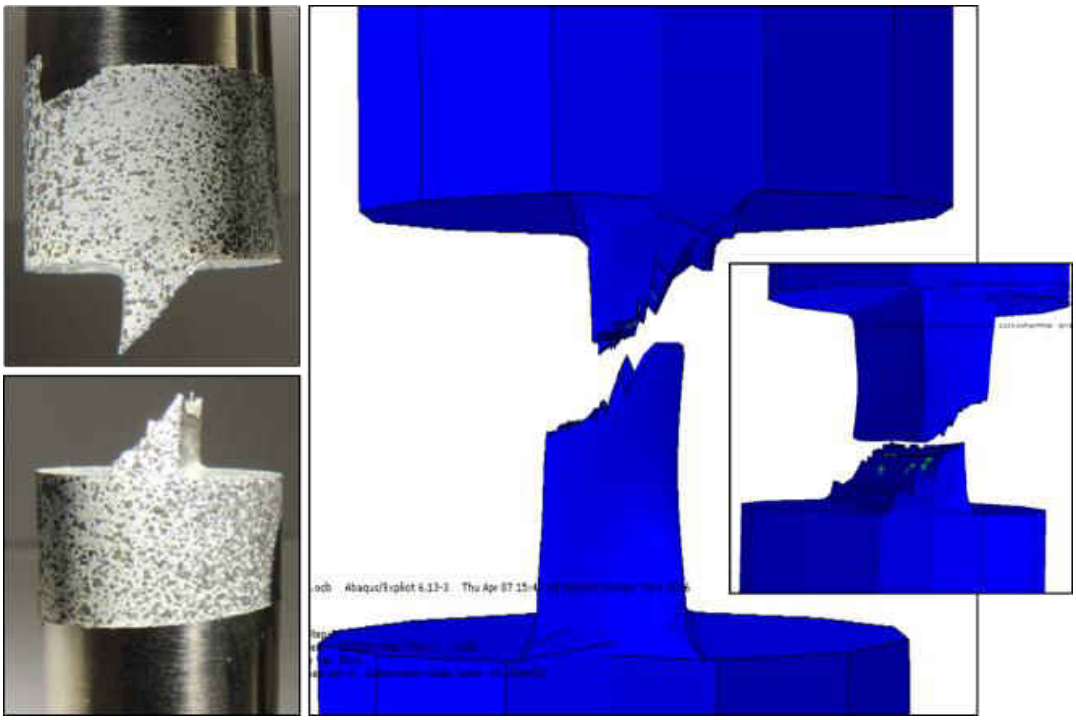

Figure 72: Numerical fracture simulation shows a slant fracture mode for the plain strain specimen (‘‘PE”) under ELCF. The left figures show the experimental results.

5.9 Error Evaluation

This paper presented studies on both ductile fracture and ELCF of IN718 superalloy. The current study demonstrates that the combined kinematic and isotropic strain hardening along with the effect of the stress triaxiality and Lode angle parameter can accurately simulates the metals’ force-displacement curves of different loading conditions and different stress states.

On the other hand, the MMC ductile fracture criterion has been validated and proven appropriate to monotonic loading conditions [225]. A suitable extension to the

MMC criterion was introduced in this paper by introducing two weighting functions to consider the nonlinearity behavior of the damage evolution and to capture the effect of the cyclic loading within the ELCF regime. The proposed fracture model considers the cyclic loading conditions as well as the monotonic loading conditions. The two extended functions are presumed to act independently and concurrently throughout a loading process.

In order to evaluate the accuracy of the proposed extension, the accumulated equivalent plastic strain ($\bar{\varepsilon}_{pl}$) at the fracture instant will be used to assess the proposed model. The ELCF initiation prediction based on the proposed model will be denoted by "Numerical $\bar{\varepsilon}_{pl}$". Similarly, $\bar{\varepsilon}_{pl}$ at the instant of the experimental ELCF is denoted by "Experimental $\bar{\varepsilon}_{pl}$". The Experimental $\bar{\varepsilon}_{pl}$ at the instant of the experimental ELCF initiation are obtained by FEA since there is no direct measure method of ($\bar{\varepsilon}_{pl}$) in the ELCF tests. The accumulated equivalent plastic strain provides a convenient measure of the step for ELCF in FEM [212, 220].

A comparison table and a plot of the predicted numerical and experimental accumulated equivalent plastic strain ($\bar{\varepsilon}_{pl}$) at fracture is shown in Table 22 and Figure 73(a). It is seen that the MMC criterion with the extension provides reasonable accuracy of the predicted $\bar{\varepsilon}_{pl}$ at fracture on IN718 under both monotonic and ELCF. For the monotonic loading tests, the comparison results show excellent prediction of the accumulated $\bar{\varepsilon}_{pl}$ at failure for all different loading and stress state cases. On the other hand, good predictions of the accumulated $\bar{\varepsilon}_{pl}$ at fracture are also seen for the cyclic

loading conditions. The data shown in Figure 73(a) indicates good model predictions when the accumulated $\bar{\varepsilon}_{pl}$ is moderately low.

As the accumulated $\bar{\varepsilon}_{pl}$ becomes greater, the proposed model predicts failure somehow earlier than the tests results. This can be seen for tests # 7 and # 8 in Table 22, and it is clearly off limits in Figure 73(a). These two testing conditions involve large number of cycles before failure, with relatively smaller strain amplitude. Thus, the under-prediction of the proposed model might be caused by a different crack or void growth/coalescence behavior in ELCF or different low-cycle fatigue mechanisms took a role in these tests. However, it can be concluded that the results of ELCF shown in Figure 73(a) is promising and capable to predict IN718 ELCF failures in various stress states.

Table 22: A summary of ductile fracture and ELCF accumulated $\bar{\varepsilon}_{pl}$ at fracture test data.

Test #	Specimen	Accumulated $\bar{\varepsilon}_{pl}$ at fracture by FEA	Accumulated $\bar{\varepsilon}_{pl}$ at fracture by Equ. (139)	Error % of Equ. (139)	Accumulated $\bar{\varepsilon}_{pl}$ at fracture by Equ. (140)	Error % of Equ. (140)
1	**R0**	0.613	0.515	19.5%	0.515	19.5%
2	**R1**	0.292	0.252	17.7%	0.252	17.7%
3	**R1**	1.431	0.414	71.1%	1.709	19.4%
4	**R1**	1.858	0.469	74.8%	1.510	18.7%
5	**R2**	0.512	0.483	11.3%	0.483	11.3%
6	**R2**	1.577	0.556	64.8%	1.808	14.6%
7	**R2**	10.124	0.776	92.3%	4.759	53.0%
8	**R2**	10.518	0.868	91.8%	4.866	53.7%
9	**PE**	0.592	0.488	17.6%	0.488	17.6%
10	**PE**	3.968	1.155	70.9%	3.549	10.6%
11	**PE**	3.542	1.179	66.7%	3.698	4.4%
12	**PE**	4.063	1.229	69.7%	3.750	7.7%

* Monotonic loading.

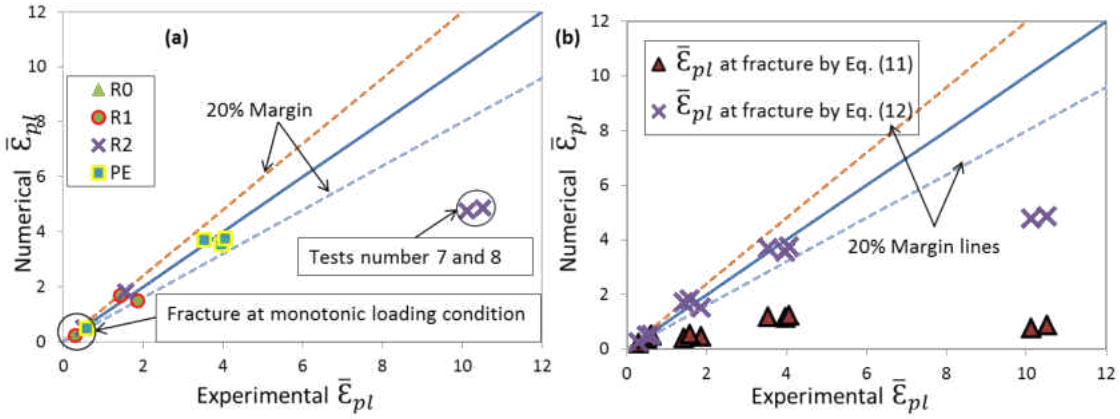

Figure 73: (a) The predicted vs. experimental accumulated equivalent plastic strains ($\bar{\varepsilon}_{pl}$) at failure for ductile fracture and ELCF, (b) A comparison between Eq. (139) and Eq. (140) on the accumulated $\bar{\varepsilon}_{pl}$ at failure for ductile fracture and ELCF.

If the extension functions in Eq. (140) are turned off (equal to Eq. (139)), the predicted accumulated equivalent plastic strain at fracture $\bar{\varepsilon}_f$ is plotted in Figure 73(b). The comparison of Eq. (139) verses Eq. (140) clearly shows that the effects of these two extension functions. The range of error of the linear damage accumulation model (Eq. (139)) is [60%, 90%], while the errors of the nonlinear model (Eq. (140)) significantly decreases to [5%, 19%].

5.10 Conclusion

This paper presented studies on both ductile fracture and ELCF of IN718 superalloy. The current study demonstrates that the combined kinematic and isotropic strain hardening along with the effect of the stress triaxiality and Lode angle parameter can accurately simulate the metals' force-displacement curves under different loading conditions and different stress states. On the other hand, the MMC ductile fracture

criterion has been validated and proven appropriate to monotonic loading conditions [225]. A suitable extension to the MMC criterion was introduced in this paper by introducing two weighting functions to consider the nonlinearity behavior of the damage evolution and to capture the effect of the cyclic loading within the ELCF regime. The proposed fracture model considers the cyclic loading conditions as well as the monotonic loading conditions. The two extended functions are presumed to act independently and concurrently throughout a loading process.

CHAPTER SIX:
EXTREMELY LOW CYCLE FATIGUE DAMAGE MECHANISM, FRACTOGRAPHIC EXAMINATION, AND LIFE PREDICTION

6.1 Abstract

The extreme high strain cyclic loading, termed extremely low cycle fatigue (ELCF), causes metals to fail in a few (less than 100) cycles. ELCF is more likely seen in heavy load machines' startup or shutdown failures and in steel-structured bridges subjected to earthquakes. This research summarizes an extensive work of experimental and numerical studies of ELCF under different stress states for Inconel 718. The modified Mohr–Coulomb (MMC) ductile fracture model, a function of stress triaxiality and Lode angle parameter, is adopted with an adequate new extension that aims to capture ELCF. A new parameter is introduced to the damage accumulation rule to represent the effect of the cyclic loading. The model explores the underlying damage and fracture mechanisms through the equivalent plastic strain evolution. The ELCF damage and fracture mechanisms are implemented into finite element analysis (FEA). Finally, fractographic examinations, analysis, and finite element simulations are presented with good correlation.

6.2 Introduction

The ELCF regime falls in between the ductile fracture due to monotonic loading and the Low cycle fatigue (LCF). The term ELCF describes high strain amplitude cyclic

loading that causes metals to fail under 100 cycles of reverse loading ($N_f < 100$) [226]. Failures due to ELCF are seen commonly in real applications, for example, steel structures under seismic loading, gas turbine under high-pressure air current, start-up or shutdown of power generators and compressors, and offshore platforms and ships under wave loading are ELCF real life examples. LCF regime has been extensively studied and well described by the strain-based Coffin-Manson law, which is subjected to moderate plastic strain amplitudes. However, Coffin-Manson law tends to over-predict the metal's life in ELCF regime due to the considerably very-large strain amplitude cyclic loading [35]. Primarily, the classical approaches of the direct strain–based fatigue models cannot model ELCF due to the accompanied large-scale yielding physical processes that are responsible for this type of fracture. Secondly, large strain amplitude cyclic loading histories randomly vary, and so, it is difficult to count the cycles in a real life situation. Thirdly, classical strain-based fatigue damage models (i.e. ΔK type) presume the existence of sharp crack or defect, which is missing in most real application details [212]. These limitations make the need of studying ELCF by a new approach be essential to understand and improve the metal's performance and life span in engineering structures and components. As a result, the similarities between the ductile fracture under monotonic loading and ELCF regarding very large accumulated plastic strain, very short life, and crack topologies reveal that extending ductile fracture models to the case of ELCF, under different stress states, merits extensive consideration.

6.3 Characterization of Stress States

This section describes the approach of investigating metals' sensitivity to arbitrary stress states by using two dimensionless parameters: stress triaxiality (η) and Lode angle (θ). These parameters are used to study the metal's plasticity and ductile fracture dependency on stress states. The three principle stresses are denoted by σ_1, σ_2, and σ_3. Stress triaxiality (η) is a dimensionless hydrostatic pressure defined by Eq. (147). The Lode angle (θ) is defined on the deviatoric plane (or π-plane), and it is known as the angle between the stress tensor that passes through the deviatoric plane and the axis of the principal stresses. The range of the Lode angle is $0 \leq \theta \leq \pi/3$ and consequently, the range of ξ (defined in Eq. (148)) is $-1 \leq \xi \leq 1$. Thus, the Lode angle can also be normalized and known as the normalized Lode angle or Lode angle parameter ($\bar{\theta}$), as seen in Eq. (148) [225].

$$\eta = \frac{\sigma_m}{\bar{\sigma}}, \quad q = \bar{\sigma} = \sqrt{3J_2} = \sqrt{\frac{1}{2}[(\sigma_1 - \sigma_2)^2 + (\sigma_2 - \sigma_3)^2 + (\sigma_3 - \sigma_1)^2]} \tag{147}$$

$$\xi = \left(\frac{r}{q}\right)^3 = \cos(3\theta), r = \left[\frac{27}{2}(\sigma_1 - \sigma_m)(\sigma_2 - \sigma_m)(\sigma_3 - \sigma_m)\right]^{1/3}, \bar{\theta} = 1 - \frac{6\theta}{\pi} \tag{148}$$

6.4 Design of Specimen Geometries

In this study, a number of specimens, having four different shapes, were tested under high strain cyclic loading of tension and compression. The four distinctive shapes are a smooth round bar, a round bar with a small external circular notch, a round bar with a large external circular notch, and a flat plane strain bar. Three-dimension (3D) sketches and information about detailed dimensions are demonstrated in Figure 74. These different

geometries are designed in a way to ensure fracture initiation at desired stress states. To easily distinguish each specimen, Table 23 explains the denotation used from now on.

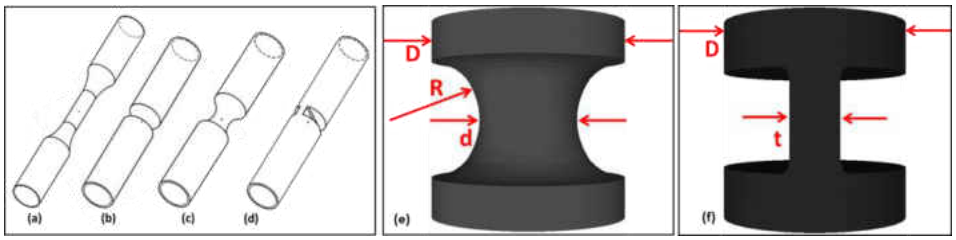

Figure 74: A 3D sketch of (a) smooth round bar, (b) small radius notch bar, (c) large radius notch bar, and (d) plane strain flat bar, (e) & (f) express main dimensions of the tested specimens.

Table 23: Denotation of sample names with their key dimensions (units: mm)

Specimen type	Denotation	Notch radius, (R)	Minimum diameter, (d) or thickness (t)	Shoulder diameter, D
(a) Smooth round bar	**R0**	∞	6.350	12.700
(b) Small radius notched bar	**R1**	3.175	6.350	12.700
(c) Large radius notched bar	**R2**	9.525	6.350	12.700
(d) Plane strain	**PE**	∞	t = 3.048	12.700

6.5 Experiments

The tested metal was Inconel 718 (Nickel-base superalloy), which is widely used in hot section parts of gas turbine engines due to its superb high strength, ductility and fatigue properties at high and cryogenic temperatures. ELCF test series were run until complete fracture of the specimen under different high strain amplitudes, and numbers of

cycles to failure (N_f) are shown in Table 24. Some of the specimen's fractured surfaces morphologies are shown in Figure 75. The experimental strain-life results in ELCF domain (Figure 75) reveal a strong dependency of the fracture strain on stress triaxiality. Hence, we can affirm from the ELCF experimental results that the strain–life curve slope is inversely proportional to the stress triaxiality. The measured force-displacement curves of the cyclic loading are recorded and illustrated in Figure 76.

Table 24: Experimental data and measurements of the ELCF tests of IN718.

Test number	Specimen	N_f	Test number	Specimen	N_f
1	R1	4	5	PE	43
2	R1	9	**6**	R2	10
3	PE	10	**7**	R2	41
4	PE	21	**8**	R2	51

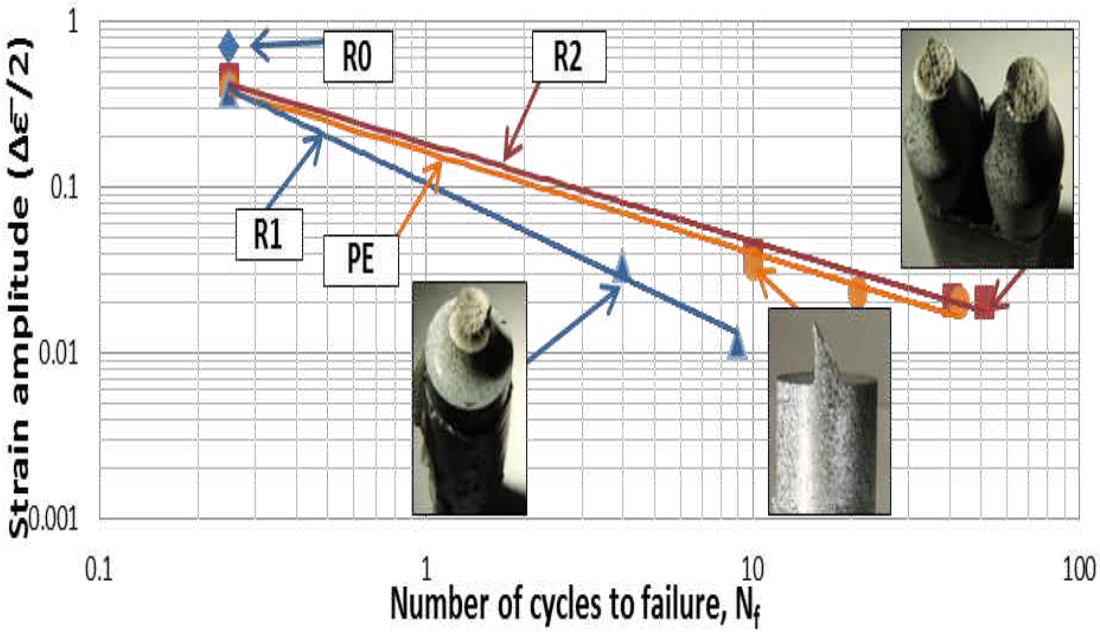

Figure 75: Strain–life curves for all specimens under ELCF with some examples of the specimens' fractured surfaces morphologies.

6.6 Constitutive Plasticity Modeling and Calibration

6.6.1 Plasticity Model with a Combined Hardening Rule

The plasticity behavior of IN718 under pull-push cyclic loading paths is assumed to involve a combined hardening rule: kinematic hardening and isotropic hardening. The Bauschinger effect was expressed by Chaboche's nonlinear model and the isotropic hardening model was described by Voce model in Eqs. (149). Moreover, the Bai-Wierzbicki plasticity model (Eq. (150)) was adopted to incorporate the effects of different stress states. . It should be noted that the term of $\left[1 - c_\eta \left(\eta - \eta_o\right)\right]$ should be bounded within certain limits for the very high or very low stress triaxiality region. For example, $0.5 \leq \left[1 - c_\eta \left(\eta - \eta_o\right)\right] \leq 2.0$ was used in our simulations. Readers are advised to Refs. [4, 219, 225] for more model details.

$$\dot{\alpha}_i = C_i \dot{\varepsilon}^{pl} - B_i \alpha_i \dot{p} \;;\; \alpha = \sum_{i=1}^{3} \dot{\alpha}_i \;,\; \sigma\left(\bar{\varepsilon}_{pl}\right) = \sigma_y + Q\left(1 - e^{-b\bar{\varepsilon}_{pl}}\right) \tag{149}$$

$$\sigma\left(\varepsilon_{pl}, \eta, \theta\right) = \sigma\left(\bar{\varepsilon}_{pl}\right)\left[1 - c_\eta \left(\eta - \eta_o\right)\right]\left[c_\theta^s + \left(c_\theta^{ax} - c_\theta^s\right)\left(\frac{m+1}{m}\right)\left(\gamma - \frac{\gamma^{m+1}}{m+1}\right)\right] \tag{150}$$

6.6.2 Ductile Fracture Criterion

The modified Mohr-Coulomb (MMC) ductile fracture locus (Eq.(151)) was applied in this study. This model was extended with post-failure behaviors to predict crack initiation and growth under different stress states of IN718 [225]. The MMC model was also extended in this paper to consider ELCF regime by introducing two independent and

concurrent functions, $g(D)$ and $h(D,\mu)$ in the damage evolution rule (Eq. (152)). The first function, $g(D) = \left(c_g D + \frac{c_g}{e^{c_g}-1}\right)$, controls the nonlinearity of the damage evolution under monotonic loadings. The second function, $h(D,\mu) = \left(1 + c_h D^{\beta_1}\mu^{\beta_2}\right)^k$, incorporates the effect of the cyclic loading in ELCF through considering by the loading direction change between the current stress and the backstress tensors. Readers are advised to read Refs. [25, 219] for more descriptive model details. The damage indicator D range is [0, 1], where $D = 0$ represents a virgin metal (flawless) and $D = 1$ represents fracture initiation.

$$\bar{\varepsilon}_f(\eta,\bar{\theta}) = \left\{ \begin{array}{l} \frac{A}{c_2} \times \left[\tilde{c}_\theta^s + \frac{\sqrt{3}}{2-\sqrt{3}}(\tilde{\mathbf{c}}_\theta^{\mathbf{ax}} - \tilde{c}_\theta^s)\left(\mathbf{sec}\left(\frac{\bar{\theta}\pi}{6}\right) - \mathbf{1}\right)\right] \\ \quad \times \left[\sqrt{\frac{1+c_1^2}{3}}\ \mathbf{cos}\left(\frac{\bar{\theta}\pi}{6}\right) + \mathbf{c_1}\left(\eta + \frac{1}{3}\ \mathbf{sin}\left(\frac{\bar{\theta}\pi}{6}\right)\right)\right] \end{array} \right\}^{-1/N} \quad (151)$$

$$D = D\left(\bar{\varepsilon}_{pl}\right) = \int_0^{\bar{\varepsilon}_{pl}} g(D).\ h(D,\mu)\ \frac{d\bar{\varepsilon}_{pl}}{\bar{\varepsilon}_f(\eta,\bar{\theta})} \quad (152)$$

6.6.3 Model Calibration and Finite Element Simulation

The proposed plasticity and fracture model for ELCF are validated by comparing the numerical simulation results (using Abaqus/Explicit) to the experimental results. Very well correlations are achieved for all loading cases in terms of force-displacement curves (Figure 76). The same MMC ductile fracture model parameters have been calibrated under monotonic loading and extensively explained in a parallel paper [225]. The extension functions were calibrated under cyclic loading conditions. A Matlab code was created to run the damage evolution integration, as in Eq. (152), to get the best estimation

of the five model parameters so that the calculated damage accumulation (D) for all the cases is close to unity, where the ELCF is predicted.

Table 25: List of material parameters of the combined hardening rule and the plasticity model.

C_1 (MPa)	B_1	C_2 (MPa)	B_2	C_3 (MPa)	B_3	c_θ^{ax}
310000	355	240000	1999	900	0	1
σ_y (MPa)	**Q (MPa)**	**b**	**c_η**	**η_o**	**c_θ^s**	**m**
45.1	100.4	35.425	0.40	0.333	0.866	0.75

Table 26: List of material ductile fracture parameters used in the MMC criterion

c_1	c_2 (MPa)	$\tilde{c}_\theta^s$	c_θ^{ax}	A	N	c_g	c_h	β_1	β_2	k
0.05896	764.588	0.86276	1	1480	0.0813	-6.0	3	0.05	0.00001	-1

6.7 ELCF Damage Mechanism and Fractography

The short fatigue life in ELCF is a result of the "fracture mode transition" from LCF to ELCF, where the damage evolution mechanism varies. The fracture mode transition is due to the crack initiation transition from the specimen's surface in LCF regime to the inside of the specimen in ELCF regime. The ELCF regime exhibits large plastic strain accumulation while LCF regime exhibits considerably lesser plastic strain accumulation. The fatigue damage in ELCF is dominated by the enormously high level of plastic strain that causes huge ductility exhaustion within the metal. This huge ductility exhaustion leads the metal to fail in a very short time during the cyclic loading process.

This is mainly presumed as the reason for the short fatigue life in ELCF. On the other hand, the low levels of plastic strain in LCF causes the fatigue damage to be dominated by crack propagation resulting in higher fatigue life.

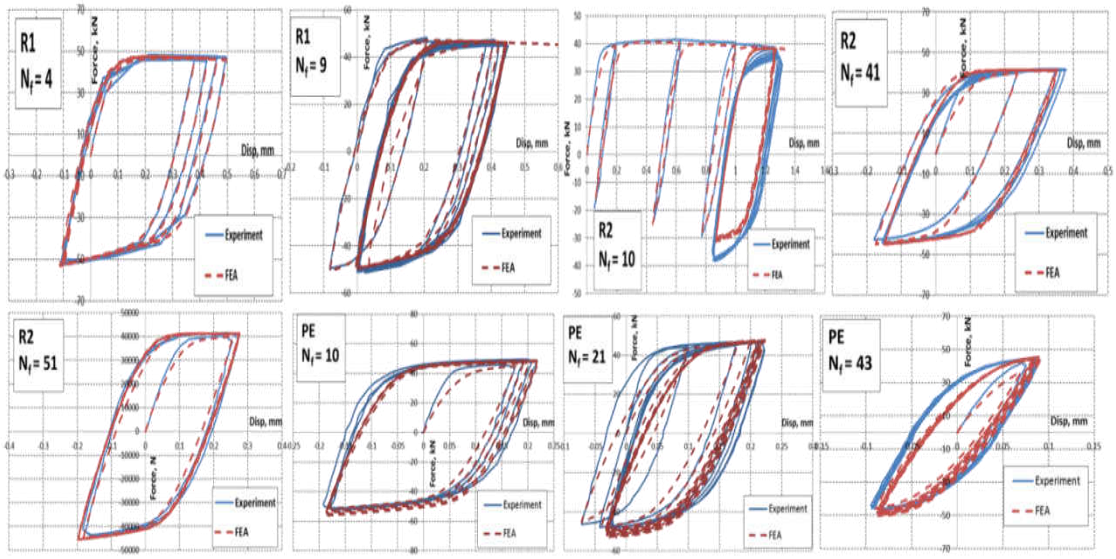

Figure 76: A comparison of force-displacement hysteresis loops for all tests. The blue solid curves are the experimental results, and the red dashed curves are the FE simulations.

Some experimentally fractured specimens under ELCF are shown earlier in Figure 75. Fatigue cracks in ELCF tended to initiate in the gauge center and then propagate towards the surface. The round bars specimens (R1, R2) exhibits cup-cone fracture mode. The cup-cone fracture mode starts with micro cracks in the gauge center followed by crack propagation towards the outer radius. Then, a shear lip is formed at the circumferential edge of the outer radius (which is close to plane strain condition). On the other hand, the plane strain specimens (PE) show a slant fracture mode, which was caused by a shear band generated in the gauge section. It is evident from the fracture

surface morphologies of each specimen that the fracture mechanism is very similar to that of the ductile fracture under monotonic loading as shown in Figure 77.

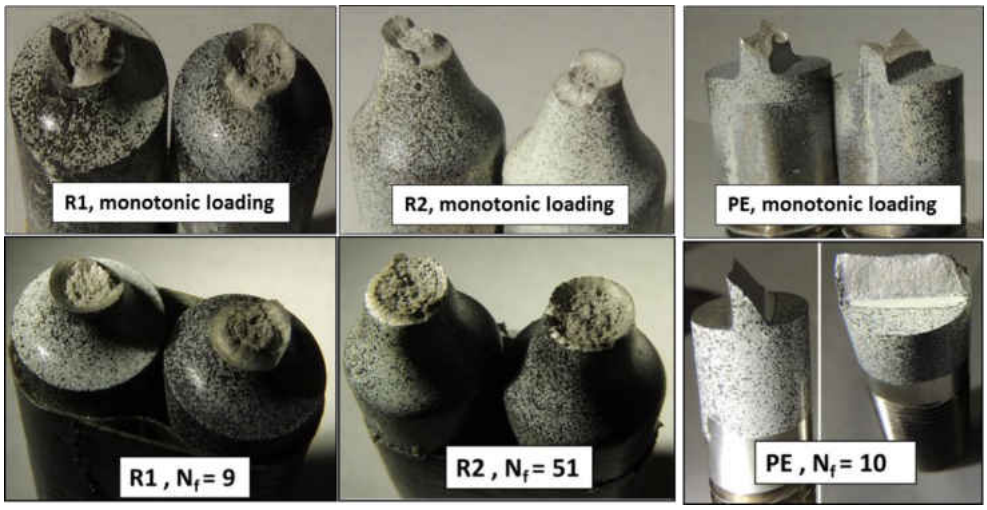

Figure 77: A comparison between the fracture modes of ductile fracture under monotonic loading (*upper row*) and the ELCF (*lower row*). The comparison shows similar fracture modes.

Similar to ductile fractures under monotonic loading, ELCF undergoes extremely large plastic strain before fracture. However, ELCF involves cycling loads as well as extremely large plastic strain accumulation. Therefore, two different damage mechanisms are involved in the ELCF failure process: ductile fracture mechanism and fatigue mechanisms. Many researches [36, 183, 185, 220], including this paper, found that the ductile fracture mechanism takes the dominant role in ELCF failure. This is evident form the tested material's fracture surface feature where cracks initiated in the gauge center and propagated outwards, which was identical to that of the monotonic loading tests. The comparison fractographic in Figure 77 between monotonic loading and ELCF are very helpful to study the underlying fracture mechanisms. It is potentially concluded that the

underlying fracture mechanism in ELCF is dominated by the ductile fracture. Finally, the behaviors of the damage evolution for all the tests series are simulated and tracked in Figure 78 using Eqs. (151) & (152). It is seen that the damage accumulation increment develops rapidly as the loading process starts. Then, the damage accumulation increment decelerates dramatically after few cycles of the loading. The increment of damage accumulation indicator, D, reaches a stable minimal around D equals unity, which is when the fracture initiates. This damage accumulation describes the huge microstructure evolution, ductility exhaustion, cyclic hardening/softening, and fracture mechanism during ELCF.

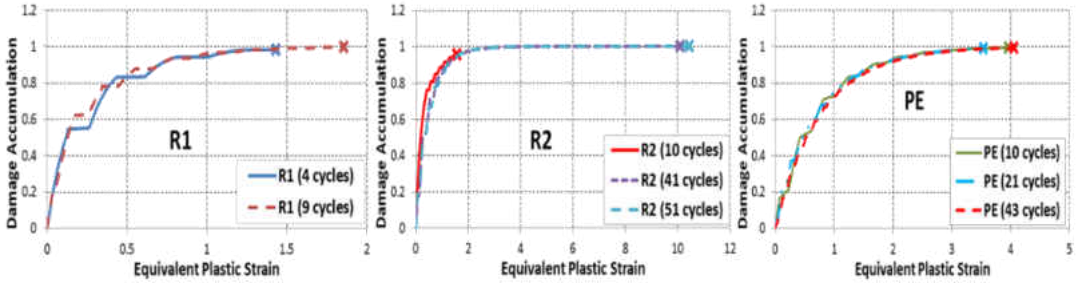

Figure 78: The damage accumulation for "R1", "R2", and "PE" specimens under ELCF.

Finally, the predicted fracture modes in FEA were closely correlated with test results for all specimens as illustrated in Figure 80. It is noteworthy that fracture simulation is very mesh-sensitive. It is concluded that the MMC fracture criterion, along with the proposed damage accumulation functions, is capable of depicting both the fracture initiation and the fracture propagation modes for all types of specimens in the ELCF domain.

6.8 ELCF Life Prediction

The previous comparison between ductile fracture due to monotonic loading and ELCF shows various similarities in the fracture modes. However, fatigue studies indicate that complicated underlying fracture mechanisms occur under fatigue failures. The MMC model with the suitable extension identifies the complicated underlying fracture mechanisms within ELCF. It also quantifies the ELCF phenomena based on crack initiation, growth, and coalescence along with damage accumulation. Such a model will promote the understanding of ELCF fracture mechanisms and will simulate the complicated mixed fracture phenomena by FEA. The MMC model with the cyclic effect extension simulates the ELCF using four parameters ($\bar{\varepsilon}_{pl}, \eta, \bar{\theta}, \mu$) to describe the complicated underlying fracture mechanisms. All these parameters are obtained from FEA at the central element of the bar specimens during reverse loadings. The accumulated equivalent plastic strain (EQPS), $\bar{\varepsilon}_{pl}$, is the key quantity parameter in predicting ELCF life, yet it cannot solely predict ELCF life. Thus, the reverse cycles of positive and negative stress triaxiality, η, and Lode angle, $\bar{\theta}$, in Figure 79(b) during ELCF take an important role in tracking the right accumulated EQPS in FEA. The cyclic parameter, μ, incorporates the cyclic loading effect on the damage accumulation. During the cycling loading, the damage accumulates until it equals to unity, where ELCF is predicted by fracture initiation. The accuracy assessment of the MMC model with extension is quantified by the accumulated EQPS at the failure instants. For comparison purposes, the ELCF initiation prediction based on the MMC criterion with extension will be denoted by Numerical EQPS. Likewise, EQPS at the instant of the experimental ELCF

(obtained by FEA) is denoted by Experimental EQPS. This approach provides a convenient measure that can be seen in Figure 79 for all different stress states, different strain amplitudes, and different loading conditions. Overall, the results of the ELCF prediction by MMC model with extension shows good accuracy, within the range of 20%. The MMC model with extension is shown capable of predicting failures due to both monotonic loading and ELCF. However, two data points of "R2" specimen in (test data 7 & 8) are clearly off the ELCF prediction range. The ELCF prediction for these two tests is fairly sooner than the experimental results. This discrepancy is seen when the EQPS is somewhat large. Moreover, these data points correspond to a relatively larger number of cycles with smaller strain amplitudes. This might affect the damage accumulation process of ELCF or might enroll another fatigue mechanism that the MMC model with extension did not capture. However, in the field of ELCF prediction research, this study has a potential to many applications.

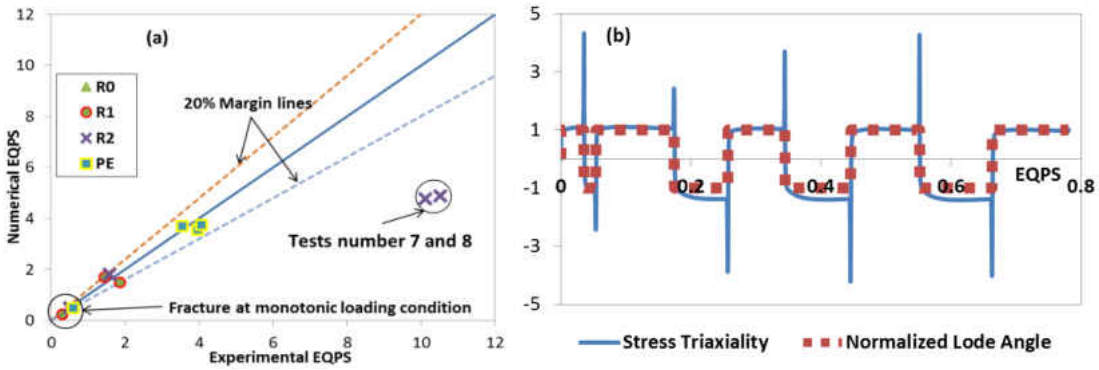

Figure 79: (a) The predicted vs. experimental accumulated EQPS at the instant of the failure. The prediction results are for ductile fracture of monotonic loading and ELCF, (b) Stress triaxiality and Lode angle versus EQPS (at the center of the specimen) during some cyclic loadings.

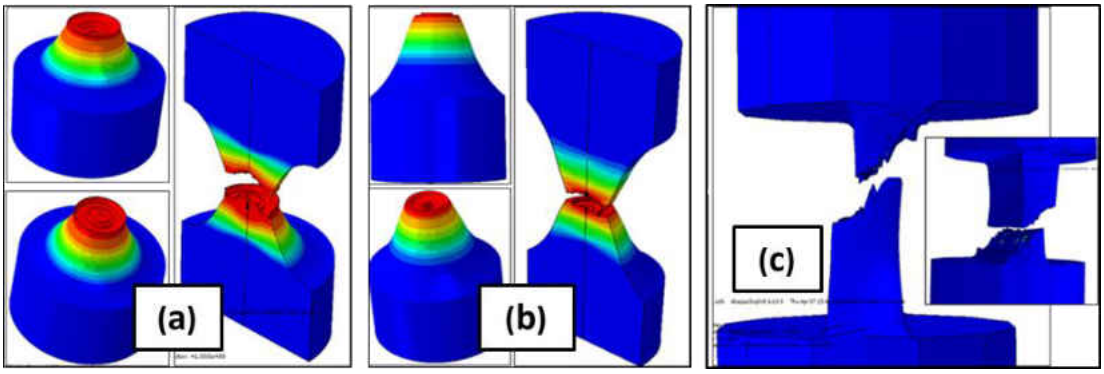

Figure 80: Numerical fracture simulations show cup-cone fracture patterns on the sharp notch bar (a), the large notch bar (b), and slant fracture mode for the plain strain specimen (c). The contour plot is the damage accumulation (D) in Abaqus.

6.9 Model Validation

The proposed MMC model with extension was also validated by test data series designed and performed by (Bao and Treitler, 2004) in Ref. [218] and calibrated by (Bai

and Wierzbicki, 2010) in Ref. [25]. The round specimen's materials were Al 2024-T351 (Aluminum alloy) and designed with three different notch external radius (Figure 81 and Table 27). A total of 11 test condition cases of different pre-compression strain (Table 27) followed by tension to fracture. Using a similar approach of Ref. [218], the force vs. displacement curves for all cases were simulated by developing the specimens' models in FEA using Abaqus . The curves results show excellent correlations to the experimental data (Figure 82). The MMC model for ductile fracture under monotonic loading was calibrated for Al 2024-T351 in Ref. [25]. The 3D fracture locus for Al 2024-T351 is constructed and shown in (Figure 83). The results of the MMC model ductile fracture prediction are in excellent agreement with the experimental results.

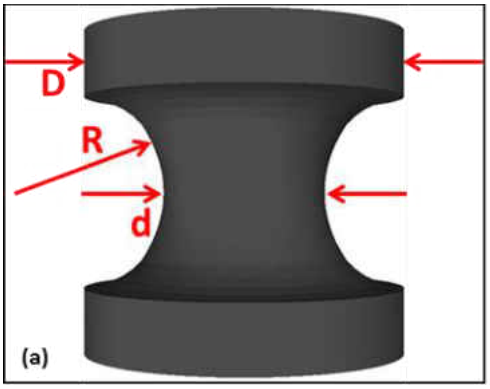

Figure 81: Main geometries and dimensions of the round bar (D = 22mm)

Table 27: A summary of the specimen's dimensions and tests

Loading case	Compression degree, %	Notch radius, R	Cross section diameter, d	Denotion
1	0	12	12	A1
2	1	12	12	A2
3	2	12	12	A3
4	3.5	12	12	A4
5	5	12	12	A5
6	2	12	9	B1

Loading case	Compression degree, %	Notch radius, R	Cross section diameter, d	Denotion
7	3	12	9	B2
8	5	12	9	B3
9	2	8	14	C1
10	3	8	14	C2
11	5	8	14	C3

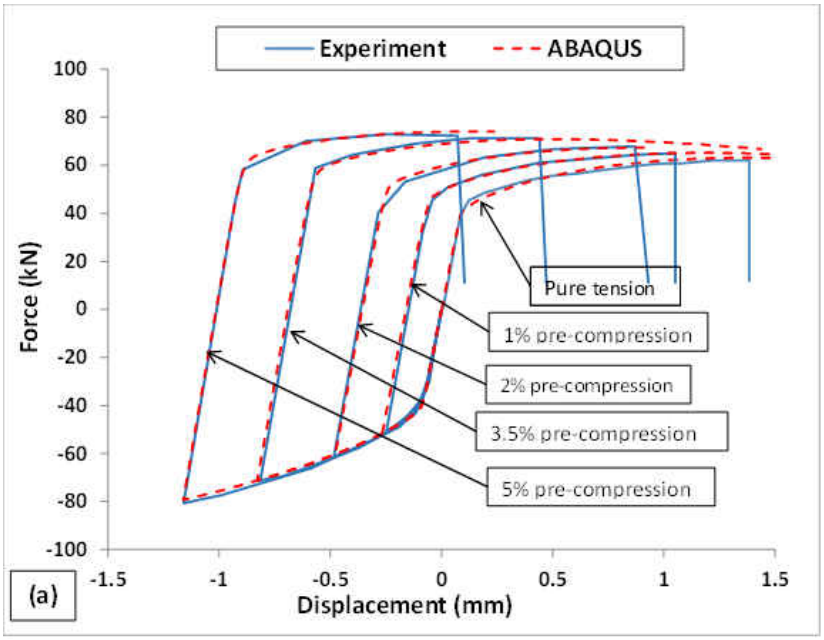

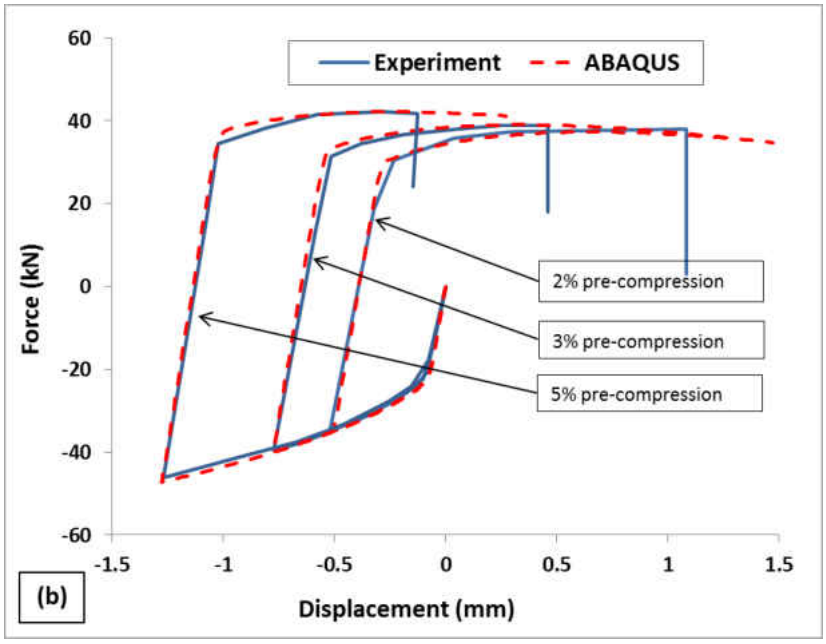

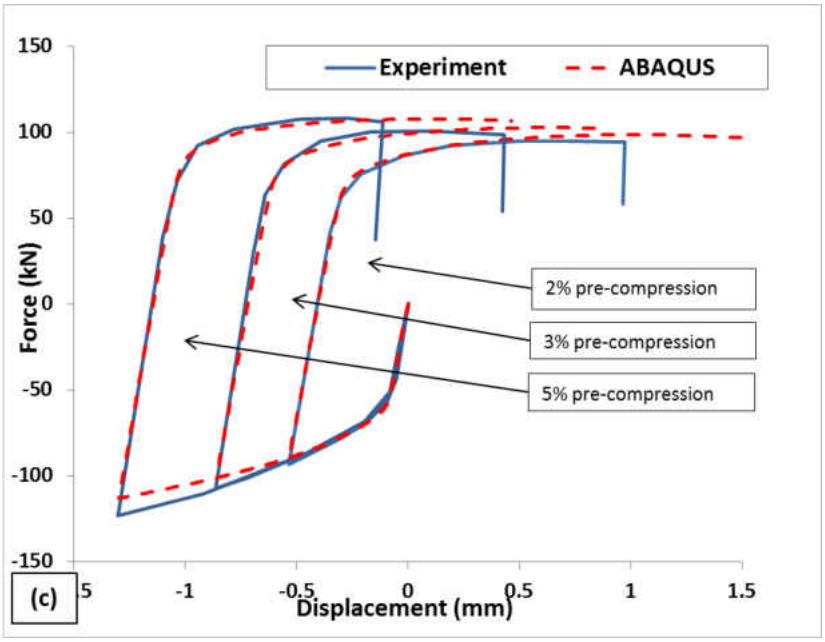

Figure 82: Comparison of load-displacement curves and predicted fracture displacements for Al 20204-T351: (a) Type A specimens; (b) Type B specimens; (c) Type C specimens.

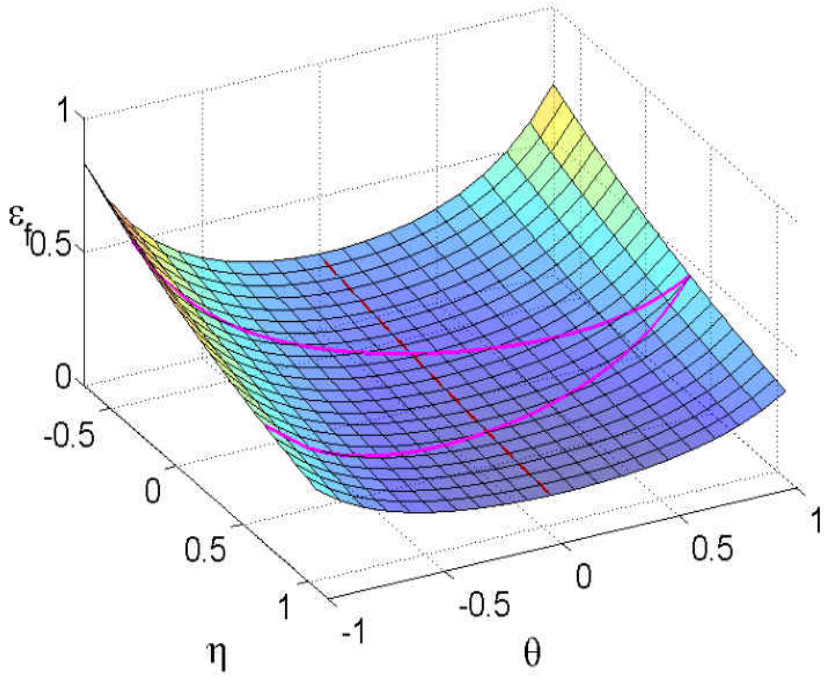

Figure 83: 3D MMC fracture locus for Al 2024-T351

Using a Matlab code, the calibration of the proposed MMC model with the extension is performed based on the literature results in Refs. [25, 218]. For comparison purposes, the ELCF initiation prediction based on the MMC criterion with extension will be denoted by "*Numerical EQPS"*. Likewise, EQPS at the instant of the experimental ELCF (obtained by FEA) is denoted by "*Experimental EQPS"*. The results for specimens A, B, and C validate the MMC model with the extension and indicate excellent ELCF predictions as shown in Figure 84.

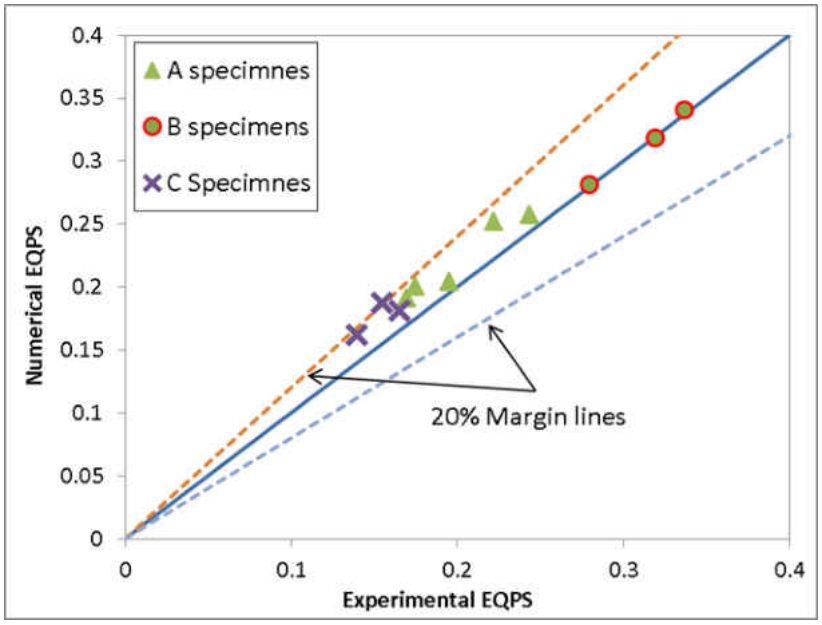

Figure 84: Experimental vs. predicted accumulated equivalent plastic strain at failure.

6.10 Discussion and Conclusion

Steel structures under seismic loading, gas turbine under high-pressure air current are ELCF life examples. ELCF is characterized by large strain amplitudes of cyclic loading that fails within few cycles (N_f < 100 cycles). The force vs. displacement behavior of IN718 for all tests under different stress states, different strain amplitudes, and different loading conditions were simulated with good accuracy. The MMC model was extended to consider ELCF regime by introducing two functions to the damage evolution rule. The first function controls the nonlinearity of the damage evolution. The second function incorporates the effect of the cyclic loading in ELCF by the loading direction change between the current stress and the backstress tensors. The fatigue

damage in ELCF is seen dominated by the enormous high level of plastic strain that causes huge ductility exhaustion within the metal. This huge ductility exhaustion leads the metal to fail in a very short time during the cyclic loading process. This is mainly presumed as the reason for the short fatigue life and the damage mechanism in ELCF. Also, it is clear from the fracture surface morphologies of each specimen that the fracture mechanism is very similar to that of the ductile fracture under monotonic loadings. The accuracy assessment of the MMC model with extension life prediction is quantified by the accumulated EQPS at the failure instant. The predicted EQPS at failure by the MMC criterion vs. the experimental EQPS at failure, obtained by FEA, show good agreement within the range of 20%. Finally, it can be concluded that the MMC model with the extension is applicable for ELCF and merits extensive consideration.

CHAPTER SEVEN:
CONCLUSION AND FUTURE WORK

7.1 Summary of Conclusion

An extensive amount of research outcome has been accomplished since the beginning of this study. Here is the summary of the research conclusions:

- Ductile fracture of IN718 under multi-axial loading conditions was achieved by novel designs of different specimen geometry. Four types of specimens (one smooth round bar, two notched round bars, and one plane strain specimen) were used to calibrate the fracture of IN718. It was found that ductile fracture strain of IN718 is strongly dependent on the stress states, especially the stress triaxiality. This phenomenon is usually contributed to the effect of hydrostatic pressure on the micro void growth and nucleation rate. The ELCF tests on IN718 on the same group of specimens indicate that the similar pressure dependent mechanism applies to ELCF. A novel method using stress triaxiality was proposed to describe the notch effect on material fatigue. The current tests were conducted under room temperature, quasi-static loading and fully reverse loading conditions.
- It was found that the stress state parameters (stress triaxiality and Lode angle parameter) have noteworthy effects on the plasticity and fracture of IN718. The plasticity model with pressure and Lode angle dependence proposed by Bai and Wierzbicki (BW) [4] was extended to describe the material's plasticity behavior, and the MMC fracture model [25] with a new post failure softening [60] was used to successfully predict both ductile fracture initiation and propagation. Finally, both

the fracture initiation and crack propagation in the finite element simulations show satisfactory agreement with test results for all four specimens.

- The current thesis has also demonstrated the combined kinematic and isotropic strain hardening along with the effect of the stress triaxiality and Lode angle parameter. It can accurately simulate the metals' force-displacement curves of different loading conditions and different stress states. A suitable damage accumulation rule was proposed by introducing two weighting functions to consider the nonlinearity behavior of the damage evolution and to capture the effect of the cyclic loading within the ELCF regime. The first function controls the nonlinearity of the damage evolution. The second function incorporates the effect of the cyclic loading in ELCF by the loading direction change between the current stress and the backstress tensors. The two extended functions are presumed to act independently and concurrently throughout a loading process. The proposed fracture model considers the cyclic loading conditions as well as the monotonic loading conditions. The range of error of the linear damage accumulation model is [60%, 90%], while the errors of the proposed nonlinear model significantly decreases to [5%, 19%].
- It has been found that the fatigue damage in ELCF is seen dominated by the enormous high level of plastic strain that causes huge ductility exhaustion within the metal. This huge ductility exhaustion leads the metal to fail in a very short time during the cyclic loading process. This is mainly presumed as the reason for the short fatigue life and the damage mechanism in ELCF. Also, it is clear from the fracture surface morphologies of each specimen that the fracture mechanism is very

similar to that of the ductile fracture under monotonic loadings. The accuracy assessment of the MMC model with extension life prediction is quantified by the accumulated EQPS at the failure instant. The predicted EQPS at failure by the MMC criterion vs. the experimental EQPS at failure, obtained by FEA, show good agreement within the range of 20%. Finally, it can be concluded that the extended MMC model is applicable for ELCF and merits extensive consideration.

7.2 Recommended Future Work

In the current thesis, a comprehensive set of experiments and simulations has been conducted and developed for predicting material plasticity, hardening, and fracture behaviors for IN718. Nevertheless, there are several more research aspects recommended for the future research. Here are some suggested topics:

1. **Wider applications**. The BW plasticity model was capable of simulating the IN718 plastic flow under ELCF. However, this model needs to be further tested to simulate a wide range of other materials under ELCF with different stress states.
2. **LCF Extension**. The BW plasticity model shown capable of predicting the metals' plasticity behavior under monotonic loading and ELCF. However, it has never been tested for Low Cycle Fatigue under multiaxial stresses states.
3. **Mean stress effect in ELCF**. The MMC model in this research shows good results in predicting ELCF for IN718. However, our experimental study did not include positive nor negative mean stress effect during the fatigue tests. It is recommended to verify the MMC model capabilities in predicting ELCF with positive and negative mean stress.

4. **Crack propagation**. The crack initiation, growth, and coalescence for monotonic loading cases were flawlessly simulated in FEM by element deletion. However, for cyclic loading, crack closure during compression loading might unstable the crack propagation phase. This strategy might lead to inappropriate simulation when simulating real structure configuration. Therefore, appropriate fatigue crack simulation can be simulated by using element split technique in the future research.
5. **Environmental effect**. In real applications, the materials of engineering structures and components are subjected to different environmental effects that will impact the materials behavior and life span. The suggested environmental effects are: high-temperature effects, corrosion environment effects, and high strain rates effects. Thus, it is vital to apply the current theoretical framework to include these environmental effects in future studies.

APPENDIX: RESEARCH PAPERS AND PRESENTATIONS

Here are the **published or submitted** papers for publication:

1. **Algarni, Mohammed**, Yuanli Bai, and Youngsik Choi. "A study of Inconel 718 dependency on stress triaxiality and Lode angle in plastic deformation and ductile fracture." Engineering Fracture Mechanics 147 (2015): 140-157.
2. **M. Algarni**, Y. Jia, J. Karl, A. P. Gordon, Y. Bai, M. The Minerals*, et al.*, "Linkage between Ductile Fracture and Extremely Low Cycle Fatigue of Inconel 718 Under Multiaxial Loading Conditions," in *TMS2015 Supplemental Proceedings*, ed: John Wiley & Sons, Inc., 2015, pp. 1023-1030.
3. **M. Algarni**, Y. Bai., "Extremely Low Cycle Fatigue Damage Mechanism, Fractographic Examination, And Life Prediction," in Materials Science & Technology Conference and Exhibition 2016; Supplemental Proceedings, Salt Lake City, Utah, USA, *publication due in October 2016.*
4. Long, X., Bai, Y., **Algarni, M.,** Choi, Y., & Chen, Q. (2015). "Study on the strengthening mechanisms of Cu/CNT nano-composites". Materials Science and Engineering: A, 645, 347-356.
5. Shabahang, Soroush, Felix Tan, Joshua Perlstein, Guangming Tao, **Mohammed Algarni**, Yuanli Bai, Oseas Alvarez et al. "Hybridized Fabrication of Robust Low-Loss Multimaterial Chalcogenide Fiber for Infrared Applications." In CLEO: Science and Innovations, pp. JF1K-3. Optical Society of America, 2016..
6. **Algarni, Mohammed**, Youngsik Choi, and Yuanli Bai. "A unified material model for multiaxial ductile fracture and extremely low cycle fatigue of Inconel 718." *International Journal of Fatigue* (2016).

Here are the conference **presentations** performed by the author:

1. "Linkage between Ductile Fracture and Extremely Low Cycle Fatigue of Inconel 718 Under Multiaxial Loading Conditions," in **TMS2015** Orlando March 16, @ Walt Disney World Swan and Dolphin Resort.
2. “Extremely Low Cycle Fatigue Damage Mechanism, Fractographic Examination, And Life Prediction," in Materials Science & Technology Conference and Exhibition **MS&T2016**; Salt Lake City, Utah, USA, presentation due in October 24, 2016.

REFERENCES

[1] J. S. Rao, *Turbomachine blade vibration*: New Age International, 1991.

[2] N. F. Rieger, "Blade Fatigue," 1983.

[3] N. S. Vyas and J. S. Rao, "Fatigue life estimation procedure for a turbine blade under transient loads," *Journal of engineering for gas turbines and power,* vol. 116, pp. 198-206, 1994.

[4] Y. Bai and T. Wierzbicki, "A new model of metal plasticity and fracture with pressure and Lode dependence," *International Journal of Plasticity,* vol. 24, pp. 1071-1096, 6// 2008.

[5] G. Gruben, O. S. Hopperstad, and T. Børvik, "Evaluation of uncoupled ductile fracture criteria for the dual-phase steel Docol 600DL," *International Journal of Mechanical Sciences,* vol. 62, pp. 133-146, 9// 2012.

[6] M. Achouri, G. Germain, P. Dal Santo, and D. Saidane, "Experimental characterization and numerical modeling of micromechanical damage under different stress states," *Materials & Design,* vol. 50, pp. 207-222, 9// 2013.

[7] K. Nahshon and J. W. Hutchinson, "Modification of the Gurson model for shear failure," *European Journal of Mechanics-A/Solids,* vol. 27, pp. 1-17, 2008.

[8] L. Xue, "Constitutive modeling of void shearing effect in ductile fracture of porous materials," *Engineering Fracture Mechanics,* vol. 75, pp. 3343-3366, 7// 2008.

[9] B. Erice and F. Gálvez, "A coupled elastoplastic-damage constitutive model with Lode angle dependent failure criterion," *International Journal of Solids and Structures,* vol. 51, pp. 93-110, 1/1/ 2014.

[10] G. R. Johnson and W. H. Cook, "A constitutive model and data for metals subjected to large strains, high strain rates and high temperatures," 1983, pp. 541-547.

[11] S. Bari and T. Hassan, "Anatomy of coupled constitutive models for ratcheting simulation," *International Journal of Plasticity,* vol. 16, pp. 381-409, 2000.

[12] S. Bari and T. Hassan, "An advancement in cyclic plasticity modeling for multiaxial ratcheting simulation," *International Journal of Plasticity,* vol. 18, pp. 873-894, 2002.

[13] S. Bari and T. Hassan, "Kinematic hardening rules in uncoupled modeling for multiaxial ratcheting simulation," *International Journal of Plasticity,* vol. 17, pp. 885-905, 2001.

[14] J.-L. Chaboche, "Constitutive equations for cyclic plasticity and cyclic viscoplasticity," *International journal of plasticity,* vol. 5, pp. 247-302, 1989.

[15] J. L. Chaboche, K. Dang Van, and G. Cordier, "Modelization of the strain memory effect on the cyclic hardening of 316 stainless steel," in *Structural mechanics in reactor technology. Transactions. Vol. L*, ed, 1979.

[16] J.-L. Chaboche, "On some modifications of kinematic hardening to improve the description of ratchetting effects," *International journal of plasticity,* vol. 7, pp. 661-678, 1991.

[17] J.-L. Chaboche, "Time-independent constitutive theories for cyclic plasticity," *International Journal of Plasticity,* vol. 2, pp. 149-188, 1986.

[18] D. L. McDowell, "Stress state dependence of cyclic ratchetting behavior of two rail steels," *International Journal of Plasticity,* vol. 11, pp. 397-421, 1995.

[19] Y. Jiang and H. Sehitoglu, "Modeling of cyclic ratchetting plasticity, part I: development of constitutive relations," *Journal of Applied Mechanics,* vol. 63, pp. 720-725, 1996.

[20] Y. Jiang and H. Sehitoglu, "Modeling of cyclic ratchetting plasticity, part II: comparison of model simulations with experiments," *Journal of Applied Mechanics,* vol. 63, pp. 726-733, 1996.

[21] X. Chen, R. Jiao, and K. S. Kim, "On the Ohno–Wang kinematic hardening rules for multiaxial ratcheting modeling of medium carbon steel," *International Journal of Plasticity,* vol. 21, pp. 161-184, 2005.

[22] X. Chen and R. Jiao, "Modified kinematic hardening rule for multiaxial ratcheting prediction," *International Journal of Plasticity,* vol. 20, pp. 871-898, 2004.

[23] L. Xue, "Damage accumulation and fracture initiation in uncracked ductile solids subject to triaxial loading," *International Journal of Solids and Structures,* vol. 44, pp. 5163-5181, 8/1/ 2007.

[24] L. Xue and T. Wierzbicki, "Numerical simulation of fracture mode transition in ductile plates," *International Journal of Solids and Structures,* vol. 46, pp. 1423-1435, 2009.

[25] Y. Bai and T. Wierzbicki, "Application of extended Mohr–Coulomb criterion to ductile fracture," *International Journal of Fracture,* vol. 161, pp. 1-20, 2010/01/01 2010.

[26] G. R. Johnson and W. H. Cook, "Fracture characteristics of three metals subjected to various strains, strain rates, temperatures and pressures," *Engineering fracture mechanics,* vol. 21, pp. 31-48, 1985.

[27] L. Xue and T. Wierzbicki, "Ductile fracture initiation and propagation modeling using damage plasticity theory," *Engineering Fracture Mechanics,* vol. 75, pp. 3276-3293, 2008.

[28] Z. Xue, M. G. Pontin, F. W. Zok, and J. W. Hutchinson, "Calibration procedures for a computational model of ductile fracture," *Engineering Fracture Mechanics,* vol. 77, pp. 492-509, 2// 2010.

[29] J.-L. Chaboche, "Continuum damage mechanics: Part II—Damage growth, crack initiation, and crack growth," *Journal of applied mechanics,* vol. 55, pp. 65-72, 1988.

[30] J. L. Chaboche and G. Rousselier, "On the plastic and viscoplastic constitutive equations—Part I: Rules developed with internal variable concept," *Journal of Pressure Vessel Technology,* vol. 105, pp. 153-158, 1983.

[31] A. F. Liu, *Mechanics and mechanisms of fracture: an introduction*: ASM International, 2005.

[32] K. Shimada, J. Komotori, and M. Shimizu, "The applicability of the Manson-Coffin law and Miner's law to extremely low cycle fatigue," *TRANS. JAPAN SOC. MECH. ENG.(SER. A).* vol. 53, pp. 1178-1185, 1987.

[33] M. Kuroda, "Extremely low cycle fatigue life prediction based on a new cumulative fatigue damage model," *International Journal of Fatigue,* vol. 24, pp. 699-703, 2002.

[34] L. Xue, "A unified expression for low cycle fatigue and extremely low cycle fatigue and its implication for monotonic loading," *International Journal of Fatigue,* vol. 30, pp. 1691-1698, 2008.

[35] K. Tateishi, T. Hanji, and K. Minami, "A prediction model for extremely low cycle fatigue strength of structural steel," *International Journal of fatigue,* vol. 29, pp. 887-896, 2007.

[36] M. Kamaya, "Fatigue properties of 316 stainless steel and its failure due to internal cracks in low-cycle and extremely low-cycle fatigue regimes," *International Journal of Fatigue,* vol. 32, pp. 1081-1089, 2010.

[37] H. Zhou, Y. Wang, Y. Shi, J. Xiong, and L. Yang, "Extremely low cycle fatigue prediction of steel beam-to-column connection by using a micro-mechanics based fracture model," *International Journal of Fatigue,* vol. 48, pp. 90-100, 2013.

[38] M. Luo, M. Dunand, and D. Mohr, "Experiments and modeling of anisotropic aluminum extrusions under multi-axial loading – Part II: Ductile fracture," *International Journal of Plasticity,* vol. 32–33, pp. 36-58, 5// 2012.

[39] K. H. Nip, L. Gardner, C. M. Davies, and A. Y. Elghazouli, "Extremely low cycle fatigue tests on structural carbon steel and stainless steel," *Journal of constructional steel research,* vol. 66, pp. 96-110, 2010.

[40] J. Dufailly and J. Lemaitre, "Modeling very low cycle fatigue," *International Journal of damage mechanics,* vol. 4, pp. 153-170, 1995.

[41] P. Mešťáneka, "Low cycle fatigue analysis of a last stage steam turbine blade," 2008.

[42] Y. Bao, "Dependence of ductile crack formation in tensile tests on stress triaxiality, stress and strain ratios," *Engineering Fracture Mechanics,* vol. 72, pp. 505-522, 3// 2005.

[43] Y. Bai, "Effect of loading history in necking and fracture," *Doctoral dissertation, Massachusetts Institute of Technolog,* 2008.

[44] L. Malcher, F. M. Andrade Pires, J. M. A. César de Sá, and F. X. C. Andrade, "Numerical integration algorithm of a new model for metal plasticity and fracture including pressure and lode angle dependence," *International Journal of Material Forming,* vol. 2, pp. 443-446, 2009/08/01 2009.

[45] F. A. McClintock, "A criterion for ductile fracture by the growth of holes," *Journal of applied mechanics,* vol. 35, pp. 363-371, 1968.

[46] J. R. Rice and D. M. Tracey, "On the ductile enlargement of voids in triaxial stress fields∗," *Journal of the Mechanics and Physics of Solids,* vol. 17, pp. 201-217, 1969.

[47] J. W. Hancock and A. C. Mackenzie, "On the mechanisms of ductile failure in high-strength steels subjected to multi-axial stress-states," *Journal of the Mechanics and Physics of Solids,* vol. 24, pp. 147-160, 1976.

[48] J. W. Hancock and D. K. Brown, "On the role of strain and stress state in ductile failure," *Journal of the Mechanics and Physics of Solids,* vol. 31, pp. 1-24, 1983.

[49] T. S. Cao, J. M. Gachet, P. Montmitonnet, and P. O. Bouchard, "A Lode-dependent enhanced Lemaitre model for ductile fracture prediction at low stress triaxiality," *Engineering Fracture Mechanics,* vol. 124–125, pp. 80-96, 7// 2014.

[50] J. M. Gachet, G. Delattre, and P. O. Bouchard, "Fracture mechanisms under monotonic and non-monotonic low Lode angle loading," *Engineering Fracture Mechanics,* vol. 124–125, pp. 121-141, 7// 2014.

[51] Y. J. Liu, Q. Sun, X. L. Fan, and T. Suo, "A stress-invariant based multi-parameters ductile progressive fracture model," *Materials Science and Engineering: A,* vol. 576, pp. 337-345, 8/1/ 2013.

[52] R. Ghajar, G. Mirone, and A. Keshavarz, "Sensitivity Analysis on Triaxiality Factor and Lode Angle in Ductile Fracture," *Journal of Mechanics,* vol. 29, pp. 177-184, 2013.

[53] X. Gao, T. Wang, and J. Kim, "On ductile fracture initiation toughness: Effects of void volume fraction, void shape and void distribution," *International Journal of Solids and Structures,* vol. 42, pp. 5097-5117, 9// 2005.

[54] X. Gao and J. Kim, "Modeling of ductile fracture: Significance of void coalescence," *International Journal of Solids and Structures,* vol. 43, pp. 6277-6293, 10// 2006.

[55] X. Gao, T. Zhang, M. Hayden, and C. Roe, "Effects of the stress state on plasticity and ductile failure of an aluminum 5083 alloy," *International Journal of Plasticity,* vol. 25, pp. 2366-2382, 12// 2009.

[56] Y. Li and T. Wierzbicki, "Prediction of plane strain fracture of AHSS sheets with post-initiation softening," *International Journal of Solids and Structures,* vol. 47, pp. 2316-2327, 8/15/ 2010.

[57] M. Dunand and D. Mohr, "On the predictive capabilities of the shear modified Gurson and the modified Mohr–Coulomb fracture models over a wide range of stress triaxialities and Lode angles," *Journal of the Mechanics and Physics of Solids,* vol. 59, pp. 1374-1394, 7// 2011.

[58] M. Luo and T. Wierzbicki, "Numerical failure analysis of a stretch-bending test on dual-phase steel sheets using a phenomenological fracture model," *International Journal of Solids and Structures,* vol. 47, pp. 3084-3102, 11// 2010.

[59] Y. Li and T. Wierzbicki, "Mesh-size effect study of ductile fracture by non-local approach," 2009.

[60] Y. Bai and T. Atkins, "Tension and shear cracking during indentation of ductile materials by opposed wedges," *Engineering Fracture Mechanics,* vol. 96, pp. 49-60, 12// 2012.

[61] S. K. Iyer and C. J. Lissenden, "Multiaxial constitutive model accounting for the strength-differential in Inconel 718," *International Journal of Plasticity,* vol. 19, pp. 2055-2081, 12// 2003.

[62] D. C. Drucker, "Relation of experiments to mathematical theories of plasticity," *JOURNAL OF APPLIED MECHANICS-TRANSACTIONS OF THE ASME,* vol. 16, pp. 349-357, 1949.

[63] W. Prager and D. C. Drucker, "Soil mechanics and plastic analysis or limit design, 0," *Appi. Math,* vol. 10, pp. 157-165, 1952.

[64] T. Kobayashi, J. W. Simons, C. S. Brown, and D. A. Shockey, "Plastic flow behavior of Inconel 718 under dynamic shear loads," *International Journal of Impact Engineering,* vol. 35, pp. 389-396, 5// 2008.

[65] M. Becker and H.-P. Hackenberg, "A constitutive model for rate dependent and rate independent inelasticity. Application to IN718," *International Journal of Plasticity,* vol. 27, pp. 596-619, 4// 2011.

[66] J. M. Pereira and B. A. Lerch, "Effects of heat treatment on the ballistic impact properties of Inconel 718 for jet engine fan containment applications," *International Journal of Impact Engineering,* vol. 25, pp. 715-733, 9// 2001.

[67] J. J. Lewandowski, P. Wesseling, N. S. Prabhu, J. Larose, and B. A. Lerch, "Strength differential measurements in IN 718: Effects of superimposed pressure," *Metallurgical and Materials Transactions A,* vol. 34, pp. 1736-1739, 2003/08/01 2003.

[68] B. Erice, M. J. Pérez-Martín, and F. Gálvez, "An experimental and numerical study of ductile failure under quasi-static and impact loadings of Inconel 718 nickel-base superalloy," *International Journal of Impact Engineering,* vol. 69, pp. 11-24, 7// 2014.

[69] J. P. Meyer and J. F. Labuz, "Linear failure criteria with three principal stresses," *International Journal of Rock Mechanics and Mining Sciences,* vol. 60, pp. 180-187, 2013.

[70] B. Erice Echávarri, "Flow and fracture behaviour of high performance alloys," 2012.

[71] P. W. Bridgman, *Studies in large plastic flow and fracture with special emphasis on the effects of hydrostatic pressure*: McGraw-Hill, 1952.

[72] P. W. Bridgman, *Studies in large plastic flow and fracture*: Harvard University Press, 1964.

[73] J. Lubliner, *Plasticity theory*: Courier Corporation, 2008.

[74] W. Prager and D. C. Drucker, "Soil mechanics and plastic analysis or limit design," *Appi. Math,* vol. 10, pp. 157-165, 1952.

[75] H.-É. Tresca, *Compte rendu de la soirée scientifique du 29 octobre 1864 au Conservatoire des arts et métiers*: E. Lacroix, 1864.

[76] R. Von Mises, "Göttinger Nachrichten," *Math. Phys. Klasse,* p. 582, 1913.

[77] L. M. Kachanov, "Time of the rupture process under creep conditions," *Isv. Akad. Nauk. SSR. Otd Tekh. Nauk,* vol. 8, pp. 26-31, 1958.

[78] Y. U. Rabotnov, "N., 1968. Creep rupture," pp. 342-349.

[79] E. A. de Souza Neto, D. Peric, and D. R. J. Owen, *Computational methods for plasticity: theory and applications*: John Wiley & Sons, 2011.

[80] J. Lemaitre, "A three-dimensional ductile damage model applied to deep-drawing forming limits," *Mechanical Behavior of Materials--IV,* vol. 2, pp. 1059-1065, 1983.

[81] J. Lemaitre and H. Lippmann, *A course on damage mechanics* vol. 2: Springer Berlin, 1996.

[82] M. L. Wilkins, R. D. Streit, and J. E. Reaugh, "Cumulative-strain-damage model of ductile fracture: simulation and prediction of engineering fracture tests," Lawrence Livermore National Lab., CA (USA); Science Applications, Inc., San Leandro, CA (USA)1980.

[83] M. L. Wilkins, *Computer simulation of dynamic phenomena*: Springer Science & Business Media, 1999.

[84] A. Brownrigg, W. A. Spitzig, O. Richmond, D. Teirlinck, and J. D. Embury, "The influence of hydrostatic pressure on the flow stress and ductility of a spherodized 1045 steel," *Acta Metallurgica,* vol. 31, pp. 1141-1150, 1983.

[85] M. Brünig, "Numerical simulation of the large elastic–plastic deformation behavior of hydrostatic stress-sensitive solids," *International Journal of Plasticity,* vol. 15, pp. 1237-1264, 1999.

[86] O. Richmond and W. A. Spitzig, "Pressure dependence and dilatancy of plastic flow," *Theoretical and applied mechanics,* pp. 377-386, 1980.

[87] W. A. Spitzig and O. Richmond, "The effect of pressure on the flow stress of metals," *Acta metallurgica,* vol. 32, pp. 457-463, 1984.

[88] J. Rottler and M. O. Robbins, "Yield conditions for deformation of amorphous polymer glasses," *Physical Review E,* vol. 64, p. 051801, 2001.

[89] N. Bonora and A. Ruggiero, "Micromechanical modeling of ductile cast iron incorporating damage. Part I: Ferritic ductile cast iron," *International Journal of Solids and Structures,* vol. 42, pp. 1401-1424, 3// 2005.

[90] N. Bonora, D. Gentile, A. Pirondi, and G. Newaz, "Ductile damage evolution under triaxial state of stress: theory and experiments," *International Journal of Plasticity,* vol. 21, pp. 981-1007, 2005.

[91] A. Pirondi and N. Bonora, "Modeling ductile damage under fully reversed cycling," *Computational Materials Science,* vol. 26, pp. 129-141, 2003.

[92] J. Lemaitre and J.-L. Chaboche, *Mechanics of solid materials*: Cambridge university press, 1990.

[93] J. Lemaitre, "Coupled elasto-plasticity and damage constitutive equations," *Computer Methods in Applied Mechanics and Engineering,* vol. 51, pp. 31-49, 1985.

[94] J. Lemaitre, "A continuous damage mechanics model for ductile fracture," *Journal of Engineering Materials and Technology,* vol. 107, pp. 83-89, 1985.

[95] A. L. Gurson, "Continuum theory of ductile rupture by void nucleation and growth: Part I—Yield criteria and flow rules for porous ductile media," *Journal of engineering materials and technology,* vol. 99, pp. 2-15, 1977.

[96] V. Tvergaard, "Influence of voids on shear band instabilities under plane strain conditions," *International Journal of Fracture,* vol. 17, pp. 389-407, 1981.

[97] V. Tvergaard, "On localization in ductile materials containing spherical voids," *International Journal of Fracture,* vol. 18, pp. 237-252, 1982.

[98] V. Tvergaard and A. Needleman, "Analysis of the cup-cone fracture in a round tensile bar," *Acta metallurgica,* vol. 32, pp. 157-169, 1984.

[99] C. C. Chu and A. Needleman, "Void nucleation effects in biaxially stretched sheets," *Journal of Engineering Materials and Technology(Transactions of the ASME),* vol. 102, pp. 249-256, 1980.

[100] M. G. Cockcroft and D. J. Latham, "Ductility and the workability of metals," *J Inst Metals,* vol. 96, pp. 33-39, 1968.

[101] T. Børvik, O. S. Hopperstad, T. Berstad, and M. Langseth, "A computational model of viscoplasticity and ductile damage for impact and penetration," *European Journal of Mechanics-A/Solids,* vol. 20, pp. 685-712, 2001.

[102] G. R. Bhashyam, "ANSYS Mechanical—A Powerful Nonlinear Simulation Tool," *Ansys, Inc,* 2002.

[103] J. H. Hollomon, "Tensile deformation," *AIME TRANS,* vol. 12, pp. 1-22, 1945.

[104] P. Ludwik, "Elemente der technischen Mechanik," *J. Springer, Berlin,* 1909.

[105] H. W. Swift, "Plastic instability under plane stress," *Journal of the Mechanics and Physics of Solids,* vol. 1, pp. 1-18, 1952.

[106] S. K. Samanta, "Resistance to dynamic compression of low-carbon steel and alloy steels at elevated temperatures and at high strain-rates," *International Journal of Mechanical Sciences,* vol. 10, pp. 613-636, 1968.

[107] E. Voce, "The relationship between stress and strain for homogeneous deformation," *J Inst Met,* vol. 74, pp. 537-562, 1948.

[108] E. Voce, "A practical strain-hardening function," *Metallurgia,* vol. 51, pp. 219-226, 1955.

[109] Z. Misiolek, J. Kowalczyk, and P. Kastner, "Investigation of Plastic Flow Stresses of Zn and Its Alloys," *Arch. Hutn.,* vol. 22, pp. 71-88, 1977.

[110] A. Abel, "Historical perspectives and some of the main features of the Bauschinger effect," pp. 11-26.

[111] W. Prager, "Recent developments in the mathematical theory of plasticity," *Journal of Applied Physics,* vol. 20, pp. 235-241, 1949.

[112] H. Ziegler, *A modification of Prager's hardening rule*, 1959.

[113] Z. Mroz, "On the description of anisotropic workhardening," *Journal of the Mechanics and Physics of Solids,* vol. 15, pp. 163-175, 1967.

[114] Y. F. Dafalias and E. P. Popov, "A model of nonlinearly hardening materials for complex loading," *Acta Mechanica,* vol. 21, pp. 173-192, 1975.

[115] Y. F. Dafalias and E. P. Popov, "Plastic internal variables formalism of cyclic plasticity," *Journal of applied mechanics,* vol. 43, pp. 645-651, 1976.

[116] H. Petersson and E. P. Popov, "Constitutive relations for generalized loadings," *Journal of the Engineering Mechanics Division,* vol. 103, pp. 611-627, 1977.

[117] N. T. Tseng and G. C. Lee, "Simple plasticity model of two-surface type," *Journal of Engineering Mechanics,* vol. 109, pp. 795-810, 1983.

[118] M. Minagawa, T. Nishiwaki, and N. Masuda, "Modelling cyclic plasticity of structural steels," *Structural Eng./Earthquake Eng,* vol. 4, pp. 361-370, 1987.

[119] A. F. Bower, "Cyclic hardening properties of hard-drawn copper and rail steel," *Journal of the Mechanics and Physics of Solids,* vol. 37, pp. 455-470, 1989.

[120] E. Mizuno, C. Shen, Y. Tanaka, and T. Usami, "A uniaxial stress-strain model for structural steels under cyclic loading," ed: CRC Press, Boca Raton, FL, 1992, pp. 37-48.

[121] C. Shen, Y. Tanaka, E. Mizuno, and T. Usami, "A two-surface model for steels with yield plateau," *Structural Eng./Earthquake Eng,* pp. 179s-188s, 1992.

[122] I. N. Basuroychowdhury and G. Z. Voyiadjis, "A multiaxial cyclic plasticity model for non-proportional loading cases," *International Journal of Plasticity,* vol. 14, pp. 855-870, 1998.

[123] F.-J. Montáns, "Bounding surface plasticity model with extended Masing behavior," *Computer methods in applied mechanics and engineering,* vol. 182, pp. 135-162, 2000.

[124] L. Geng and R. H. Wagoner, "Role of plastic anisotropy and its evolution on springback," *International Journal of Mechanical Sciences,* vol. 44, pp. 123-148, 2002.

[125] F. Yoshida, "A constitutive model of cyclic plasticity," *International Journal of Plasticity,* vol. 16, pp. 359-380, // 2000.

[126] F. Yoshida and T. Uemori, "A model of large-strain cyclic plasticity describing the Bauschinger effect and workhardening stagnation," *International Journal of Plasticity,* vol. 18, pp. 661-686, 2002.

[127] F. Yoshida and T. Uemori, "A model of large-strain cyclic plasticity and its application to springback simulation," *International Journal of Mechanical Sciences,* vol. 45, pp. 1687-1702, 2003.

[128] M.-G. Lee, D. Kim, C. Kim, M. L. Wenner, R. H. Wagoner, and K. Chung, "A practical two-surface plasticity model and its application to spring-back prediction," *International Journal of Plasticity,* vol. 23, pp. 1189-1212, 2007.

[129] P. J. Armstrong and C. O. Frederick, *A mathematical representation of the multiaxial Bauschinger effect*: Central Electricity Generating Board [and] Berkeley Nuclear Laboratories, Research & Development Department, 1966.

[130] M. Ekh, A. Johansson, H. Thorberntsson, and B. L. Josefson, "Models for cyclic ratchetting plasticity—integration and calibration," *Journal of engineering materials and technology,* vol. 122, pp. 49-55, 2000.

[131] A. H. Mahmoudi, S. M. Pezeshki-Najafabadi, and H. Badnava, "Parameter determination of Chaboche kinematic hardening model using a multi objective Genetic Algorithm," *Computational Materials Science,* vol. 50, pp. 1114-1122, 2011.

[132] M. Rezaiee-Pajand and S. Sinaie, "On the calibration of the Chaboche hardening model and a modified hardening rule for uniaxial ratcheting prediction," *International Journal of Solids and Structures,* vol. 46, pp. 3009-3017, 2009.

[133] G.-H. Koo and J.-H. Lee, "Investigation of ratcheting characteristics of modified 9Cr–1Mo steel by using the Chaboche constitutive model," *International Journal of Pressure Vessels and Piping,* vol. 84, pp. 284-292, 2007.

[134] R. I. Stephens, A. Fatemi, R. R. Stephens, and H. O. Fuchs, *Metal Fatigue in Engineering*: John Wiley & Sons, 2000.

[135] O. H. Basquin, "The exponential law of endurance tests," pp. 625-630.

[136] S. S. Manson, "Discussion:“Experimental Support for Generalized Equation Predicting Low Cycle Fatigue”(Tavernelli, JF, and Coffin, Jr., LF, 1962, ASME J. Basic Eng., 84, pp. 533–537)," *Journal of Fluids Engineering,* vol. 84, pp. 537-541, 1962.

[137] J. F. Tavernelli and L. F. Coffin, "Experimental support for generalized equation predicting low cycle fatigue," *Journal of Fluids Engineering,* vol. 84, pp. 533-537, 1962.

[138] S. S. Manson, "Fatigue: a complex subject—some simple approximations," *Experimental mechanics,* vol. 5, pp. 193-226, 1965.

[139] J. H. Ong, "An improved technique for the prediction of axial fatique life from tensile data," *International journal of fatigue,* vol. 15, pp. 213-219, 1993.

[140] J.-H. Park and J.-H. Song, "Detailed evaluation of methods for estimation of fatigue properties," *International Journal of Fatigue,* vol. 17, pp. 365-373, 1995.

[141] K. S. Kim, X. Chen, C. Han, and H. W. Lee, "Estimation methods for fatigue properties of steels under axial and torsional loading," *International journal of fatigue,* vol. 24, pp. 783-793, 2002.

[142] M. A. Meggiolaro and J. T. P. Castro, "Statistical evaluation of strain-life fatigue crack initiation predictions," *International Journal of Fatigue,* vol. 26, pp. 463-476, 2004.

[143] J. Morrow, "Fatigue properties of metals," *Fatigue Design Handbook,* pp. 21-30, 1968.

[144] S. S. Manson and G. R. Halford, "Practical implementation of the double linear damage rule and damage curve approach for treating cumulative fatigue damage," *International Journal of Fracture,* vol. 17, pp. 169-192, 1981.

[145] A. Ince and G. Glinka, "A modification of Morrow and Smith–Watson–Topper mean stress correction models," *Fatigue & Fracture of Engineering Materials & Structures,* vol. 34, pp. 854-867, 2011.

[146] L. F. Coffin, "The effect of high vacuum on the low cycle fatigue law," *Metallurgical Transactions,* vol. 3, pp. 1777-1788, 1972.

[147] S. Predmore, "The normalization of deviance."

[148] Q. Chen, N. Kawagoishi, and H. Nisitani, "Evaluation of fatigue crack growth rate and life prediction of Inconel 718 at room and elevated temperatures," *Materials Science and Engineering: A,* vol. 277, pp. 250-257, 2000.

[149] N. Shamsaei and S. A. McKelvey, "Multiaxial life predictions in absence of any fatigue properties," *International Journal of Fatigue,* vol. 67, pp. 62-72, 2014.

[150] A. Ince and G. Glinka, "A generalized fatigue damage parameter for multiaxial fatigue life prediction under proportional and non-proportional loadings," *International Journal of Fatigue,* vol. 62, pp. 34-41, 2014.

[151] M. W. Brown and K. J. Miller, "A theory for fatigue failure under multiaxial stress-strain conditions," *Proceedings of the Institution of Mechanical Engineers,* vol. 187, pp. 745-755, 1973.

[152] F. A. Kandil, M. W. Brown, and K. J. Miller, "Biaxial low-cycle fatigue failure of 316 stainless steel at elevated temperatures," in *Mechanical behaviour and nuclear applications of stainless steel at elevated temperatures*, ed, 1982.

[153] C. H. Wang and M. W. Brown, "A PATH-INDEPENDENT PARAMETER FOR FATIGUE UNDER PROPORTIONAL AND NON-PROPORTIONAL LOADING," *Fatigue & fracture of engineering materials & structures,* vol. 16, pp. 1285-1297, 1993.

[154] D. F. Socie, L. A. Waill, and D. F. Dittmer, "Biaxial fatigue of Inconel 718 including mean stress effects," *Multiaxial Fatigue,* pp. 463-481, 1985.

[155] A. Fatemi and D. F. Socie, "A Critical Plane Approach to Multiaxial Fatigue Damage Including out-of-Phase Loading," *Fatigue & Fracture of Engineering Materials & Structures,* vol. 11, pp. 149-165, 1988.

[156] Y. Bai, "Effect of loading history in necking and fracture," 2008.

[157] I. Barsoum and J. Faleskog, "Rupture mechanisms in combined tension and shear—Experiments," *International Journal of Solids and Structures,* vol. 44, pp. 1768-1786, 3/15/ 2007.

[158] I. Barsoum and J. Faleskog, "Rupture mechanisms in combined tension and shear—Micromechanics," *International Journal of Solids and Structures,* vol. 44, pp. 5481-5498, 8/15/ 2007.

[159] L. Xue, "Ductile fracture modeling: theory, experimental investigation and numerical verification," 2007.

[160] L. Xue and T. Wierzbicki, "Ductile fracture characterization of aluminum alloy 2024-T351 using damage plasticity theory," *International Journal of Applied Mechanics,* vol. 1, pp. 267-304, 2009.

[161] K. L. Nielsen and V. Tvergaard, "Effect of a shear modified Gurson model on damage development in a FSW tensile specimen," *International Journal of Solids and Structures,* vol. 46, pp. 587-601, 2009.

[162] A. A. Zadpoor, J. Sinke, and R. Benedictus, "Formability prediction of high strength aluminum sheets," *International Journal of Plasticity,* vol. 25, pp. 2269-2297, 2009.

[163] G. Mirone and D. Corallo, "A local viewpoint for evaluating the influence of stress triaxiality and Lode angle on ductile failure and hardening," *International Journal of Plasticity,* vol. 26, pp. 348-371, 2010.

[164] H. Li, M. W. Fu, J. Lu, and H. Yang, "Ductile fracture: experiments and computations," *International Journal of Plasticity,* vol. 27, pp. 147-180, 2011.

[165] T. B. Stoughton and J. W. Yoon, "A new approach for failure criterion for sheet metals," *International Journal of Plasticity,* vol. 27, pp. 440-459, 2011.

[166] A. S. Khan and H. Liu, "A new approach for ductile fracture prediction on Al 2024-T351 alloy," *International Journal of Plasticity,* vol. 35, pp. 1-12, 2012.

[167] L. Malcher and E. N. Mamiya, "An improved damage evolution law based on continuum damage mechanics and its dependence on both stress triaxiality and

the third invariant," *International Journal of Plasticity,* vol. 56, pp. 232-261, 2014.

[168] L. E. Malvern, *Introduction to the Mechanics of a Continuous Medium*, 1969.

[169] B. Xu and X. Liu, "Applied mechanics: elasticity and plasticity," ed: Tsinghua University Press, Beijing, China, 1995.

[170] R. E. Peterson, *Stress Concentration Design Factors*: J. Wiley & Sons, 1953.

[171] Y. Bai, X. Teng, and T. Wierzbicki, "On the Application of Stress Triaxiality Formula for Plane Strain Fracture Testing," *Journal of Engineering Materials and Technology,* vol. 131, p. 021002, 2009.

[172] W. J. Dan, W. G. Zhang, S. H. Li, and Z. Q. Lin, "An experimental investigation of large-strain tensile behavior of a metal sheet," *Materials & design,* vol. 28, pp. 2190-2196, 2007.

[173] M. Kõrgesaar and J. Romanoff, "Influence of mesh size, stress triaxiality and damage induced softening on ductile fracture of large-scale shell structures," *Marine Structures,* vol. 38, pp. 1-17, 10// 2014.

[174] T. S. Cao, "Numerical simulation of 3D ductile cracks formation using recent improved Lode-dependent plasticity and damage models combined with remeshing," *International Journal of Solids and Structures,* vol. 51, pp. 2370-2381, 6/15/ 2014.

[175] M. Brünig, S. Gerke, and D. Brenner, "New 2D-Experiments and Numerical Simulations on Stress-state-dependence of Ductile Damage and Failure," *Procedia Materials Science,* vol. 3, pp. 177-182, // 2014.

[176] X. Teng, "Numerical prediction of slant fracture with continuum damage mechanics," *Engineering Fracture Mechanics,* vol. 75, pp. 2020-2041, 2008.

[177] A. Fatemi and N. Shamsaei, "Multiaxial fatigue: An overview and some approximation models for life estimation," *International Journal of Fatigue,* vol. 33, pp. 948-958, 8// 2011.

[178] J. Schijve and J. Schijve, *Fatigue of structures and materials*: Springer, 2001.

[179] D. Gustafsson and E. Lundström, "High temperature fatigue crack growth behaviour of Inconel 718 under hold time and overload conditions," *International Journal of Fatigue,* vol. 48, pp. 178-186, 2013.

[180] D. Gustafsson, J. Moverare, S. Johansson, M. Hörnqvist, K. Simonsson, S. Sjöström*, et al.*, "Fatigue crack growth behaviour of Inconel 718 with high temperature hold times," *Procedia Engineering,* vol. 2, pp. 1095-1104, 2010.

[181] P. Heuler, E. Affeldt, and R. J. H. Wanhill, "Effects of loading waveform and stress field on high temperature fatigue crack growth of alloy 718," *Materialwissenschaft und Werkstofftechnik,* vol. 34, pp. 790-796, 2003.

[182] D. Gustafsson, J. J. Moverare, S. Johansson, K. Simonsson, M. Hörnqvist, T. Månsson*, et al.*, "Influence of high temperature hold times on the fatigue crack propagation in Inconel 718," *International Journal of Fatigue,* vol. 33, pp. 1461-1469, 2011.

[183] R. Liu, Z. J. Zhang, P. Zhang, and Z. F. Zhang, "Extremely-low-cycle fatigue behaviors of Cu and Cu–Al alloys: Damage mechanisms and life prediction," *Acta Materialia,* vol. 83, pp. 341-356, 2015.

[184] L. Kang and H. Ge, "Predicting Ductile Crack Initiation of Steel Bridge Structures Due to Extremely Low-Cycle Fatigue Using Local and Non-Local Models," *Journal of Earthquake Engineering,* vol. 17, pp. 323-349, 2013.

[185] L. Tong, X. Huang, F. Zhou, and Y. Chen, "Experimental and numerical investigations on extremely-low-cycle fatigue fracture behavior of steel welded joints," *Journal of Constructional Steel Research,* vol. 119, pp. 98-112, 2016.

[186] C. Guionnet, "Modeling of ratchetting in biaxial experiments," *Journal of Engineering Materials and Technology,* vol. 114, pp. 56-62, 1992.

[187] N. Ohno and J. D. Wang, "Kinematic hardening rules with critical state of dynamic recovery, Part II: application to experiments of ratchetting behavior," *International journal of plasticity,* vol. 9, pp. 391-403, 1993.

[188] J. L. Chaboche, "Modeling of ratchetting: evaluation of various approaches," *European journal of mechanics. A. Solids,* vol. 13, pp. 501-518, 1994.

[189] G. Z. Voyiadjis and S. M. Sivakumar, "A robust kinematic hardening rule with ratchetting effects: Part I. Theoretical formulation," *Acta Mechanica,* vol. 90, pp. 105-123, 1991.

[190] T. Hassan and S. Kyriakides, "Ratcheting of cyclically hardening and softening materials: II. Multiaxial behavior," *International Journal of Plasticity,* vol. 10, pp. 185-212, 1994.

[191] T. Hassan and S. Kyriakides, "Ratcheting of cyclically hardening and softening materials: I. Uniaxial behavior," *International Journal of Plasticity,* vol. 10, pp. 149-184, 1994.

[192] P. Delobelle, P. Robinet, and L. Bocher, "Experimental study and phenomenological modelization of ratchet under uniaxial and biaxial loading on an austenitic stainless steel," *International Journal of Plasticity,* vol. 11, pp. 295-330, 1995.

[193] N. Ohno, "Current state of the art in constitutive modeling for ratcheting," in *Proceedings of the 14th International Conference on SMiRT*, *Lyon, France*, 1997, pp. 201-212.

[194] Y. Jia and Y. Bai, "Ductile fracture prediction for metal sheets using all-strain-based anisotropic eMMC model," *International Journal of Mechanical Sciences,* vol. 115, pp. 516-531, 2016.

[195] Y. Jia and Y. Bai, "Experimental study on the mechanical properties of AZ31B-H24 magnesium alloy sheets under various loading conditions," *International Journal of Fracture,* vol. 197, pp. 25-48, 2016.

[196] Z. Xia and F. Ellyin, "A constitutive model with capability to simulate complex multiaxial ratcheting behaviour of materials," *International journal of plasticity,* vol. 13, pp. 127-142, 1997.

[197] W. Prager, "A new method of analyzing stresses and strains in work-hardening plastic solids," 1956.

[198] D. C. Drucker and L. Palgen, "On stress-strain relations suitable for cyclic and other loading," *Journal of Applied Mechanics,* vol. 48, pp. 479-485, 1981.

[199] A. Manonukul, F. P. E. Dunne, D. Knowles, and S. Williams, "Multiaxial creep and cyclic plasticity in nickel-base superalloy C263," *International journal of plasticity,* vol. 21, pp. 1-20, 2005.

[200] R. Mücke and O.-E. Bernhardi, "On temperature rate terms for viscoplastic constitutive models with applications to high temperature materials," *Computer methods in applied mechanics and engineering,* vol. 195, pp. 2411-2431, 2006.

[201] M. M. Shenoy, D. L. McDowell, and R. W. Neu, "Transversely isotropic viscoplasticity model for a directionally solidified Ni-base superalloy," *International journal of plasticity,* vol. 22, pp. 2301-2326, 2006.

[202] J. Tong and B. Vermeulen, "The description of cyclic plasticity and viscoplasticity of waspaloy using unified constitutive equations," *International journal of fatigue,* vol. 25, pp. 413-420, 2003.

[203] T.-W. Kim, D.-H. Kang, J.-T. Yeom, and N.-K. Park, "Continuum damage mechanics-based creep–fatigue-interacted life prediction of nickel-based superalloy at high temperature," *Scripta Materialia,* vol. 57, pp. 1149-1152, 2007.

[204] D. Gustafsson, J. J. Moverare, K. Simonsson, and S. Sjöström, "Modeling of the constitutive behavior of inconel 718 at intermediate temperatures," *Journal of engineering for gas turbines and power,* vol. 133, p. 094501, 2011.

[205] N. Ohno, "Constitutive modeling of cyclic plasticity with emphasis on ratchetting," *International Journal of Mechanical Sciences,* vol. 40, pp. 251-261, 2// 1998.

[206] J.-T. Yeom, S. J. Williams, I.-S. Kim, and N.-K. Park, "Unified viscoplastic models for low cycle fatique behavior of Waspaloy," *Metals and Materials International,* vol. 7, pp. 233-240, 2001.

[207] J. Komotori and M. Shimizu, "Fracture mechanism of ferritic ductile cast iron in extremely low cycle fatigue," *Low cycle fatigue and elasto–plastic behaviour of materials. Elsevier Science Ltd,* pp. 39-44, 1998.

[208] K. Shimada, J. Komotori, and M. Shimizu, "Fracture mode transition and damage in extremely low cycle fatigue," in *Low Cycle Fatigue and Elasto-Plastic Behaviour of Materials*, ed: Springer, 1987, pp. 680-686.

[209] L. F. Coffin Jr, "A study of the effect of cyclic thermal stresses on a ductile metal," *American Society of Mechanical Engineers,* vol. 76, pp. 931-950, 1954.

[210] S. S. Manson, *Behavior of materials under conditions of thermal stress*: NACA TN 2933, 1953.

[211] J. Komotori and M. Shimizu, "Microstructural Effect Controlling Exhaustion of Ductility in Extremely Low Cycle Fatigue," in *Low Cycle Fatigue and Elasto-Plastic Behaviour of Materials—3*, ed: Springer, 1992, pp. 136-141.

[212] A. M. Kanvinde and G. G. Deierlein, "Cyclic void growth model to assess ductile fracture initiation in structural steels due to ultra low cycle fatigue," *Journal of engineering mechanics,* vol. 133, pp. 701-712, 2007.

[213] R. W. Fuller, N. Shamsaei, and J. Simsiriwong, "Fatigue Life Predictions for Irradiated Stainless Steels Considering Void Swellings Effects," *Engineering Failure Analysis,* 2015.

[214] D. Fournier and A. Pineau, "Low cycle fatigue behavior of inconel 718 at 298 K and 823 K," *Metallurgical Transactions A,* vol. 8, pp. 1095-1105, 1977.

[215] F. Alexandre, S. Deyber, and A. Pineau, "Modelling the optimum grain size on the low cycle fatigue life of a Ni based superalloy in the presence of two possible crack initiation sites," *Scripta Materialia,* vol. 50, pp. 25-30, 2004.

[216] D. F. Socie, "Multiaxial fatigue damage models," *Journal of Engineering Materials and Technology,* vol. 109, pp. 293-298, 1987.

[217] M. Clavel and A. Pineau, "Fatigue behaviour of two nickel-base alloys I: Experimental results on low cycle fatigue, fatigue crack propagation and substructures," *Materials Science and Engineering,* vol. 55, pp. 157-171, 1982.

[218] Y. Bao and R. Treitler, "Ductile crack formation on notched Al2024-T351 bars under compression–tension loading," *Materials Science and Engineering: A,* vol. 384, pp. 385-394, 2004.

[219] Y. Bai, "Fracture of 1045 steel under complex loading history," in *The 8th International Conference and Workshop on numerical simulation of 3D seet metal forming processes (NUMISHEET 2011)*, 2011, pp. 758-764.

[220] H. Wen and H. Mahmoud, "New Model for Ductile Fracture of Metal Alloys. II: Reverse Loading," *Journal of Engineering Mechanics,* vol. 142, p. 04015089, 2015.

[221] P. C. Paris and F. Erdogan, "A critical analysis of crack propagation laws," *Journal of basic engineering,* vol. 85, pp. 528-533, 1963.

[222] T. Endo, "Damage evaluation of metals for random on varying loading-three aspects of rain flow method," p. 374.

[223] Y. Bao and T. Wierzbicki, "On fracture locus in the equivalent strain and stress triaxiality space," *International Journal of Mechanical Sciences,* vol. 46, pp. 81-98, 1// 2004.

[224] H. Wen and H. Mahmoud, "New Model for Ductile Fracture of Metal Alloys. I: Monotonic Loading," *Journal of Engineering Mechanics,* vol. 142, p. 04015088, 2015.

[225] M. Algarni, Y. Bai, and Y. Choi, "A study of Inconel 718 dependency on stress triaxiality and Lode angle in plastic deformation and ductile fracture," *Engineering Fracture Mechanics,* vol. 147, pp. 140-157, 2015.

[226] M. S. Algarni, Y. Jia, J. Karl, A. P. Gordon, Y. Bai, M. The Minerals*, et al.*, "Linkage between Ductile Fracture and Extremely Low Cycle Fatigue of Inconel 718 Under Multiaxial Loading Conditions," in *TMS2015 Supplemental Proceedings*, ed: John Wiley & Sons, Inc., 2015, pp. 1023-1030.

[227] A. Version, "6.11. User's manual," *Dassault Systemes,* 2011.